ATOMIC-RESOLUTION TWO-DIMENSIONAL MAPPING OF LOCAL BONDING CHANGES AT TRANSITION METAL OXIDE INTERFACES

A Dissertation

Presented to the Faculty of the Graduate School

of Cornell University

in Partial Fulfillment of the Requirements for the Degree of

Doctor of Philosophy

by

Julia Agnes Mundy

May 2014

ATOMIC-RESOLUTION TWO-DIMENSIONAL MAPPING OF LOCAL BONDING CHANGES AT TRANSITION METAL OXIDE INTERFACES

Julia Agnes Mundy, Ph.D.

Cornell University 2014

Transition metal oxides exhibit almost every physical state known however electronic changes at polar interfaces between transition metal oxides offer the tantalizing possibility to stabilize further novel ground states. These interface stabalized phases can also cause unintended reconstructions in thin films poised for inclusion in next-generation devices. Here we use scanning transmission electron microscopy (STEM) in conjunction with electron energy loss spectroscopy (EELS) to directly probe with atomic-resolution the charge distribution across transition metal oxide interfaces. We are particularly interested in quantifying the intrinsic electronic reconstructions while maintaining sensitivity to defects at the interface that could obscure the underlying electronic properties.

We first investigate $LuFe_2O_4$, purported to be the highest known ferroelectric ferrimagnet. We demonstrate that the local bonding of the oxygen atoms, incorporated into two distinct sites in the crystal, can be determined and mapped with atomic-resolution. We find no evidence for iron charge-ordering claimed to give rise to the ferroelectricity.

We then investigate two similar interfaces between polar and non-polar perovskite oxides, systems that are typically considered with the polar catastrophe model framework. In the case of $LaAlO_3/SrTiO_3$, we show an exquisite dependence of interface conductivity on the $LaAlO_3$ film composition. Using EELS,

we demonstrate that in the case of La-rich films, cation vacancies accumulate at the interface to screen the polarization catastrophe without valence changes. In contrast, the $La_{1-x}Sr_xMnO_3/SrTiO_3$ system investigated does not show these defect-mediated interfacial screening mechanisms. Rather, we demonstrate a quantitative agreement between interfacial charge transfer present on the manganese sites of the crystal and the polar catastrophe model for $x < 0.3$, the insulating regime of the phase diagram.

Finally, we investigate a related system to the $La_{1-x}Sr_xMnO_3$ films: ordered superlattices of $(LaMnO_3)_{2n}(SrMnO_3)_n$. Here we show a delocalization of the excess charge on the manganese sites for $n \geq 2$ as mapped by EELS spectroscopic imaging. Combined these four systems allow us a unique opportunity to measure electronic properties at oxide interfaces in real space with atomic-resolution.

BIOGRAPHICAL SKETCH

Julia Mundy was born in Syracuse, New York. She graduated from Manlius Pebble Hill School in 2002. She received a bachelor's degree in Chemistry and Physics and a master of arts degree in Chemistry from Harvard University in 2006. She then taught high school science for two years with Teach for America before entering the PhD program in Applied Physics at Cornell University in 2008. At Cornell, her work has focused on the study of complex oxide heterostructures under the guidance of Darrell Schlom and David Muller.

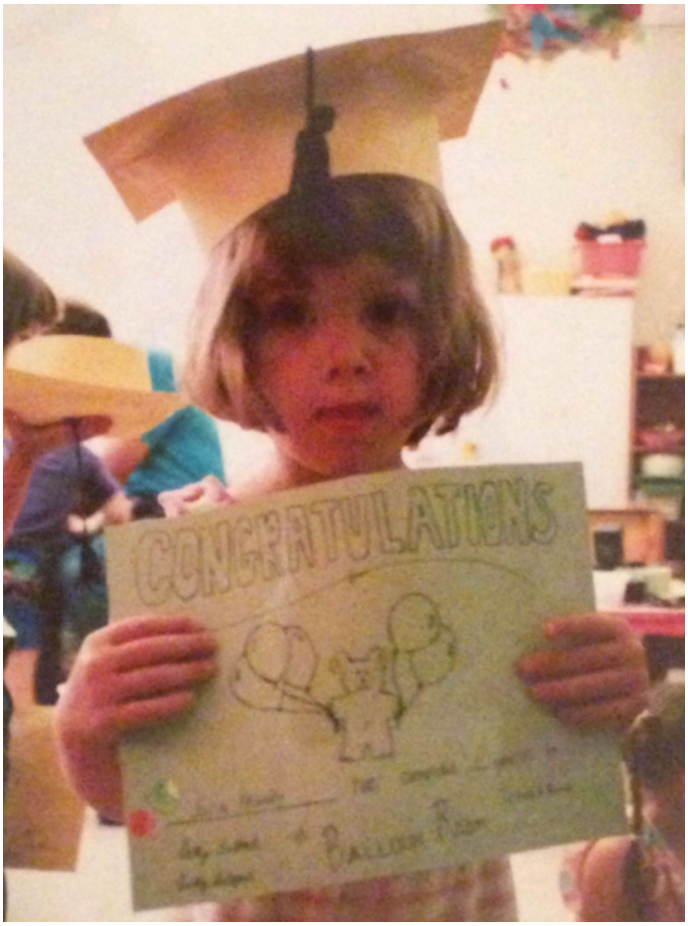

This thesis is dedicated to Ruth L. Satter, physicist, microscopist and loving grandmother.

ACKNOWLEDGEMENTS

I would like to thank my advisors Darrell G. Schlom and David A. Muller for their guidance and support over the past five and a half years. I have greatly benefitted from their insight in the field of complex oxides, the intellectual freedom they have afforded me to explore a range of projects and incredibly high standards for my research. I would also like to thank Professor Joel D. Brock for serving on my special committee and carefully reading this thesis as well as his mentorship as my Director of Graduate Studies.

I would like to thank John Grazul and Mick Thomas for their tireless maintenance of the microscopy facilities, assistance operating the tools and their consistent support over my graduate studies. I would also like to thank Dr. Earl Kirkland for many conversations on microscopy as well as his contributions to the Nion Microscope; the large spectroscopic images shown in Chapter 6 in particular are a result of his alignment condition of the instrument. I also greatly appreciate many fruitful conversations about complex oxide thin films with Professor Craig Fennie and Professor Kyle Shen.

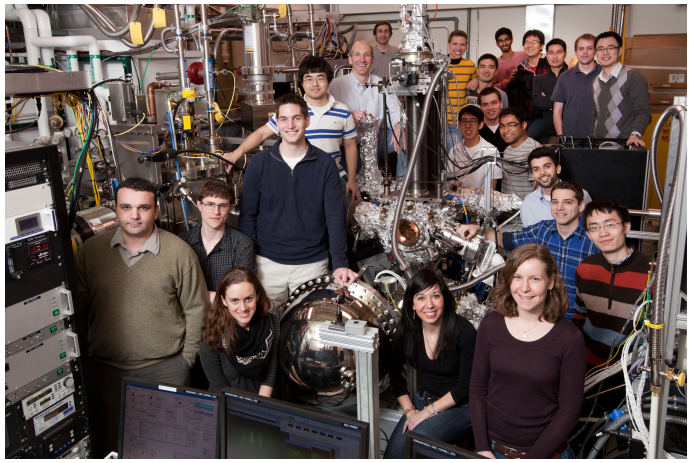

I have had the great pleasure of many wonderful colleagues in the Muller group and the Schlom group. I would like thank the leadership of older grad-

uate students Judy Cha, Peter Ercius, Jerome Hyun and Lena Kourkoutis and post-docs Ye Zhu and HuiQiong Wang in the Muller group. I benefitted greatly from collaborations and friendship with Huolin Xin and Robby Hovden. I would also like to thank the newer generation of Muller group students Paul Cueva, Megan Holtz, Pinshane Huang, Barnaby Levin, Qingyun Mao, Kayla Nguyen and Yingchao Yu. I have also greatly enjoyed the collaborations and friendships of all of the students and post-docs in the Schlom group: Carolina Adamo, Charles Brooks, Jessica Burton, Natalie Dawley, Phil King, Rainer Held, John Heron, Che-Hui Lee, Alex Melville, Hari Nair, Yuefeng Nie, Hanjong Paik, Arsen Soukiassian, Zhe Wang, Maitri Warusawithana, Josh Williams and Shaobo Zhu. It was a pleasure to image so many pristine samples as well as collaborate on growth projects. I would also like to thank the members of the Shen group for collaborations and camaraderie especially Eric Monkman and Danny Shai. Finally, I have had the pleasure of collaborating with three undergraduate students: Randi Cabezas, Steve Dacek and Daniel Hodash.

In addition to the MBE-grown samples from the Schlom group, I have had the pleasure of imaging samples from Harold Hwang's group at the Univer-

sity of Toyko and Stanford University from Yasuyuki Hikita, Takeaki Hidaka, Takeaki Yajima, Takuya Higuchi, Hiroki Sato, Dae Young Kwon and Boggi Kim. I also enjoyed my collaborations with Andreas Schmehl, Thomas Mairoser and Rainer Jany in Professor Jochen Mannhart's group. I appreciate strong collaborations with Rajiv Misra and Jarrett Moyer in Peter Schiffer's group as well as Hena Das in Craig Fennie's group studying $LuFeO_3$ thin films. Finally, I appreciated the work with Dr. Vic Lui and his team at General Motors on the Pt-Co project.

Finally, I would like to thank my family and friends for their constant support, encouragement and love. I am very lucky to have benefited from amazing educational experiences, wonderful teachers and great friends from my start at Jowonio and Manlius Pebble Hill through my time at Harvard and Cornell. I appreciate my parents' and grandparents' dedication to education and work to making those opportunities possible; it was incredible to be in the position of "simply" trying to follow in the math/science footsteps of my grandmother and great-aunt.

TABLE OF CONTENTS

LIST OF FIGURES

CHAPTER 1

INTRODUCTION

1.1 Overview

Transition metal perovskite oxides exhibit almost every physical state known: metallic conductivity[**?**], (high-temperature) superconductivity[**?**, **?**, **?**, **?**, **?**], ferroelectricity[**?**, **?**], ferromagnetism[**?**] and sometimes have multiferroic orders[**?**, **?**, **?**, **?**]. Moreover, the workhorse oxide substrate, $SrTiO_3$, can be epitaxially integrated onto silicon[**?**, **?**, **?**], making these materials with colossal magnetoresistance or superconductivity potentially exciting for next-generate technological devices.[**?**] These properties, as well as the theoretical interest in these materials, largely stem from the fact that the electrons in the system are strongly-correlated[**?**]: their properties cannot be described by single electron models, as can be done with simple metals, nor by pure ionic models. Most of the transition metal perovskite oxides have partially filled d or f orbitals where the electrons interact strongly with their neighboring electrons beyond the interactions that would be expected for a single-particle like "electron sea" interaction. For example, the d electrons of the transition-metals experience competing forces between strong Coulombic interactions which tend to localize the electrons to single lattice sites while simultaneous hybridization with the oxygen orbitals tends to delocalize the electrons. These correlations can generate the rich array of magnetic and electronic properties described above.

The crystal structure of the perovskite oxides is shown in Fig. **??**. The ABO_3 structure consists of octahedra of oxygen atoms surrounding the B-site cation; the A-site cation sits on the corner of the cubic crystal structure. Most elements

can be incorporated into the perovskite crystal structure given an appropriate companion cation as shown in Fig. **??**.[**?**] The size-ratios of the incorporated cations can cause deviations to the cubic perovskite crystal structure.[**?**] For example, if the *B*-site cation is "too-small", it will experience an off-centering from the center of the oxygen octahedral.[**?**] As is the case in $BaTiO_3$, this will lead to a net polarization and ferroelectricity. In contrast if the *A*-site cation is "too-small" the system will respond with tilts of the oxygen octahedral as is the case for $CaTiO_3$.

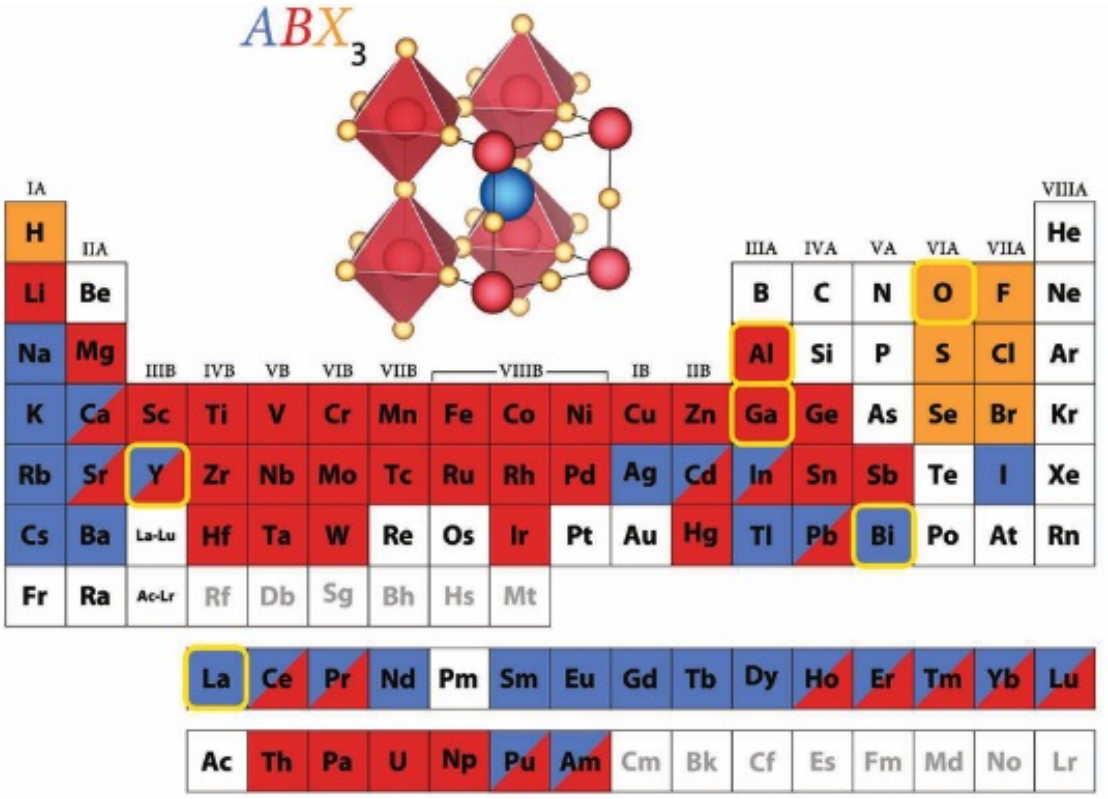

Figure 1.1: A cartoon of the perovskite crystal structure with the formula ABX_3 (in this thesis, only ABO_3 structures will be considered). Most elements can be incorporated in this crystal structure as shown on the color-coded periodic table. For example, all elements found in the *A*-site are colored blue. Reproduced from [**?**]

In addition to ternary ABO_3 compounds, the *A*- or *B*-sites can also contain a

mixture of multiple elements. For example, the $La_{1-x}Sr_xMnO_3$ system that is the subject of Chapter 6 has a mixture of strontium and lanthanum on the *A*-site of the crystal. As shown in the phase digram[**?**] in Fig. **??**, the end member $LaMnO_3$ is a paramagnetic insulator at room-temperature. At the other end of the spectrum, $SrMnO_3$ is also insulating and non-magnetic at room-temperature. Hole doping the La^{+3} with Sr^{+2} generates a room-temperature ferromagnetic metallic state over a range of cation ratios. In this manner, the cation stoichiometry can be tuned to systematically vary the ground state to exhibit a wide range of electronic and magnetic properties.

1.2 Perovskite oxide interfaces and heterostructures

Not only do hundreds of compounds form with the canonical perovskite structure, yet multiple different perovskite compounds can be combined in a heterostructure due to the close lattice matching of the parent compounds. Figure **??** plots the lattice constants of materials often used a substrates for the growth of thin film oxides as well as multifunctional thin films.[**?**] As shown, most compounds have a psuedocubic lattice parameter ranging from 3.7 Å to 4.1 Å or about 10% lattice mismatch across the entire series of compounds plotted. This permits the epitaxial growth of thin films, below a critical thickness, on substrate templates, maintaining a coherent cation and oxygen backbone across the interface as shown in Fig. **??**.

Not only does the close lattice matching of the perovskite oxides permit the epitaxial integration of various oxide compounds with functional properties, additionally the strain induced can change the properties of the thin film. For

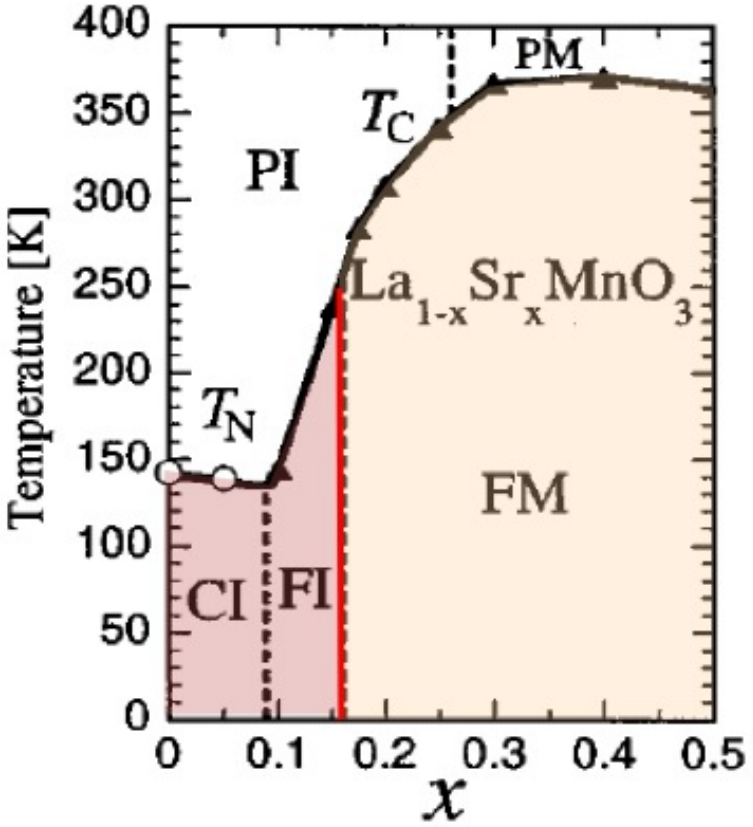

Figure 1.2: Phase diagram of $La_{1-x}Sr_xMnO_3$. Various electronic and magnetic states are accessible as a function of cation ratio and temperature as shown: PI (Paramagnetic Insulating), PM (Paramagnetic Metallic), CI (Spin-canted Insulating), FI (Ferromagnetic Insulating) and FM (Ferromagnetic Metallic). Reproduced from [**?**]

example, in the bulk form, $EuTiO_3$ is antiferromagnetic and paraelectric. The application of either tensile (~0.75%) or compressive (~1.2%) strain through growth on an appropriate epitaxial substrate was theoretically predicted and experimentally[**?**] shown to drive the material into the ferromagnetic ferroelectric state. While attempts to provide ~1% of compression through hydrostatic pressure would crack the crystal, the epitaxial template provided by the substrate can impart significant amounts of strain to thin films and access novel states of the material not present in the bulk crystals.

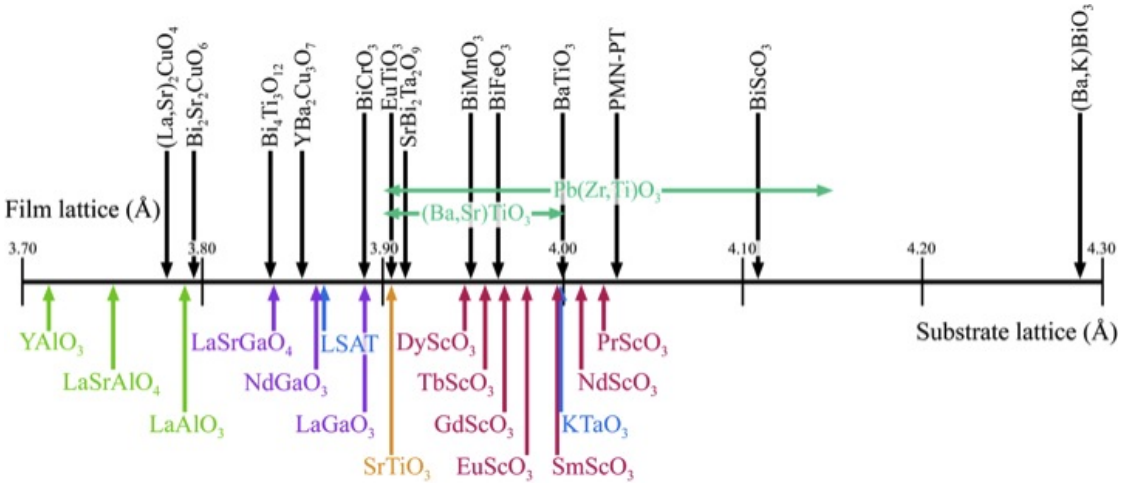

Figure 1.3: Numberline of the lattice parameter of various perovskite oxides. The materials accessible as single crystal, commercial substrates are plotted on the bottom. A sampling of functional oxides are plotted as well for reference. Reproduced from [**?**]

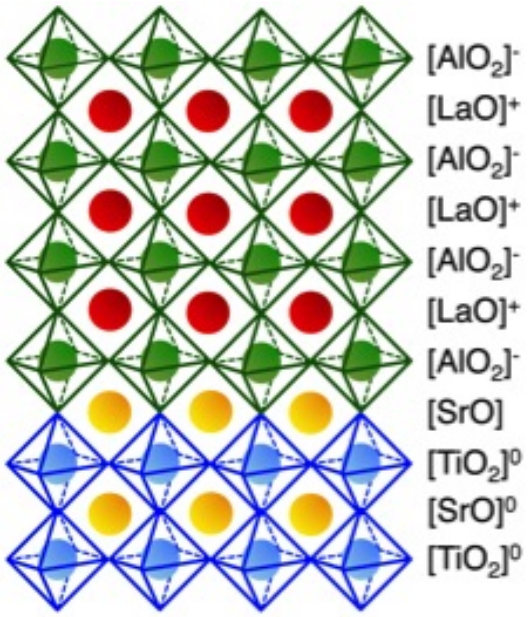

Figure 1.4: A cartoon of a thin film of $LaAlO_3$ on a [100] $SrTiO_3$ substrate. Sr, Ti, La and Al are plotted in yellow, blue, red and green respectively. For clarity, octahedral rotations are not pictured.

Interleaving multiple transition metal oxides into a heterostructure can also create a material with properties not present in either bulk compound. For example, $SrTiO_3$ is paraelectric and $PbTiO_3$ is ferroelectric. Superlattices generated by precise layering of the two compounds were found to exhibit improper ferroelectricity with a large temperature-independent dielectric constant.[**?**] Further theoretical work has predicted that some "double perovskites" or ordered superlattices of $[ABO_3]$ and $[A'BO_3]$ with orthorhombic crystal structures could produce a ferroelectric ground state not present in the bulk of either compound.[**?**, **?**, **?**, **?**] Here the improper ferroelectricity is induced by the octahedral tilting of the oxygen backbone. In this manner, materials with novel properties can be engineering through the epitaxial integration and appropriate layering of multiple perovskite oxide materials.

In addition to driving a phase transition through the application of strain and the engineering of new materials through a superlattice architecture, underlying electronic reconstructions at an interface between two materials can dominate the properties observed. One of the most widely studied examples of this phenomenon is the $SrTiO_3/LaAlO_3$ interface. Both materials are insulators in the bulk yet the interface between the two forms a confined, two-dimensional electron liquid and is superconducting at low temperatures.[**?**, **?**] Moreover, novel magnetic properties have been observed despite the fact that both compounds are non-magnetic in the bulk.[**?**] Chapter 2 will discuss the physics of this interface and Chapter 4 the interplay between extrinsic defects and intrinsic electronic reconstructions which emerge for this system.

1.3 Synthesis of Oxide Heterostructures

Experimentally, realization of these engineered perovskite oxide thin films and superlattices requires deposition techniques capable of controlling the structure with atomic-level precision. The films presented in this thesis were grown by two techniques: reactive oxide molecular beam epitaxy (MBE) and pulsed laser deposition (PLD). The Vecco Gen10 MBE system at Cornell University has nine ports, each containing a single elemental source. Each of these sources is heated in an effusion cell to produce a molecular beam of atoms which is sprayed onto the substrate target. The flux of atoms can be calibrated roughly through use of a quartz crystal microbalance and more precisely during growth using reflection high-energy electron diffraction (RHEED).[**?**] By opening and closing the shutters for the sources at precise intervals, a single monolayer dosage of a particular element can in principle be delivered to the substrate. The growth occurs in a background of oxygen, in the form of molecular oxygen (O_2) or distilled ozone (O_3). The thin films of $LuFe_2O_4$, $LaMnO_3/SrMnO_3$ heterostructures and $LaAlO_3/SrTiO_3$ interfaces presented in this thesis were grown by MBE.

In contrast, pulsed laser deposition starts with a target (or multiple targets) of solid compounds with the intended composition. A high-energy pulsed laser is focused onto the target, causing the material to be ablated and form a plasma plume. The material then condenses on the substrate to form the thin film. The deposition can be controlled by adjusting the laser fluence and energy, substrate temperature and background pressure of oxygen in the chamber. Once again, RHEED can be used to monitor the growth $in-situ$. The thin films of $La_{1-x}Sr_xMnO_3$ on the $SrTiO_3$ substrates and superlattices of $LaTiO_3/SrTiO_3$ presented in this thesis were grown by PLD. The precision afforded by both tech-

niques allows high-quality, epitaxial thin films of the desired composition to be patterned, including artificial materials which are not stable in the bulk form.

1.4 Thesis Overview

As shown in this chapter, the perovskite oxide class of materials exhibits a wide range of physical ground states primed for applications in next-generation devices; interfaces and heterostructures between two oxide materials provides a further knob to vary the physical properties exhibited. The goal of this thesis is to provide a site-specific, atomic-resolution understanding of the electronic properties at these complex oxide interfaces.

The intrinsic reconstructions at the interface between an insulating polar film and a non-polar substrate is typically thought of in terms of the polar catastrophe model: the presence of alternating positively and negatively charged layers on a non-polar surface causes the build-up of a non-zero electric field and an electric potential which diverges with sample thickness. The polar catastrophe can be alleviated by transferring charge to the interface, manifest as either the presence of an extra half of an electron or hole per unit cell. Chapter 2 presents the polar catastrophe model and explicitly calculates the effect of cation off-stoichiometry and intermixing on the resulting potential profile. The theory of EELS and application towards probing valence states in oxide thin films is also presented.

Chapter 3 presents a study of natural superlattices of hexagonal $LuFe_2O_4$, purported to be the highest know simultaneous ferroelectric ferrimagnet. EELS is used to probe the local bonding environment of the oxygen atoms. A two-

dimensional analysis of the fine structure of the O-K edge yielded distinct signals for the two inequivalent oxygen sites in the crystal. Comparison to an $ab-initio$ simulation shows that these two components can be interpreted in terms of the differing hybridization of the O p orbitals to the nearest-neighbor Lu and Fe d orbitals, thus producing an atomic-resolution map of the local oxygen bonding environment. This establishes the ability of EELS to probe local deviations in the bonding with single monolayer precision.

The charge transfer in response to the polar catastrophe is then measured for two similar systems. Chapter 4 considers the $LaAlO_3/SrTiO_3$ interface; despite the fact that $LaAlO_3$ and $SrTiO_3$ are both insulators, the interface between the two can be both conducting and superconducting at low temperatures, generating considerable interest in the system. We show that the interfacial conductivity depends exquisitely on the $LaAlO_3$ film stoichiometry. For La-rich films, Al/Ti vacancies cluster at the interface, offsetting the polar catastrophe in the absence of a valence change which would render the system conducting. This work provides the first direct evidence of this new mechanism, cation vacancies, to alleviate the polar catastrophe.

We also consider a similar system, $La_{1-x}Sr_xMnO_3/SrTiO_3$ interfaces, in Chapter 5. Here, by measuring the concentration and valence of the cations, we find an intrinsic electronic reconstruction on the interfacial manganese sites in the insulating films ($x \leq 0.2$). The total charge observed for these insulating manganite films quantitatively agrees with that needed to cancel the polar catastrophe. As the manganite becomes metallic with increased hole-doping, the total charge build-up and its spatial range drop substantially. The spatial range of the charge transfer at the metallic $La_{0.7}Sr_{0.3}MnO_3/SrTiO_3/SrTiO_3$ interface agrees with pre-

vious reports of the screening length in $La_{0.7}Sr_{0.3}MnO_3$, providing an image of the onset of metallic screening in this system in addition to the direct quantification of the charge transferred over a series of samples.

Finally, in Chapter 6, we consider an analog system to $La_{0.67}Sr_{0.33}MnO_3/SrTiO_3$, digital superlattices of $(LaMnO_3)_{2n}(SrMnO_3)_n$. The magnetic and electronic properties of this system are highly dependent on the superlattice layering, n, with metallic ferromagnetic samples observed for $n \leq 2$. We demonstrate that the $n = 1$ superlattice shows a constant occupancy of the manganese d orbitals throughout the superlattice (despite the atomic-resolution sensitivity of EELS shown in Chapter 3). For layering of $n \geq 2$, the manganese d occupancy spatial varies, with additional charge residing in the $LaMnO_3$. This spectroscopic probe of the system can be used to interpret the bulk electronic and magnetic properties of the superlattices.

CHAPTER 2

ELECTRONIC CHANGES AT OXIDE INTERFACES

While perovskite oxides can access almost every physical ground state known, the interface between two perovskite oxides can further display ground states not apparent in the bulk constituents. For example, the superlattices of two insulating materials, $LaTiO_3$ and $SrTiO_3$, display metallic conductivity when patterned with judicious layerings [**?**]. $SrTiO_3$ is a band insulator: the Ti^{+4} sites have an [Ne]$3s^2 3p^6 4s^0 3d^0$ configuration and notably the outer *d* orbitals are empty. In contrast the Ti^{+3} ions in $LaTiO_3$ have a single t_{2g}-*d* electron with the [Ne]$3s^2 3p^6 4s^0 3d^1$ configuration. However, a Mott-Hubbard gap breaks the degeneracy of the three t_{2g}-*d* orbitals due to the strong electron-electron correlations rendering $LaTiO_3$ insulating.

Thus, superlattices of $LaTiO_3$ and $SrTiO_3$ incorporate a spatially varying titanium valence, begging the determination of the valence present at the interfaces: $LaO/TiO_2/SrO$ or $SrO/TiO_2/LaO$. EELS spectroscopy can map the valence of the titanium through the superlattice as shown in Fig. **??**. As shown in Fig. **??** and previously in 1-D in [**?**], the extra t_{2g} electron spatially extends past the chemical signal from the lanthanum in the $LaTiO_3$ layers. This mixed valence $Ti^{+3.5}$ state present at between the $LaTiO_3$ and $SrTiO_3$ layers leads to a spatially confined conducting layer. Thus, the interface stabilizes an electronic state of the titanium not present in either bulk compound, leading to markedly different properties.

This chapter will first present the theory of electronic reconstructions at oxide interfaces following the polar catastrophe model. Explicit consideration will be given to extrinsic defects which can arise in real samples and the interplay

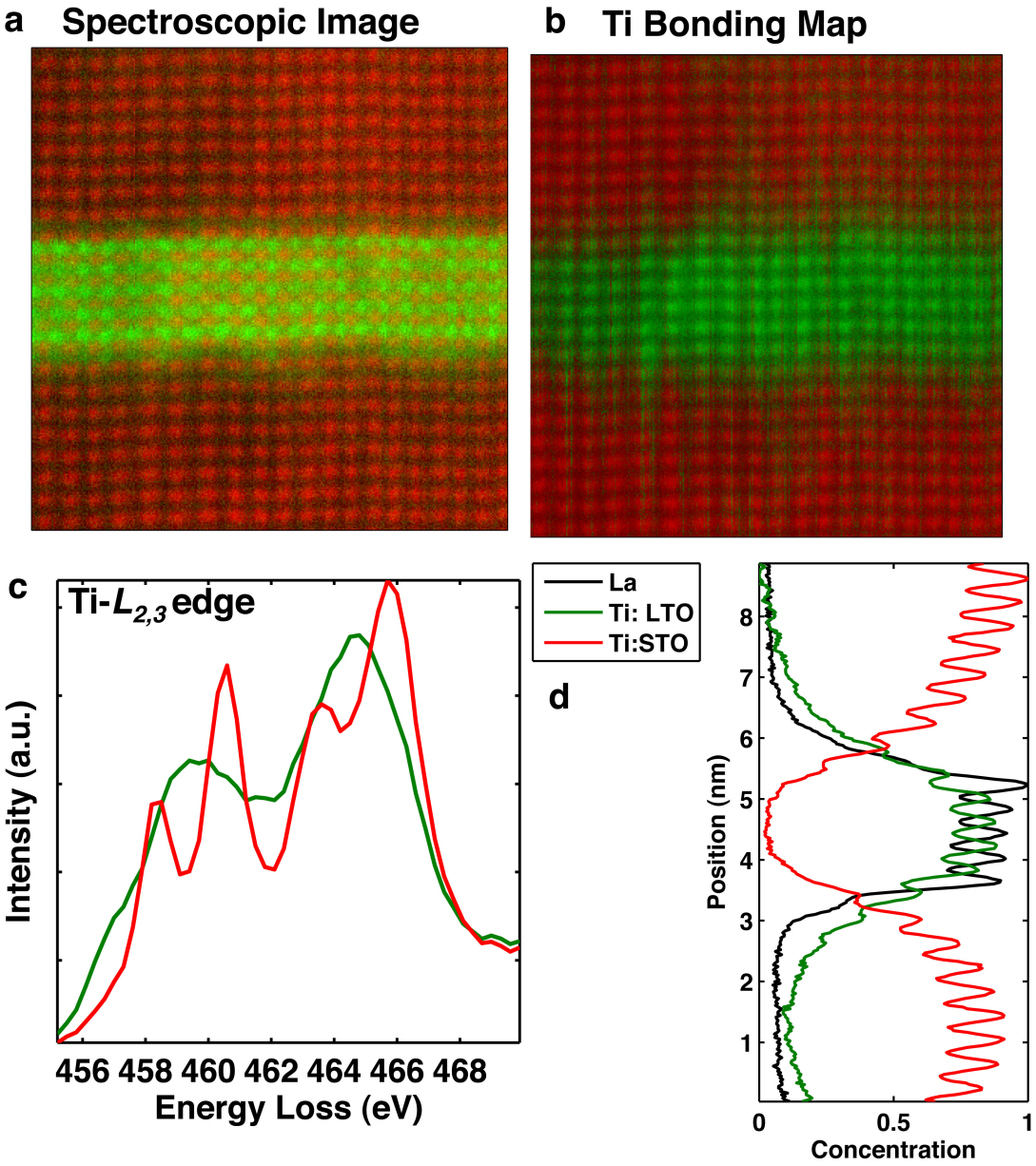

Figure 2.1: Spectroscopic imaging of the titanium valence in a $[LaTiO_3]_5[SrTiO_3]_{10}$ superlattice. (a) A spectroscopic imaging of the cation concentrations with La and Ti in green and red respectively. The La signal is well confined to 5 monolayers with little intermixing. (b) A map of Ti valence with Ti^{+3} and Ti^{+4}, obtained from the signals in (c), are shown in green and red respectively. A binned image in (d) demonstrates that the Ti^{+3} extends spatially further than the chemical fingerprint of the La atoms.

between these defects and the underlying electronic reconstructions. We will then discuss the theory of electron energy loss spectroscopy, which formed the basis for the analysis of the oxide interface in Fig. **??** and will be the primary tool used throughout the thesis to investigate these phases.

2.1 Polar Catastrophe

The $LaTiO_3/SrTiO_3$ superlattice demonstrates the stability of interfacial phases not present in the bulk constituents. In addition to these states, electronic reconstructions can further drive interfacial states not observed as a simple "mixing" of the two bulk compounds. This is demonstrated perhaps most directly by the observation of conductivity[**?**] and later superconductivity[**?**] and novel magnetic phases[**?**] at the interface between insulators $LaAlO_3$ and $SrTiO_3$. $LaAlO_3$ is a band insulator; viewed in the [100] direction, $LaAlO_3$ is composed of alternating planes of polar $[LaO]^{+1}$ and $[AlO_2]^{-1}$ as shown in Fig. **??**a. In contrast, the band insulator $SrTiO_3$ has alternating non-polar layers of $[SrO]^0$ and $[TiO_2]^0$. This sharp onset of charge modulation in the film leads to an alternating, positive electric field and diverging potential as a function of film thickness as shown in Fig. **??**a. This "polar catastrophe" was first described in semiconductor interfaces[**?**] and can be rectified in a number of ways. One is to transfer 0.5 e^- to the interfacial titanium sites, as shown in Fig. **??**b. This results in an electric field which oscillates around 0 and a finite potential which does not diverge with layer thickness.[**?**] The transfer of this extra electronic charge to the interface results in a superconducting electron liquid, spatially confined to this interface region.

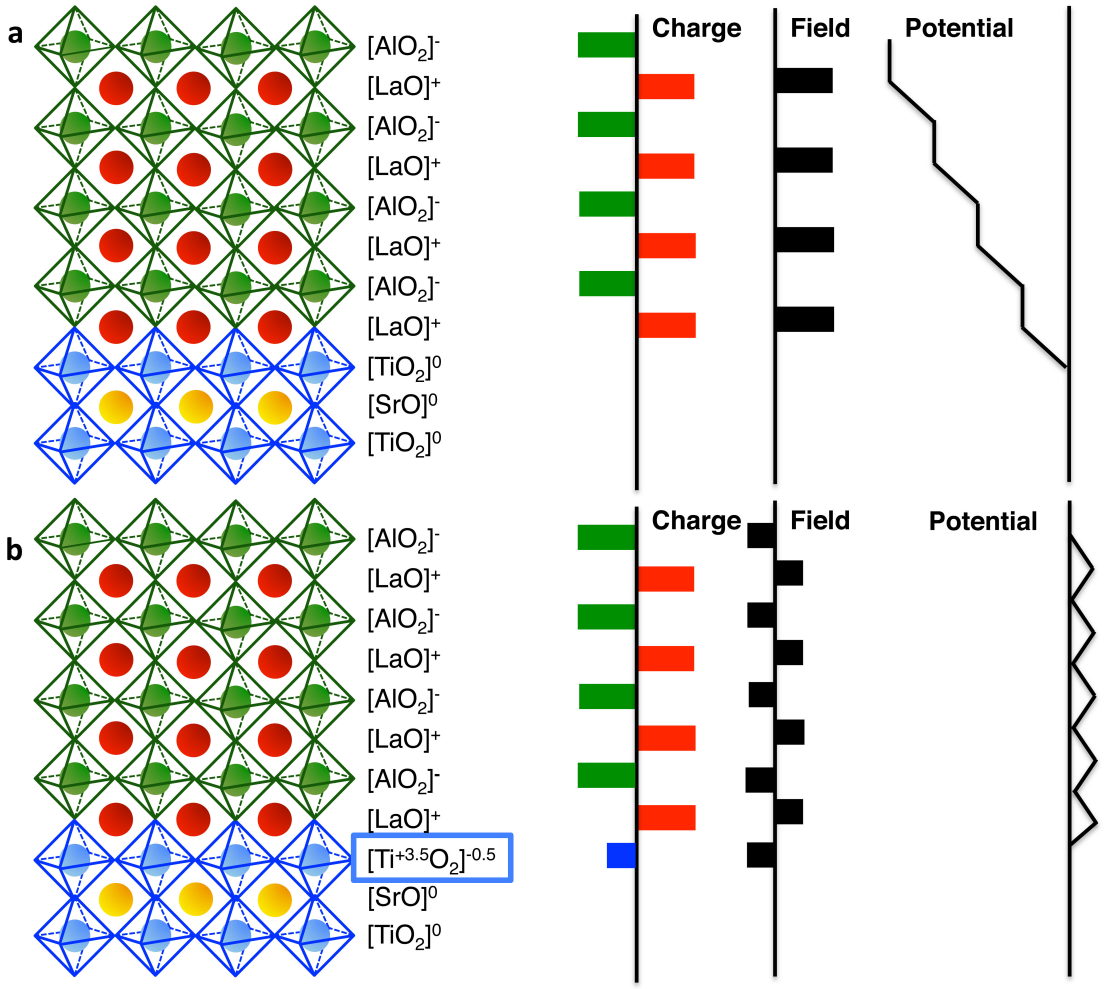

Figure 2.2: The polar catastrophe for the *n*-type $LaAlO_3/SrTiO_3$ interface. (a) shows a model of the interfacial layering, charge, electric field and diverging potential. In (b), the diverging potential is alleviated by transferring an extra half an electron to the top Ti-O layer.

The interface shown in Fig. **??** is the "*n*-type" interface where the $SrTiO_3$ is terminated with a $[TiO_2]$ layer and the $LaAlO_3$ begins with a monolayer of $[LaO]^{+1}$. In contrast, an alternative growth sequence could be envisioned where the $SrTiO_3$ could be terminated with a [SrO] layer and the $LaAlO_3$ film starting with a monolayer of $[AlO_2]^{-1}$. In this case, +0.5 $e-$/unit cell layer charge is required to screen the polarization catastrophe at the interface. Given that the Ti^{+4} ions in $SrTiO_3$ have an electron configuration of $[Ne]3s^2 3p^6 4s^0 3d^0$, they

will not lose additional electronic charge to drop below the Ti^{+4} oxidation state. In contrast, oxygen vacancies can provide the interfacial charge in the absence of valence changes leading to the *p*-type interface as shown in Fig. **??**. The two different compensation mechanisms–titanium valence changes and oxygen vacancies–for the different layering patterns lead to different electronic properties of the interface as well as different growth modes of the $LaAlO_3/SrTiO_3$ superlattices.[**?**, **?**]

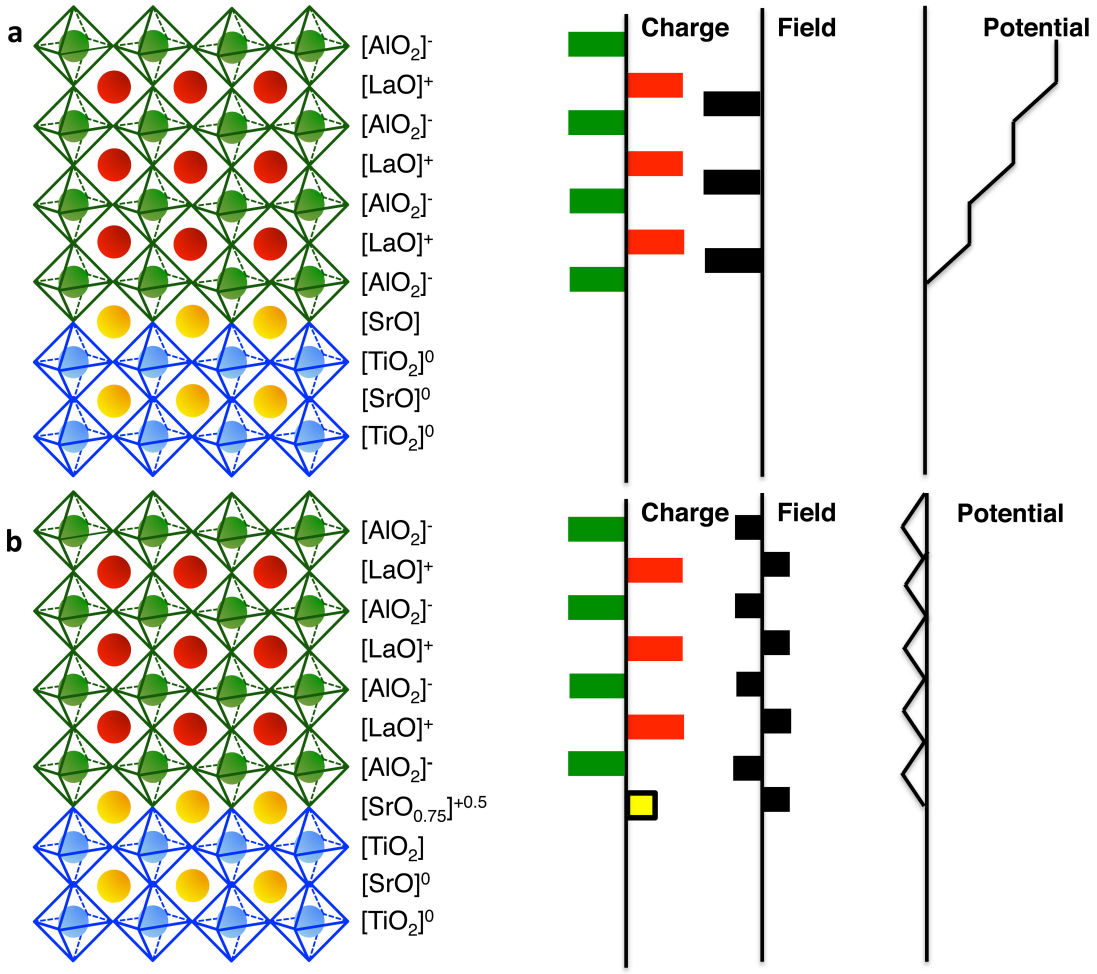

Figure 2.3: The polar catastrophe for the *p*-type $LaAlO_3/SrTiO_3$ interface. (a) shows a model of the interfacial layering, charge, electric field and diverging potential. In (b), the diverging potential is alleviated by oxygen vacancies at the top SrO layer.

It is important to note that the carrier concentrations found at the "*n*-type" $LaAlO_3/SrTiO_3$ interfaces has varied.[**?**] A simple estimate from 0.5 e^-/unit cell of charge transferred to the interface would yield carrier concentrations around 3.5 x 10^{14} cm^{-2}. The original reports of conductivity at the interface found sheet densities closer to 4 x 10^{16} cm^{-2},[**?**] two orders of magnitude higher than what would be expected from the polar catastrophe model. Follow-up experiments varied the oxygen pressure during the growth and post-growth during an annealing step were able to vary the carrier concentration from 10^{16} cm^{-2} to 10^{13} cm^{-2}.[**?**] Further experiments have consistently identified sheet densities closer to 10^{13} cm^{-2},[**?**, **?**] now an order of magnitude below that expected from the polar catastrophe model. This could indicate that the $LaAlO_3$ film cannot be treated in the fully ionic limit and rather the layer charges are much lower than ± 1 due to partial covalency. The initial films with sheet densities of 10^{16} cm^{-2} could indicate that those films had oxygen vacancies in the substrate (due to low pressure growths) in addition to the intrinsic carriers caused by a response to the polar catastrophe.

The simultaneous presence of oxygen vacancies and titanium bonding changes at the $LaAlO_3/SrTiO_3$ interface captures the fact that there are a number of both intrinsic and extrinsic factors that can emerge at real interfaces including:

- Many synthetic interfaces show chemical interdiffusion and intermixing rather than the atomically abrupt interfaces shown in the cartoon in Fig. **??**.
- Deposited thin films could potentially contain cation and/or oxygen vacancies altering the charges of the layers.

- Lattice distortions can impact the charge profile in ionic thin films/substrates.

While there are a variety of other defects and types of disorder that can dramatically affect interface properties, we consider each of the above explicitly.

2.1.1 Polar Catastrophe in the presence of interdiffusion

Chemical interdiffusion is present in many thin films to some degree. For the $LaAlO_3/SrTiO_3$ superlattices, we might observe La atoms on the Sr sites in the $SrTiO_3$ thin film given that both cations occupy the *A*-site sublattice of the perovskite lattice. Likewise, Al atoms could occupy the Ti sites in the *B*-site sublattice. The effects of interdiffusion is considered in Fig. **??** for the *n*-type interface layering. Here we explicitly consider the case of both symmetric diffusion on both sublattices[**?**], as well as enhanced diffusion on each individual sublattice.

As shown in Fig. **??**(b), with equal interdiffusion on both lattice sites, the diverging potential follows an identical profile to that for an atomically abrupt interface pictured in Fig. **??**(a). When the *A*-site sublattice is interdiffuse, but the *B*-site atomically abrupt as shown in Fig. **??**(c), there is an additional offset to the potential. While the slope of the diverging potential remains constant, the offset leads to a larger value of a potential at each lattice site. In contrast, enhanced diffusion on the *B*-site sublattice as shown in Fig. **??**(d) leads to an offset in the potential which reduces the magnitude at each layer position. We note that considering different diffusion profiles on the *A*-site and *B*-site sublattices is not purely an academic exercise as shown in Chapter 5 where the *B*-site lattice more abrupt than the *A*-site as shown in Fig. **??**. Finally, we note that the profile of the potential in Fig. Fig. **??**(d) suggests that the polar catastrophe

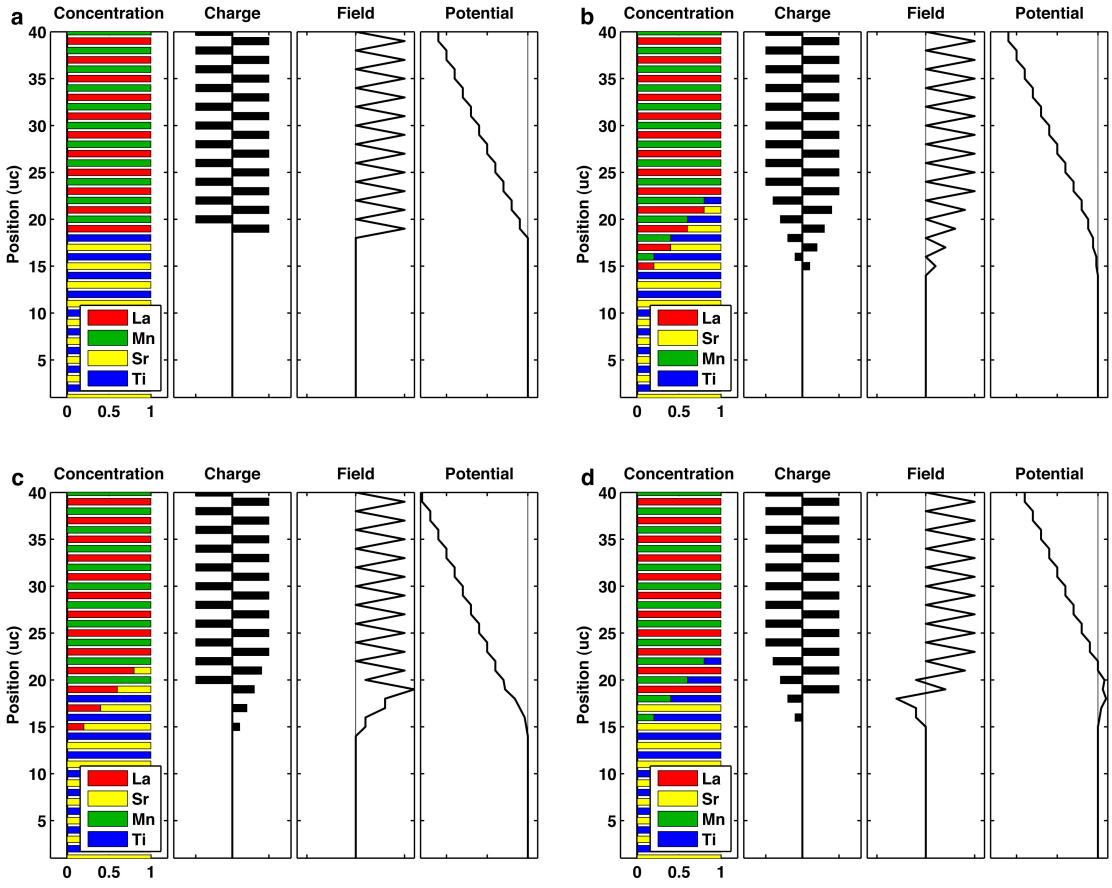

Figure 2.4: The polar catastrophe for the *n*-type $LaMnO_3/SrTiO_3$ interface. The elemental concentrations of La, Mn, Sr and Ti, the charge per unit cell and the resulting electric field and electric potential are plotted for: (a) an atomically abrupt interface; (b) an interface with both *A*-site and *B*-site interdiffusion; (c) a diffuse *A*-site sublattice with an abrupt *B*-site lattice; and (d) a diffuse *B*-site sublattice and an abrupt *B*-site lattice. Diffusion on the *A*-site, as observed for the samples measured in this study, accelerates the divergence of the electric potential while excess diffusion on the B-site results in a slight reduction in the divergence. For all calculations, the total *A*-site concentration, La + Sr, and the total *B*-site concentration, Ti + Mn, are one for each layer.

could be cancelled for ultrathin films with a desired interdiffusion profile however the magnitude is not great enough for a film thickness of greater than one unit cell.

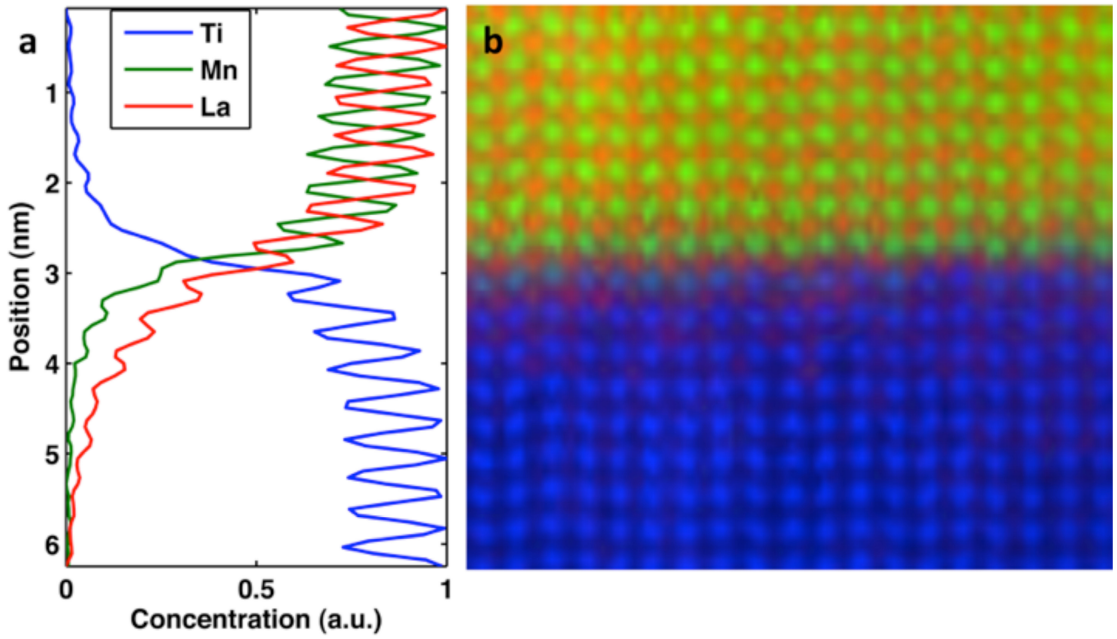

Figure 2.5: (a) Integrated elemental concentration across the $x = 0.1$ $La_{1-x}Sr_xMnO_3/SrTiO_3$ interface from the spectrum map shown in (b). The La signal persists further into the substrate than the Mn signal indicating more interdiffusion on the *A*-site sublattice than the *B*-site.

Finally, we note that some groups have suggested that conductivity observed at the $LaAlO_3/SrTiO_3$ at the interface can be attributed to interdiffusion.[**?**] While the novel magnetic phases observed at this interface are not present in the $La_{1-x}Sr_xTiO_3$ phase diagram, $La_{1-x}Sr_xTiO_3$ is conducting for a range of x values. Chapter 4 will investigate a series of samples with a range of interdiffusion profiles and show systematically that there is no correlation between the degree of lanthanum interdiffusion and the interface properties observed.

2.1.2 Polar Catastrophe in the presence of cation and oxygen vacancies

As discussed above, the $SrTiO_3$ substrate is known to accommodate oxygen vacancies which gives rise to itinerant electrons[**?**, **?**] and enhanced conductivity. As shown in Fig. **??**, the presence of oxygen vacancies screen the polarization catastrophe for *p*-type interfaces, yet not for the corresponding *n*-type interfaces. However the addition of oxygen vacancies to a conducting *n*-type interface could cause additional mobile charge carriers; many groups suggested that oxygen vacancies induced by kinetic bombardment of the PLD ablated species or low background pressures of oxygen during growth could be responsible for the observed conductivity.[**?**, **?**]. Further work has suggested that oxygen vacancies induced during growth can lead to an enhancement in the total charge carriers–notably beyond the number required to screen the polarization catastrophe as discussed above. For example, conducting atomic force microscopy (c-AFM) found that the conducting channels of a $LaAlO_3/SrTiO_3$ system grown in highly reducing conditions extended past 1 μ into the substrate[**?**]. Further post-growth annealing in a high-oxygen environment reduced the number of mobile charge carriers and confined them to within nanometers of the interface, consistent with the resolution limit of the probe. Thus, there seems to be an interplay between charge carrier concentration and oxygen vacancies. In the absence of oxygen vacancies, a small concentration of charge carriers persist due to the compensation of the polar catastrophe.

In contrast, the cations are positively charged and cation vacancies in the absence of a change in the oxygen stoichiometry could result in the desired charge balance. Figure **??** models an atomically-abrupt stoichiometric interface and an

an atomically-abrupt interface missing 1/6 of the interfacial La atoms in (a) and (b) respectively. Note that as the La atom assumes the "+3" oxidation state, 1/6 of an atom corresponds to the desired 0.5 $e-$ electronic charge. An equivalent calculation could have been performed with vacancies residing on the *B*-site sublattice. Chapter 4 will give experimental evidence for the presence of localized cation vacancies and the result on the electronic properties for a series of $LaAlO_3/SrTiO_3$ interfaces.

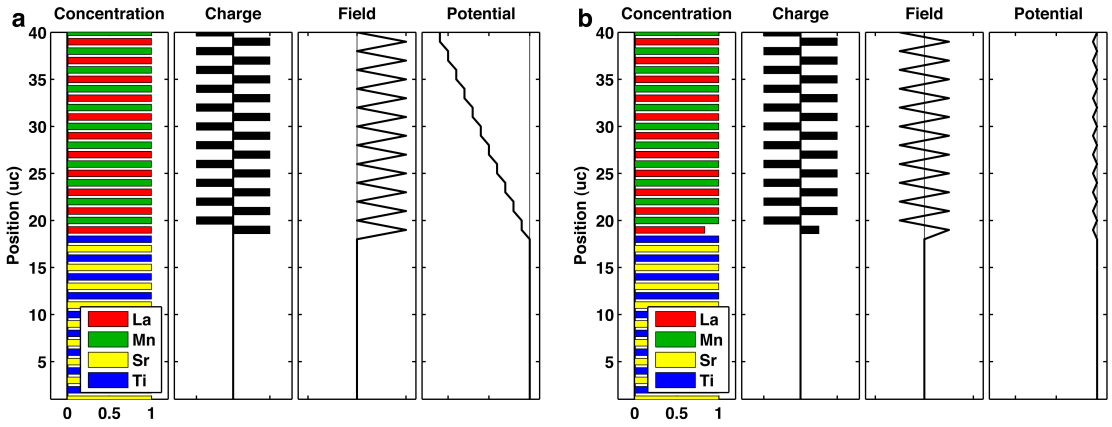

Figure 2.6: The polar catastrophe for the *n*-type $LaMnO_3/SrTiO_3$ interface. The elemental concentrations of La, Mn, Sr and Ti, the charge per unit cell and the resulting electric field and electric potential are plotted for: (a) an atomically abrupt interface; (b) an atomically abrupt interface with 1/6 of the interfacial La atoms missing without a corresponding change in the oxygen stoichiometry.

2.1.3 Polar Catastrophe in the presence of lattice distortions

There is a sharp onset in the conductivity at the *n*-type $LaAlO_3/SrTiO_3$ interface with film thickness: conductivity is only observed for films thicknesses of ≥ 4 unit cells[**?**] and superlattices of the same periodicity.[**?**] In principle, the polar catastrophe should scale linearly with the film thickness and excess charge should travel to the interface for any film thickness. Theoretical work has sug-

gested that the polar [LaO] and [AlO_2] layers buckle, creating a polar-type distortion which adds an electrostatic dipole.[**?**] This distortion can counteract the interface polarization and allows the system to remain insulating for the first few unit cells. While polar distortions are not the subject of the work presented in this thesis, these structural distortions driven by the polar catastrophe at the interface can also impact the electronic properties in the absence of electronic changes.

2.2 Quantifying Electronic Changes at Oxide Interfaces with Electron Microscopy

The above section described the electronic states that can be stabilized as at the interface between a polar and non-polar perovskite oxide. To analyze these interfaces we would like to quantify intrinsic electronic changes at with atomic resolution. However, we also need to be simultaneous sensitive to to extrinsic defects such cation or oxygen vacancies, structural distortions etc given the interplay between the intrinsic and extrinsic factors. The data presented in this thesis was collected by a combination of scanning transmission electron microscopy (STEM) and electron energy loss spectroscopy (EELS). Interfacial changes in the composition and bonding information can be exquisitely probed at the atomic scale with these tools. This section will give a brief overview of the theory behind the technique.

2.2.1 HAADF-STEM imaging

In the current generation of electron microscopes, 100 keV - 300 keV electron beams can be focused down and fired through thin ($< 0.1\mu$) samples.[**?**] The development of multipole-base aberration correctors has further reduced the resolution to sub-Å.[**?**, **?**] An annular dark field (ADF) image is formed by scanning this beam across the thin sample and collecting the electrons which scatter to high angles on an annular dark field detector. Similar to Rutherford scattering, the fraction of electrons scattered to the ADF detector scales with the atomic number (Z) as approximately $Z^{1.7}$.[**?**, **?**, **?**] An example of a HAADF-STEM of a $LuFeO_3$-$LuFe_2O_4$ superlattice is shown in Fig. **??**. Due to the atomic number difference between Fe (Z = 26) and Lu (Z = 71), there is clear contrast between the two atomic columns with the Lu atoms appearing brighter. Here, the 0.4 Å ferroelectric displacement of the Lu atoms in the $LuFeO_3$ layers can easily be observed as well as the damping of these distortions in the $LuFe_2O_4$ layers. Thus, HAADF-STEM can provide information regarding structural and compositional properties of oxide systems.

2.2.2 Electron energy loss spectroscopy

HAADF-STEM images are formed from the elastically scattered electrons. In addition to elastic scattering, the incident electrons can scatter inelastically following interactions with the sample.[**?**] These scattering events can cause the generation of plasmons (collective oscillations valence electrons by the field of the incident beam), radiative losses and core-level transitions. The EELS spectrometer disperses the inelastically scattered beam according the energy loss

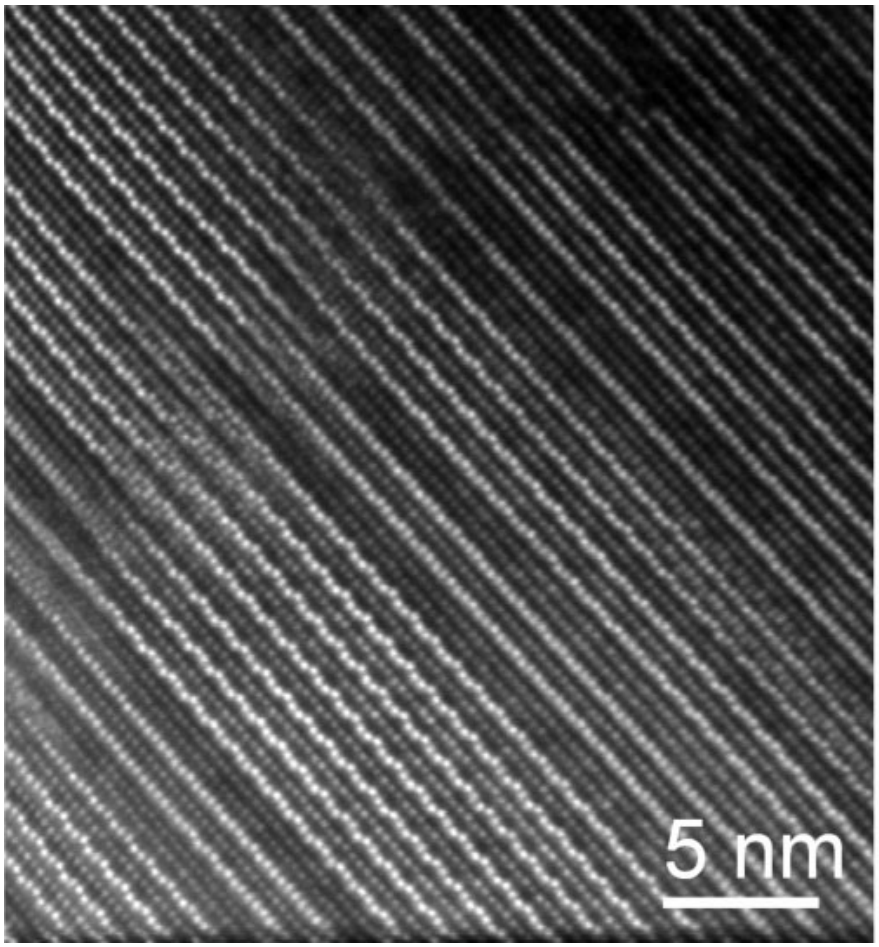

Figure 2.7: HAADF-STEM image of a $LuFeO_3$-$LuFe_2O_4$ superlattice.

and can measure losses of the incident electron beam energy with up to 100 meV resolution using monochromated sources (typical EELS resolution is 0.6 eV for measurements in this thesis). Following the ”zero-loss” peak, the peak corresponding to the incident electrons which did not scatter inelastically with the sample, the first ~50 eV is deemed the ”low-loss” region of the spectrum. These transitions are dominated by bulk and surface plasmons as well as excitations of the valence electrons. These transitions are delocalized on the atomic scale[**?**, **?**] and are thus not the focus of the work in this thesis.

Theory of EELS scattering

Ionization of the core-level electrons occurs after ~50 eV. Here, the swift electrons in the incident beam excite electrons in the deeply-bound core energy levels of the sample to the unoccupied orbitals above the Fermi level. Given that the core-level binding energies are distinct for each element, this signal gives a site-specific measurement of the elemental composition of the sample. The scattering cross-section for these transitions can be explicitly calculated from the transition rate.[**?**]

Fermi's golden rule gives the transition rate, $\Gamma_{i^* \to f^*}$ for the excitation of the core-level electron with an energy loss ΔE:

$$\Gamma_{i^* \to f^*} = \frac{2\pi}{\hbar} | < f^* | V | i^* > |^2 \delta(E_i - E_f - \Delta E) \tag{2.1}$$

Here $|i^* >$ and $f^* >$ are the initial and final states of the system with energy E_i and E_f respectively. Note that the states include that of both the incident electron beam and the electron in the solid sample. The interaction potential, V, follows the Coulomb potential:

$$V = \frac{-e^2}{\vec{r'} - \vec{r}} \tag{2.2}$$

where $\vec{r'}$ and $\vec{r}$ are the coordinates of the incident and target electrons. The initial and final states of the system are composed of the states of both the incident electron beam as well as the target electron in the solid. Due to the negligible overlap, we can consider the state as the product of the ground state wavefunction of the target electron and plane wave incident beam. The incident state can thus be written:

$$|i^* >= e^{-\vec{k_i} \cdot \vec{r'}} |i > \tag{2.3}$$

And the final state as:

$$|f^* >= e^{-\vec{k_f}\cdot\vec{r'}}|i > \tag{2.4}$$

where $|i>$ and $|f>$ are the initial and final wavefunctions of the target electron and $\vec{k_i}$ and $\vec{k_f}$ the initial and final momentum of the incident electron. Substituting these expressions into the equation for the transition rate, we have:

$$\Gamma_{i^*\to f^*} = \frac{-2\pi e^4}{\hbar}| < f|\frac{e^{i(\vec{k_f}-\vec{k_i})\cdot\vec{r'}}}{|\vec{r'}-\vec{r}|}|i > |^2\delta(E_i - E_f - \Delta E) \tag{2.5}$$

We first simplify this by defining a new variable, $\vec{q} = \vec{k_f} - \vec{k_i}$.

$$\Gamma_{i^*\to f^*} = \frac{2\pi e^4}{\hbar}| < f|\frac{e^{i\vec{q}\cdot\vec{r'}}}{|\vec{r'}-\vec{r}|}|i > |^2\delta(E_i - E_f - \Delta E) \tag{2.6}$$

If we define a new variable $\vec{R} = \vec{r} - \vec{r'}$ then we have:

$$\Gamma_{i^*\to f^*} = \frac{2\pi e^4}{\hbar}| < f|\frac{e^{i\vec{q}\cdot\vec{r}}e^{i\vec{q}\cdot\vec{R}}}{|\vec{R}|}|i > |^2\delta(E_i - E_f - \Delta E) \tag{2.7}$$

This expression is now of the form that can be simplified using Bethe's integral $\int d\rho e^{i\vec{K}\cdot\vec{\rho}} = \frac{4\pi}{K^2}$ to perform the integration over $\vec{R}$.

$$\Gamma_{i^*\to f^*} = \frac{32\pi^3 e^4}{\hbar}| < f|\frac{e^{i\vec{q}\cdot\vec{r}}}{q^2}|i > |^2\delta(E_i - E_f - \Delta E) \tag{2.8}$$

Using this expression for the transition rate, we can find the differential scattering cross-section, $d^2\sigma/dEd\Omega$, using:

$$\frac{d^2\sigma}{dEd\Omega} = \frac{m_e^2}{2\pi\hbar^3}\frac{k'}{k}\sum_{i,f}\Gamma_{i,f} \tag{2.9}$$

leaving:

$$\frac{d^2\sigma}{dEd\Omega} = \frac{16\pi^2 m_e^2 e^4}{\hbar^4}\frac{k'}{k}\sum_{i,f}| < f|\frac{e^{i\vec{q}\cdot\vec{r}}}{q^2}|i > |^2\delta(E_i - E_f - \Delta E) \tag{2.10}$$

The Bohr radius, a_0, is given by $a_0 = 4\pi\hbar^2/m_e e^2$ and thus we have:

$$\frac{d^2\sigma}{dEd\Omega} = \frac{4}{a_0^2}\frac{k'}{k}\sum_{i,f}| < f|\frac{e^{i\vec{q}\cdot\vec{r}}}{q^2}|i > |^2\delta(E_i - E_f - \Delta E) \tag{2.11}$$

The exponential can be expanded using a Taylor series in the approximation $\vec{q} \cdot \vec{r} << 1$ and noting the orthogonality of the wavefunctions $< f|i >= 0$:

$$\frac{d^2\sigma}{dEd\Omega} = \frac{4}{a_0^2 q^4} \frac{k'}{k} \sum_{i,f} | < f|\vec{r}|i > |^2 \delta(E_i - E_f - \Delta E) \tag{2.12}$$

Thus the differential scattering cross-section is proportional to the matrix element, $< f|\vec{r}|i >$. The vector $\vec{r}$ is a first-order tensor. Applying the Wigner-Eckhart theorem, the matrix element vanishes unless the transition from initial to final state has an angular momentum transition from l to $l \pm 1$. The initial states, $|i >$, are usually localized allowing us to express the final states, $|f >$, in this basis. Doing so, we can define matrix elements $M_{l+1} =< f_{l+1}|r|i_l >$. Assuming that the matrix elements varying slowly with k as is true for an atomic-like basis, we can re-write the differential scattering cross-section as:

$$\frac{d^2\sigma}{dEd\Omega} \propto M_{l+1}^2 \rho_{l+1} + M_{l-1}^2 \rho_{l-1} \tag{2.13}$$

Here ρ_{l+1} is the final local density of states for the state with angular momentum $l+1$. Usually the matrix elements M_{l+1} are slowly varying and thus the scattering cross section is dominated by the local density of states (LDOS) of the final state.

Interpretation of EELS fine structure for core-loss transitions

For single particle excitations, the energy loss due to inelastic scattering from these core-level transitions provides a site-specific measurement of the LDOS above the Fermi level, partitioned by chemical species and angular momentum due to the dipole selection rules.[**?**] For transition metal $L_{2,3}$-edges of interest in this thesis however, there can be significant deviations to this simple picture due to the perturbations to the LDOS due to the core-hole effect[**?**], multiple

scattering[**?**] and other many body effects. Nevertheless, comparison to reference spectra has permitted identification of the oxidation state of these materials in two-dimensions.[**?**, **?**, **?**]

The perovskite transition metal $L_{2,3}$ edges of particular interest nominally includes transitions from the $2p$ states to the $4s$ and $3d$ DOS. Due to the negligible overlap between the $4s$ and $2p$ states, these transitions are dominated by the $2p$ to $3d$ transition.[**?**] A cartoon spectra of the transition from the $2p^6 3d^0 \rightarrow 2p^5 3d^1$ as might be expected for the Ti^{+4} state in $SrTiO_3$ is shown in Fig. **??**.[**?**] The single transition is split into the separate L_2 and L_3 lineshapes due to the spin-orbit coupling in the initial $2p$ creating distinct transitions from $2p_{1/2}$ and $2p_{3/2}$. Due to the $(2j+1)$ degeneracy of these final states, the expected branching ratio of the L_2 to L_3 is 1:2.

Solid-state effects also strongly perturb the observed lineshape of the $L_{2,3}$-edge. The final state of the $3d$ is not symmetric and is split by the crystal-field splitting of the perovskite lattice. As shown in the cartoon in Fig. **??**, the octahedral coordination of the oxygen atoms around the transition metal splits the energy levels of the d unoccupied orbitals. The lower overlap of the d_{xy}, d_{xz} and d_{yz} orbitals and the oxygen orbitals leads to the lower lying antibonding t_{2g} states. In contrast, the stronger overlap between the $d_{x^2-y^2}$ and d_{3z^2-1} orbitals leads to a higher lying e_g states. The transition of these $2p$ electrons to these split $3d$ levels leads to an additional splitting of the $L_{2,3}$ edge as shown in the final line of Fig. **??**. Note that the observed splitting of both the L_2 and L_3 edges is related to, yet not equal to, the crystal field splitting between the t_{2g} and e_g states.[**?**]

Several deviations are still observed between the spectra shown in Fig. **??**

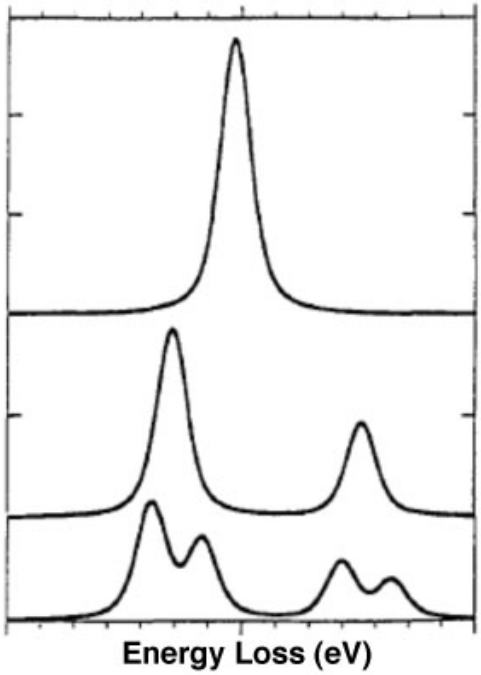

Figure 2.8: A sample $L_{2,3}$ lineshape. In the second line, a single peak is split due to the spin-orbit coupling split of the initial $2p$ states. The final line shows an additional splitting due to the crystal-field splitting of the final state d orbitals in a transition metal oxide. Reproduced from [**?**]

and the experimentally observed spectra as shown in Fig. **??**(c). The Ti^{+4} spectra shown for $SrTiO_3$ shows a more intense L_2 peak in contrast to the predicted branching ratio. This deviation can be attributed to the multiplet effects and the 3d spin-orbit coupling.[**?**] This aside, the fine structure shows four clear peaks which can be attributed to the spin-orbit and crystal-field splitting. The Ti^{+3} peak imaged for $LaTiO_3$ does not show a strong crystal-field splitting. For the Ti^{+3} atom, the initial state has a $2p^6 3d^1$ configuration and thus there are a greater number of final states accessible to the system.[**?**]

Further calculation efforts of the near-edge fine structure of transition metals include a variable to include for the degree of covalency in the material and explicit inclusion of the core-hole effect. This aside, the EELS spectra are still

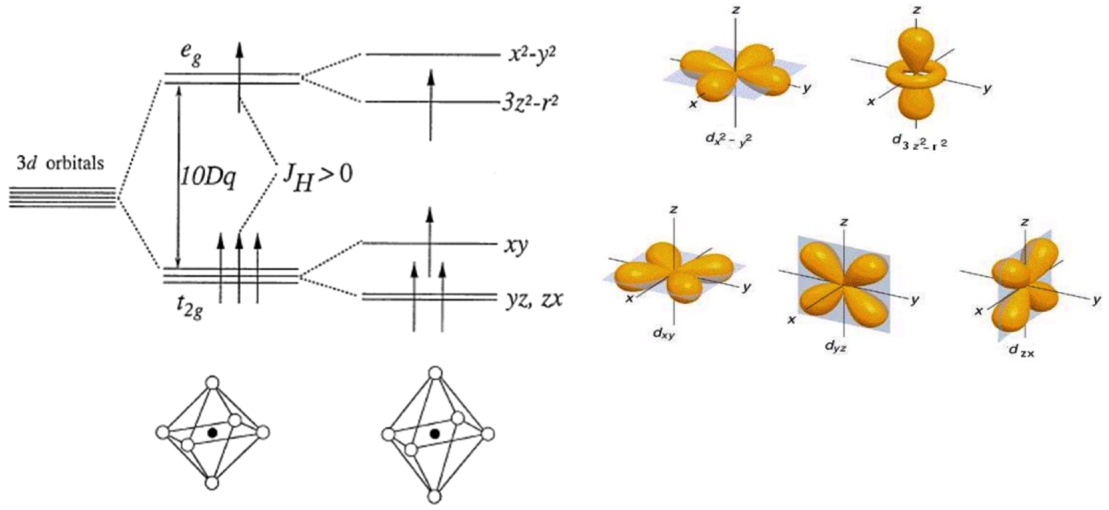

Figure 2.9: The octahedral environment of the oxygen atoms breaks the orbital degeneracy of the 3*d* orbitals in a transition metal into the t_{2g} and e_g levels. For this compound, there is a further Jahn-Teller distortion and subsequent splitting of the energy levels to remove the degeneracy of the e_g state. Reproduced from [**?**]

powerful tools to determine the atomic structure of materials by comparing the measured EELS spectra to a fingerprint for a valence state. As shown in Fig. **??**(c), the Ti^{+3} and Ti^{+4} show distinct lineshapes and onset energies. Given that the EELS fine structure is primarily sensitive to the nearest neighbor coordination, the fine structure can provide an atomic-resolution probe of the local bonding.

2.3 Conclusions

In this chapter, we presented the polar catastrophe model for understanding the electronic changes which can occur at the interfaces between polar and nonpolar materials. In addition to the simple cartoon, we explicitly considered the effects of interdiffusion, cation stoichiometry and lattice perturbations on the

expected electronic structure. Chapter 4 will explore the $LaAlO_3/SrTiO_3$ interface in detail and will show the strong dependence of the interface properties on the local deviations in cation stoichiometry. Chapter 5 will look at series of $La_{1-x}Sr_xMnO_3/SrTiO_3$ and will determine the regions on the phase diagram where we observe a quantitative agreement between the charge transfer predicted by the polar catastrophe model and where the model does not apply.

We also presented the theory of electron energy loss spectroscopy which will form the basis for the atomic-resolution concentration and valence measurements in the remainder of the thesis. Chapter 3 will demonstrate the use of the O-*K* to map the local bonding environment of the oxygen atoms in a superlattice with atomic level sensitivity. The fine structure of the transition metal iron, titanium and manganese spectra $L_{2,3}$ edges will be compared to fingerprint spectra and used to map the valence states of these multivalent cations throughout the thesis.

CHAPTER 3

ATOMIC-RESOLUTION MAPPING LOCAL BONDING ENVIRONMENT OF OXYGEN IN NATURAL SUPERLATTICE $LuFe_2O_4$

3.1 Introduction

Transition metal oxides display a host of properties from ferroelectricity and ferromagnetism to high-temperature superconductivity. While varied in structure and composition, the ubiquitous backbone is the cage of oxygen atoms surrounding the transition metal cation. Small distortions such as tilts and rotations of the oxygen octahedron or tetrahedron can dramatically impact the properties of the material. Current computational studies are attempting to harness these octahedral rotations to engineer materials with desired properties.[**?**, **?**, **?**, **?**] Thus, accurately determining the position and local bonding environment of the oxygen atoms experimentally is crucial in correlating the structure to the macroscopic properties.

Advances in aberration correction have made electron energy loss spectroscopy (EELS) on a scanning transmission electron microscope (STEM) a powerful tool for probing elemental concentrations at the atomic scale. For transition metal $L_{2,3}$ edges strong core-hole effects produce a significant deviation between the local density of states (LDOS) and the observed energy-loss near-edge fine structure (ELNES); nevertheless, comparison to fingerprint spectra has permitted atomic resolution two-dimensional maps of oxidation state of transition metal and lanthanide cations using EELS. In contrast to the transition metal $L_{2,3}$ edges, the oxygen K edge ELNES can be more simply related to the LDOS as the oxygen $2p$ electrons mostly screen the 1s core hole. The result is

a distorted but often recognizable reflection of the ground state LDOS.[**?**, **?**] In a tight-binding decomposition, the bulk of the O $2s$ and $2p$ states are occupied and thus much of the oscillator strength on the O-K edge is composed of states that can be attributed to overlap with the neighboring sites. As such, the O-K edge is rich with information about the system and in particular can be sensitive to the number of d holes if bonded to transition metals, and more generally the nearest-neighbor bonding to cations, including those for which the EELS edges lie outside the energy range accessible by current spectrometers.[**?**, **?**, **?**]

Oxygen spectroscopic images, however, can be difficult to obtain due to the inherently low jump ratio of the edge and often require substantial post-acquisition data processing.[**?**] This not only can produce artifacts in a concentration map that can be mistaken for channeling contrast, but also alters the fine structure of the EELS signal.[**?**] Improved optics on the current generation of spectrometers allows for greater collection efficiency and thus more signal, making the O-K edge more accessible. Here, we present EELS spectral maps of the oxygen atoms in $LuFe_2O_4$ and probe the local bonding environment through atomic-resolution analysis of the O-K edge fine structure. We show that direct maps of the oxygen positions and local environment can be obtained, even in the presence of heavy cations. We find that attempts to enhance the signal using the popular principal components analysis distorted the bonding maps.

We investigate thin films of $LuFe_2O_4$, purported to be the highest temperature known simultaneous ferroelectric ferrimagnet.[**?**] The ferroelectricity was attributed to charge ordering on the iron sites[**?**] which allows for a polarization without precluding magnetism. A recent series of studies, however, have suggested that $LuFe_2O_4$ is not ferroelectric[**?**, **?**, **?**] and that while both Fe^{+2}

and Fe^{+3} formal valences are present, the charge arrangements result in a non-polar structure.[**?**] It is worth noting that while distinct iron valence states have been observed in the bulk[**?**] and superlattice reflections which could be consistent with charge ordering have been observed in TEM diffraction,[**?**] a direct measure of the iron valence atomic column by atomic column remains elusive. $LuFe_2O_4$ has a layered hexagonal structure, $R\bar{3}m$, consisting of planes of Lu-O (U layers[**?**]) alternating with double planes of Fe-O (W layers[**?**]). There are two distinct oxygen sites in the crystal.[**?**] The oxygen atoms that sit slightly above and below the iron planes, O_1, are surrounded by four iron atoms with a long bond to a lone lutetium atom in an asymmetric trigonal bipyramid structure. In contrast, the remaining oxygen atoms, O_2, are surrounded by a roughly tetrahedral cage of three lutetium atoms and a single iron atom. The O-K edge probes the hybridization of the O p orbitals to the Lu and Fe d orbitals, thus we can observed distinct EELS fine structure fingerprints from O_1 and O_2.

3.2 Experimental Techniques

3.2.1 Adsorption-controlled growth of $LuFe_2O_4$

Thin films of $LuFe_2O_4$ were grown on (111) $MgAl_2O_4$ by reactive oxide molecular-beam epitaxy in a Veeco GEN 10. The film was grown at 890° C and an oxygen pressure of 1×10^{-6} T. A excess of iron was provided (iron flux equal to approximately four times that of lutecium); at these adsorption-control conditions, iron is volatile and the excess iron beyond that required for a stoichiometric film desorbs. X-ray diffraction (XRD) presented in citation indicate that the

films are indeed single phase and (0001) oriented. Magnetization experiments showed a magnetic moment of 0.3 μ_B per iron atom at 70 kOe.

3.2.2 EELS Mapping of Bonding Changes

Spectroscopic images of cross-sectional TEM specimens were performed on a 100 keV Nion UltraSTEM, a 5^{th} order aberration corrected microscope optimized for EELS spectroscopic imaging with a probe size of 1 Å, EELS energy resolution of 0.6 eV and a high usable beam current. Simultaneous maps of Lu, Fe, and O were acquired with a 1 eV/channel dispersion and maps revealing fine structure with 0.3 eV/channel. Calculations of the EELS fine structure of $LuFe_2O_4$ were performed with FEFF with 100 keV incident electrons, convergence and collection angles of 30 and 80 mrad, respectively, to match the experimental conditions. Core-hole effects, and a 0.2 eV energy broadening were included. Ground state LDOS were also calculated using Wien 2k, which provides a more accurate treatment of the near-edge features.

3.3 Results and Discussion

3.3.1 Bonding Changes in O-Kedge

Figure **??** shows a two-dimensional atomic resolution spectroscopic image of $LuFe_2O_4$ oriented along the [110] zone axis of the film. The film is single phase and well ordered as shown in the HAADF-STEM image, Fig. **??**(a). The EELS spectroscopic image, Fig. **??**(b)-1(e), simultaneously resolves the atomic posi-

tions of all the elements in the film using the Lu-$M_{4,5}$, Fe-$L_{2,3}$, and O-K edges. The simultaneously recorded ADF signal is shown for comparison in Fig. **??**(f). The concentrations plotted are obtained using a simple power law background subtraction and integration over the edge without additional noise reduction techniques. A small amount of intermixing between the iron and lutetium sublattices is observed in the EELS map. This may reflect step edges viewed in projection or genuine anti-site defects. Finally, as test of sensitivity, we note that the oxygen atoms sit 0.25 Å above and below the iron atoms in the Fe-O planes in the bulk crystal structure. This is clearly apparent in overlaid image, Fig. **??**(b).

In addition to mapping the concentration of oxygen atoms, the fine structure of the O-K edge can be used to map the local bonding environment with atomic resolution as shown in Fig. **??**. The oxygen signal, integrated in Fig. **??**(b), was extracted from a representative region of the film, shown in Fig. **??**(a). Analysis of the fine structure of the EELS signal produced two distinct components, shown in Fig. **??**(c). A non-negative non-linear least squares fit of these components to the full spectrum map, Fig. **??**(d), reveals the oxygen fine structure is clearly bifurcated into distinct concentrations of oxygen atoms in the Fe-O layers, O_1, and those in the Lu-O layers, O_2. Finally, we note that all analysis was performed without the application of the popular weighted principal component analysis (w-PCA) filter. We find the use of the filter severely distorts the concentration maps, Fig. **??** even when an excess of components well beyond that suggested by the scree-plot criterion are used. Similar artifacts have been observed for one-dimensional concentration profiles.[**?**] These artifacts are reminiscent of those observed in previous attempts to map the local bonding structure with oxygen which was attributed to fundamental limita-

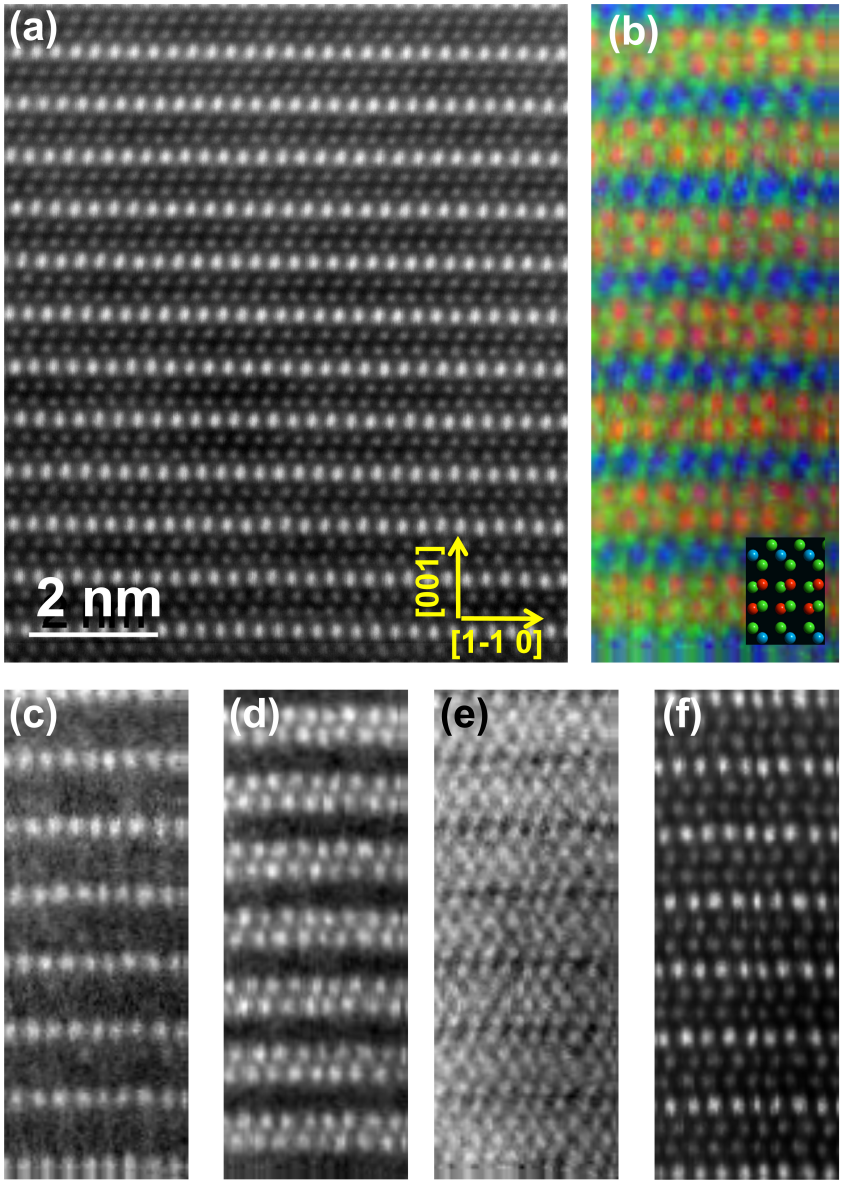

Figure 3.1: Compositional mapping of $LuFe_2O_4$ viewed along the [110] zone axis. (a) HAADF-STEM image showing the repetition of Lu layers separated by double layers of Fe. The EELS spectroscopic composition image, (b), is an overlay of the Lu-$M_{4,5}$ (c), Fe-$L_{2,3}$ (d) and O-K (e) signals. In (b), Lu is plotted in blue, Fe in red, and O in green. The inset shows the bulk $LuFe_2O_4$ crystal structure color-coded accordingly. The ADF image recorded simultaneously with the EELS map is shown in (f). Images (b)-(f) are 70 x 186 pixel images with a field of view of 2.8 nm by 7.4 nm and were acquired with 40 msec/pixel.

tions from channeling, delocalization and thermal diffuse scattering. [?] Here we show that at moderate sample thicknesses these need not be fundamental limits and direct maps can be obtained, even in the presence of heavy elements. We would caution against using PCA filtering on raw data, especially when the peak-background ratio (or signal/noise ratio as defined in [?]) is low.

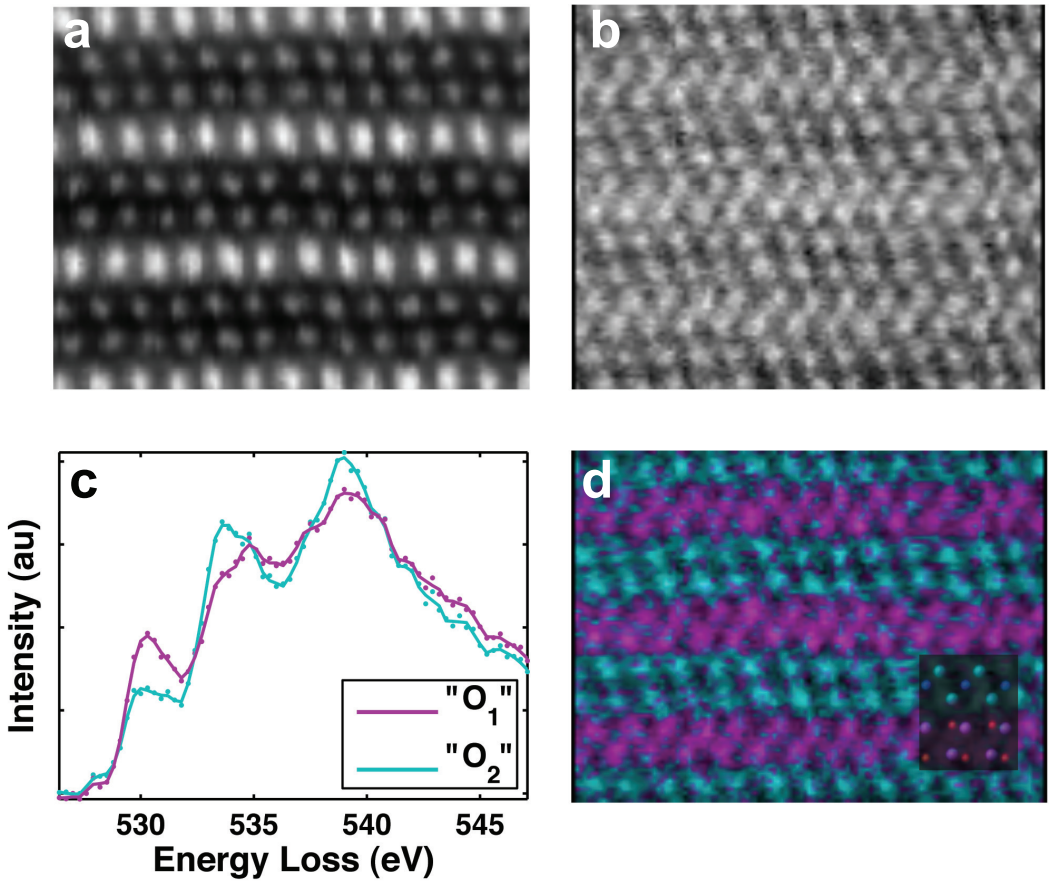

Figure 3.2: Local bonding information extracted from the O-*K* edge. (a) HAADF-STEM image recorded simultaneously with the oxygen concentration map of (b). Two distinct components were present in the O-*K* edge fine structure, (c), and fit to the spectroscopic image as shown in (d). The inset to (d) shows the crystal structure with iron plotted in red, lutecium in blue, and O_1 and O_2 in magenta and turquoise respectively. (a), (b), and (d) are 123 x 91 pixel images with a field of view of 3.4 nm by 2.5 nm and were acquired with 40 msec/pixel.

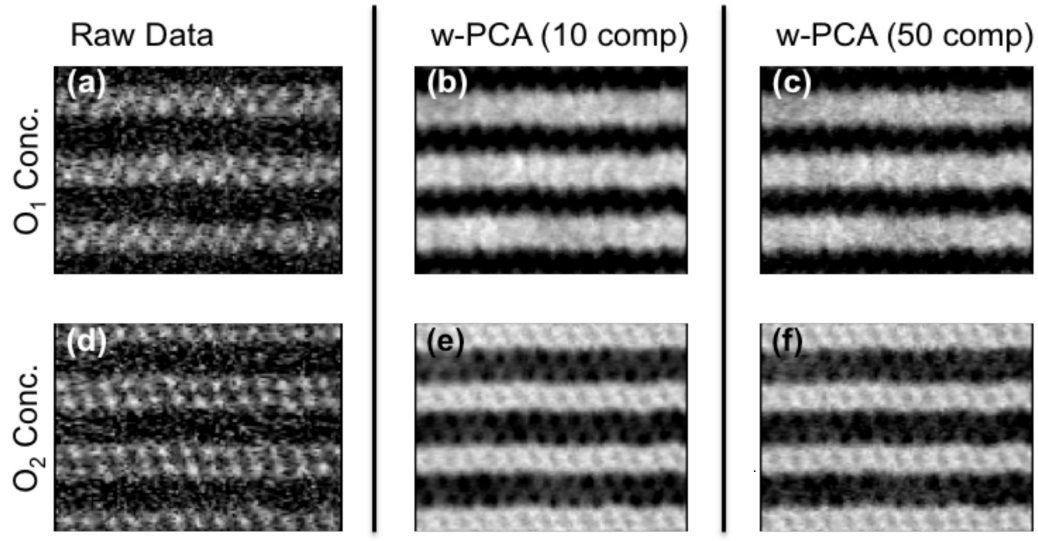

Figure 3.3: Impact of the weighted-PCA analysis on the concentration mapping. The extracted spectra from Fig. **??**(c) were fit to the raw data (reproduced from Fig. **??**(d)), the data after w-PCA with 10 components and the data after w-PCA with 50 components in (a) and (d), (b) and (e), and (c) and (f), respectively. The Scree plot requires only 5 components, however, even with 50 components there are significant artifacts present in the concentration mapping with a non-negligible concentration of O_2 off the O_2 sites.

3.3.2 Calculations of the O-K edge

To understand the origin of the peaks, simulations with FEFF9 were performed. FEFF is an *ab – initio* self-consistent multiple-scattering code based on a real space Green's function approach that calculates the excitation spectra and electronic structure in the presence of a core hole. [**?**, **?**] Because we do not detect the characteristic (1/3,1/3,half integer) diffraction peaks characteristic of structural charge ordering in our samples, we model the system in the unordered state where the all the iron sites have the same oxidation state.[**?**] Unlike previous cluster calculations for this system, the iron oxidation state is consistent for all sites.[**?**] FEFF computes the extended fine structure over a wide energy range, though is less accurate for the very near edge structure, especially for the first

few eV of the edge due to its sensitivity to the position of the Fermi energy as a result of errors inherent in its use of the muffin tin potentials. For this reason, we checked our results with full-potential calculations using Wien 2k and again saw similar trends[**?**] as shown in Fig. **??** . We did not include a core hole in the Wien 2k calculations, indicating that the trends shown in Fig. **??** persist in the ground state.

The O *p*, Lu *d*, and Fe *d* density of states for the distinct oxygen sites O_1 and O_2 are shown in Figs. **??**(a) and **??**(b) respectively. The resulting EELS spectra are shown in Fig. **??**(c). The first peak at 533 eV, corresponding to the hybridization of the O *p* orbitals to the Fe *d* orbitals, is distinct for the two oxygen sites. As shown in the inset to Fig. **??**(c), O_1 has four iron nearest neighbors in contrast to one for O_2 . The calculated EELS signal in Fig. **??**(c), as well as the experimentally recorded spectra in **??**(c), shows a much stronger feature for the O_1 spectra in this energy range. In contrast, the second two peaks are primarily due to the overlap of the Lu *d* orbitals with the O *p* orbitals. Here, O_2 has three Lu nearest neighbors whereas O_1 has one, resulting in a stronger peak in this region for the O_2 spectra. Thus the signal can be used as a local fingerprint for the orbital hybridization between the oxygen atom and the surrounding cations. We have seen similar trends in non-spatially resolved measurements for the substitution of A-site cations in bulk perovskites[**?**], but here the measurements and observed changes are local and site specific.

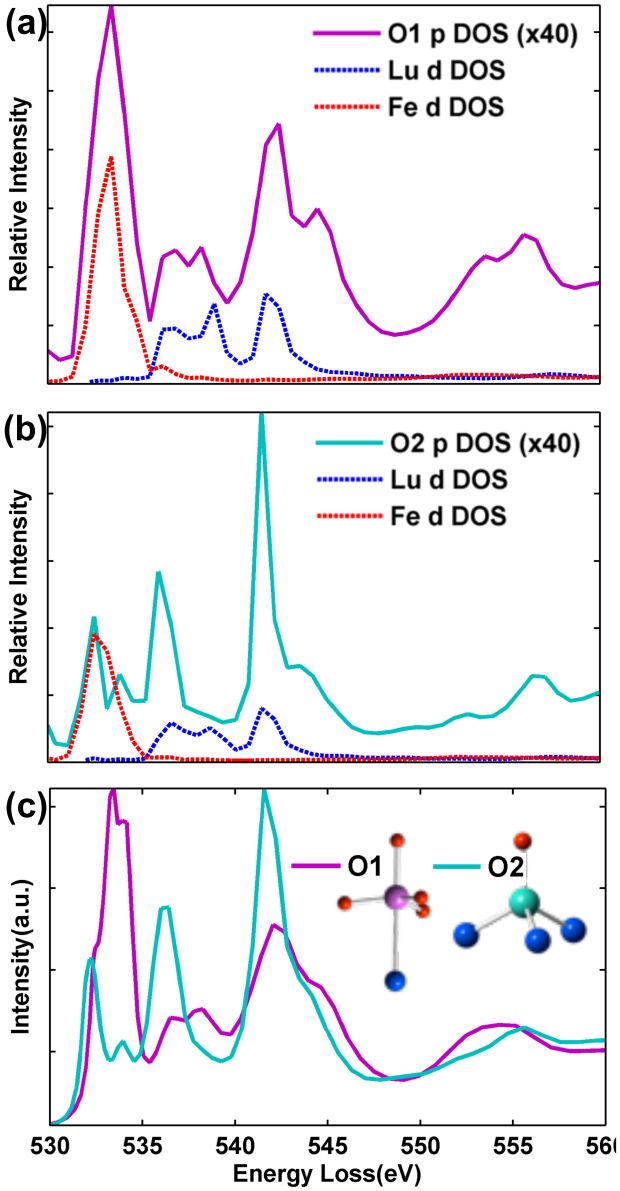

Figure 3.4: FEFF calculations of the EELS fine structure. The O *p* and Lu and Fe *d* local densities of states are shown for the distinct O_1 and O_2 sites in (a) and (b), respectively. In both cases, the much weaker O *p* LDOS tracks the combined Fe and Lu LDOS. The corresponding calculated EELS signal is shown in (c). A cartoon inset to (c) shows the local chemical environment of O_1 and O_2. Lu is plotted in blue, Fe in red, and the O atom in magenta and turquoise respectively.

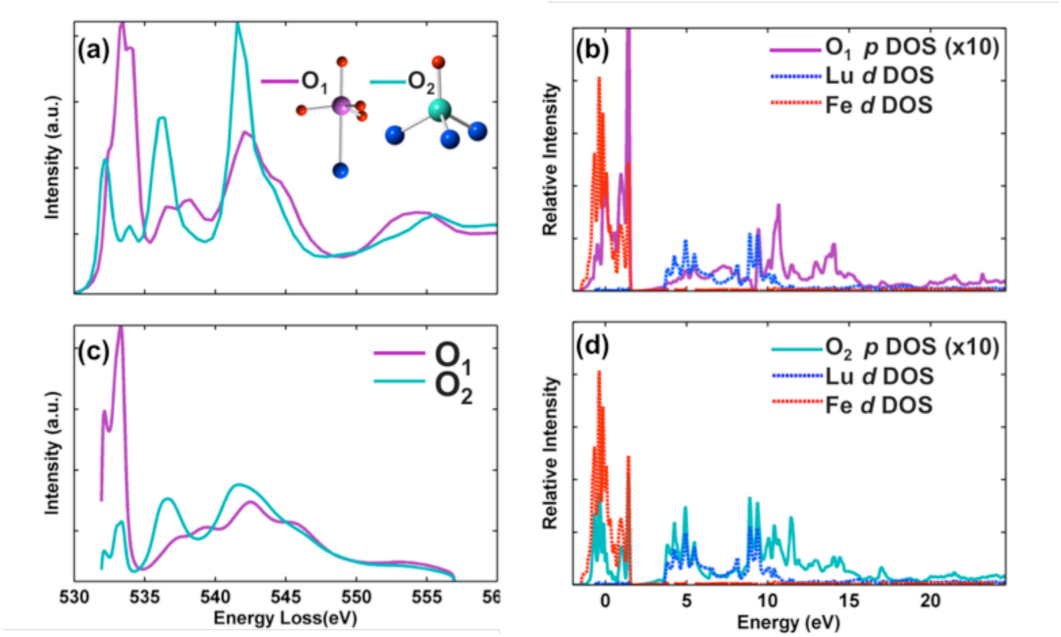

Figure 3.5: Comparison of the FEFF and Wien 2k calculations of the O-*K* edge EELS fine structure. The EELS signal for O_1 and O_2 calculated with FEFF is shown in (a), as reproduced from Fig. 3(c) and with Wien 2k in (c). The O *p* and Lu and Fe *d* local densities of states calculated with Wien 2k are shown for the distinct O_1 and O_2 sites in (b) and (d), respectively. In (b) and (d), energy 0 is the Fermi energy.

3.3.3 Iron Valence mapping to probe "charge-ordered ferroelectricity"

Finally, given that EELS is capable of probing bonding information with atomic resolution, we turn to investigate the sensitivity of EELS to proposed charge ordering arrangements on the iron sites. Similar to other transition metal cations, the Fe $L_{2,3}$-edge is sensitive to the valence with the onset energy shifting as the oxidation changes +2 to +3.[**?**, **?**] We image $LuFe_2O_4$ down the $[1\bar{1}0]$ zone axis of the crystal;[**?**] to increase the signal-to-noise, a full spectrum map was acquired, the Fe sites identified from the simultaneous ADF image and a mean spectrum generated from each atomic column. When these spectra are fit with Fe^{+2} and

Fe^{+3} references, only small fluctuations (a standard deviation of 0.09 $e-$) around a mean valence are observed as is shown in Fig. **??**. Notably, no consistent, reproducible charge-ordering pattern was discerned for our room temperature measurements in these films. This is consistent with the absence of ferroelectricity observed in the thin film. This also justifies the use of a single mean iron oxidation state for our calculations.

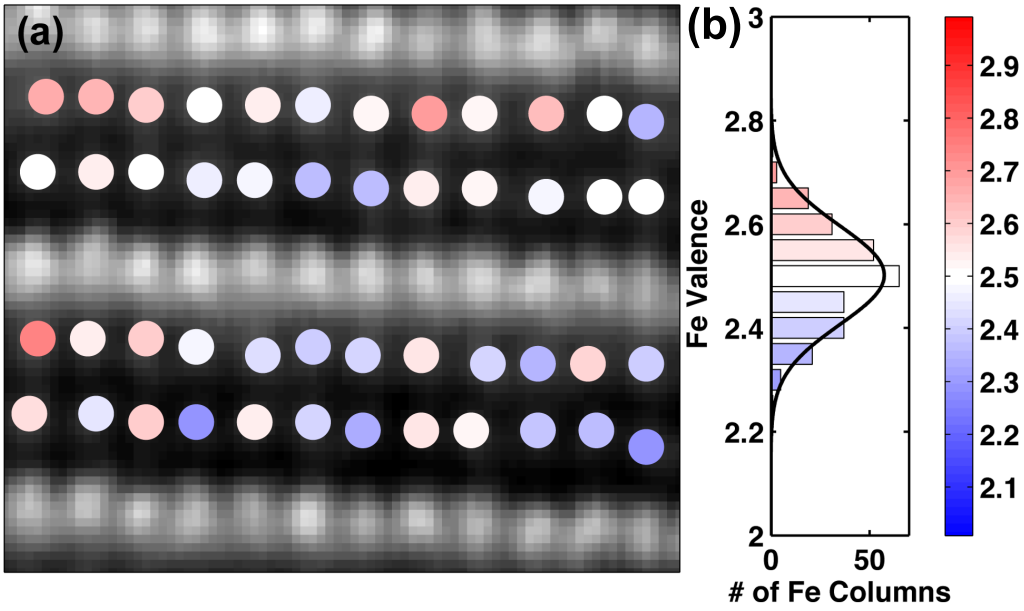

Figure 3.6: Measurement of the Fe oxidation state down $[1\bar{1}0]$ zone axis of the film. (a) ADF image on which the Fe valence obtained from an analysis of the Fe-$L_{2,3}$ edge fine structure is overlaid. Blue is used to indicate pure Fe^{+2} and red, pure Fe^{+3}. No consistent charge ordering pattern is observed. (b) A Histogram of Fe valences from all rows of panel (a) as well as other spectroscopic images with the same acquisition parameters (272 total Fe columns), showing a unimodal Gaussian distribution with a standard deviation of 0.09 e^{-}, placing a bound on the detection sensitivity for charge modulations, which should produce a bimodal distribution.

3.4 Conclusions

In summary, we have obtained atomic-resolution EELS spectroscopic images of all atomic species in a thin film of the multiferroic $LuFe_2O_4$. The EELS O-*K* edge fine structure was used to map changes in electronic structure in two-dimensions with atomic resolution, describing the local coupling of the oxygen 2*p* orbitals to the Fe and Lu *d* orbitals. Atomic-resolution mapping of the fine structure in the O-*K* edge should lend insight for other transition metal oxides. In particular, while Lu and Fe both had an accessible EELS edge, the O-*K* edge can also track nearest neighbor bonding to cations that have inaccessible EELS edges either due to overlap with another edge or a weak cross section as is the case for Sr, Ru, W, and Bi. Thus, the O-*K* edge fine structure analysis could provide an alternative pathway to mapping the concentrations of these elements in materials such as $BiFeO_3$ or $SrRuO_3$. Finally, while atomic-resolution valence mapping with a sensitivity of 0.09 $e-$ on the Fe sites did not show a consistent charge-ordering pattern in our sample, the demonstrated spatial resolution and valence sensitivity should prove useful for future exploring the O *K*-edge or the Fe charge ordering with EELS at low temperatures where the valence modulations should be more pronounced.

3.5 Acknowledgements

Growth and XRD analysis of the $LuFe_2O4$ thin films was performed by Dr. Charles M. Brooks and Prof. Darrell G. Schlom. Magnetic measurements were performed by Dr. Rajiv Misra and Prof. Peter Schiffer. FEFF and Wien2k calculations were performed by Qingyun Mao.

CHAPTER 4

LOCAL DEVIATIONS IN STOICHIOMETRY TO OFFSET THE POLAR CATASTROPHE

4.1 Introduction

The interface between transition metal oxides can support electronic phases not present in either parent compound. This is evidenced perhaps most interestingly by the discovery of conductivity,[**?**] and later superconductivity,[**?**, **?**] and novel magnetic phases[**?**] at the interface between two non-magnetic band insulators, $LaAlO_3$ and $SrTiO_3$. The creation of these novel electronic and magnetic phases is intriguing for device applications. Furthering the potential to include these materials in conventional silicon-based technologies, recent work has demonstrated the growth of the $LaAlO_3/SrTiO_3$ interface on Si as well as monolithically integrated NMOS logic circuits.[**?**]

As discussed in Chapter 2, the conducting two-dimensional electron liquid which forms at the interface is attributed to electronic charge transfer to the interfacial titanium sites to alleviate the polar catastrophe.[**?**, **?**, **?**] Despite considerable interest in the system, however, many questions remain regarding the role of defects on the properties of the system and in particular the interplay between extrinsic defects and the intrinsic electronic reconstruction. As discussed in Chapter 2, varied carrier concentrations have been reported–from those two orders of magnitude greater than that would be expected from valence changes to one order of magnitude lower.[**?**] It has even been claimed that the conductivity can only be attributed to extrinsic defects such as the following:

- La interdiffusion into the $SrTiO_3$ substrate, generated La-doped $SrTiO_3$. La-doped $SrTiO_3$ is a conductor and low temperature superconductor.[**?**, **?**]
- Oxygen vacancies in the $SrTiO_3$ substrate, induced during the growth in low oxygen pressure environments.[**?**, **?**]
- Oxygen vacancies in the $SrTiO_3$ substrate, generated by the surface treatment process of the native $SrTiO_3$ substrates prior to growth.[**?**]
- Bombardment of the $SrTiO_3$ substrate by high energy ablated species during the pulsed laser deposition growth.[**?**]

$SrTiO_3$ is known to easily accommodate oxygen vacancies which give rise to itinerant electrons and enhanced conductivity.[**?**, **?**] Moreover, all of the initial observations of conductivity at the $LaAlO_3/SrTiO_3$ interface were on the etched and annealed pre-treated $SrTiO_3$ substrate (rather than on *in – situ* grown STO_3) and with LAO_3 samples grown by pulsed laser deposition. While it is difficult to explain the sharp onset of conductivity at four unit cells of $LaAlO_3$, as reproduced by numerous groups around the world,[**?**] and the observation of novel magnetic phases,[**?**] not present in either parent compound or on the La:$SrTiO_3$ phase diagram, the balance of extrinsic to intrinsic causes for the conducting interfaces remained contentious.

Here, we investigate a series of samples grown by molecular beam epitaxy to show the interplay between extrinsic defects and intrinsic electronic reconstructions across a series of a samples.[**?**] The gentle molecular beams afforded by this technique eliminates the damage caused to the substrate by the ablated species. We simultaneously grew a series of samples with composition ranging from nearly 25% Al rich to 5% La rich. Surprisingly, we show an exquisite dependence of the interfacial electronic properties on the film stoichiometry with

a sharp onset in conductivity at La/Al≤ 0.97. As the compositional spread was grown simultaneously, we can not only eliminate the effects of varying oxygen background, yet also have controlled environment to probe to compare intrinsic bonding changes and extrinsic defects at the interface. In particular, investigating the microstructure of this series of samples allows us to simultaneously investigate a system which responds to the polar catastrophe by induced electronic changes as well as a seemingly similar samples which lack this electronic reconstruction. We propose a new mechanism to alleviate the polar catastrophe in some of our samples without bonding changes–namely charged cation vacancies which provide a compensating electric field to the diverging electric potential due to the polar catastrophe.

4.2 Experimental

Eight unit cell compositional varying $LaAlO_3$ thin films were grown by reactive molecular beam epitaxy on a Veeco 930 system in 1×10^{-6} Torr of distilled ozone. A single holder was prepared with 16 pieces of $n-type$ TiO_2-terminated $SrTiO_3$ substrates. Four 5 x 5 mm pieces were cut from a single 10 x 10 mm piece of $SrTiO_3$ substrate and the four pieces distributed into the holder such that effects of the starting substrate could be probed. The lanthanum and aluminum sources were calibrated by a quart crystal micrograph and the composition fine tuned using reflection high energy electron diffraction (RHEED) analysis. Composition was measured using Rutherford Backscattering on thick samples grown immediately after the eight unit cell samples. Detailed growth conditions, density functional theory (DFT) and conductivity conditions can be found elsewhere.[**?**]

Energy energy loss spectroscopy was employed to measure the composition and valence of the elements in the system. Tripod polished samples were prepared by gluing pieces of two wafers together, representing the conducting and insulating samples and imaged back-to-back. This permitted analysis of the fine structure of the EELS edges to be performed on samples with identical preparation and imaging conditions. EELS signals from the Ti-$L_{2,3}$ edge (455 eV), O-K-edge (532 eV), La-$M_{4,5}$ edge (832 eV) and Al-K edge (1560 eV) were collected simultaneously. Immediately after, the signal from the La-$M_{4,5}$ edge (832 eV), Al-K edge (1560 eV) and Sr-$L_{2,3}$ edge (1900 eV) were collected due to limitations in the range of the Enfina spectrometer. The simultaneously acquired ADF signal and La EELS signal was used to cross-correlate the signals.

4.3 Results and Discussion

4.3.1 Compositionally varying conductivity

Figure **??** shows a schematic of the experimental setup. Four wafers, labeled 1-4, of etched and annealed TiO_2-terminated $SrTiO_3$ substrate were cut into four pieces, labeled A-D. They were then loaded into a specialized puck for MBE growth. The samples was not rotated during the growth such that the lanthanum and aluminum effusion cells, located at opposite sides of the chamber, created a flux gradient across the sample. The stoichiometric position was then systematically moved by slightly adjusting the shutter times for repeated growths. The conductivity of the samples is indicated by the coloring of the resulting wafer. As shown, the samples closer to the aluminum side of the cham-

ber produced conducting interfaces, regardless of the origin of the wafer piece. Note that both conducting and insulating samples were created from pieces of $SrTiO_3$ substrates etched and annealed simultaneously and provided with the same oxidizing background. While oxygen vacancies induced by the surface treatment or background pressure could enhance the number of mobile carrier concentration, they cannot be solely responsible for the conductivity observed.

Rather, we notice a dependence of the conductivity on a new feature, the cation stoichiometry. Figure **??** shows the interface sheet resistance as a function of the film stoichiometry; there is a sharp change in the resistance at $La/Al = 0.97$. We note that the Al-rich samples are conducting, rather than the La-rich samples, making lanthanum interdiffusion an unlikely cause for the conduction. This data begs a new question as well though: how does the lattice accommodate variations in the aluminum and lanthanum stoichiometry as to create conducting interfaces for Al-rich samples and insulating interfaces for La-rich samples? If the intrinsic polar catastrophe directs the interfacial conductivity, how is it alleviated in the absence of electronic reconstructions for the lanthanum rich samples?

Before probing electron density changes at the interface, we first examine the structural quality of the samples. Figures **??**(a) and (b) show representative HAADF-STEM images and titanium and lanthanum spectroscopic images from two films grown on the same original substrate near the ends of the composition spread. As shown, both films are coherent and epitaxial to the substrate. Dark-field imaging of the samples showed the presence of small quantity of edge dislocations, observed in approximately equal quantities for the conducting and insulating samples.

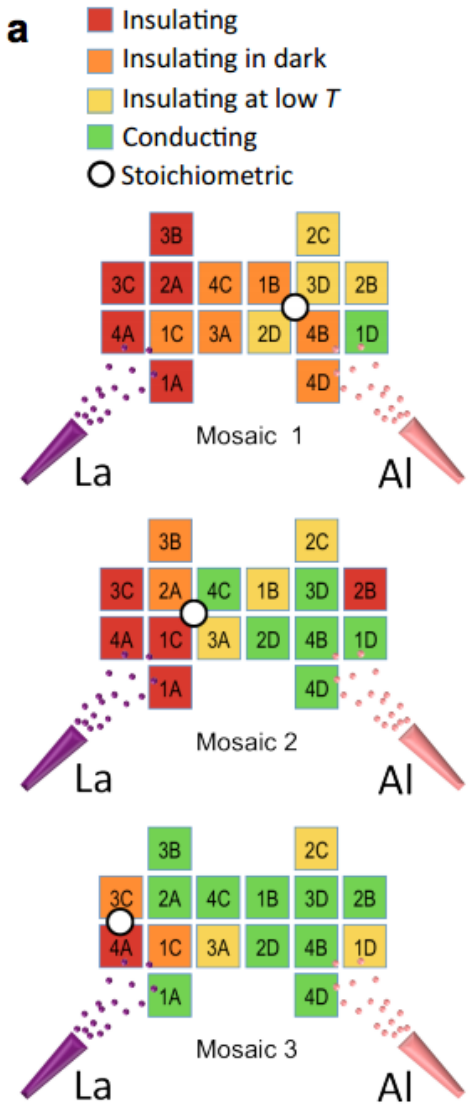

Figure 4.1: The setup of the compositional varying mosaics grown by MBE. Four substrates, labeled 1-4, were cut into pieces A-D and placed in the holder as drawn. The lanthanum and aluminum fluxes were calibrated to near 1:1 stoichiometric ratio yet the samples were not rotated during growth. This yielded aluminum and lanthanum rich samples on the right and left of the mosaic respectively. The electronic properties of the resulting wafers are colored.

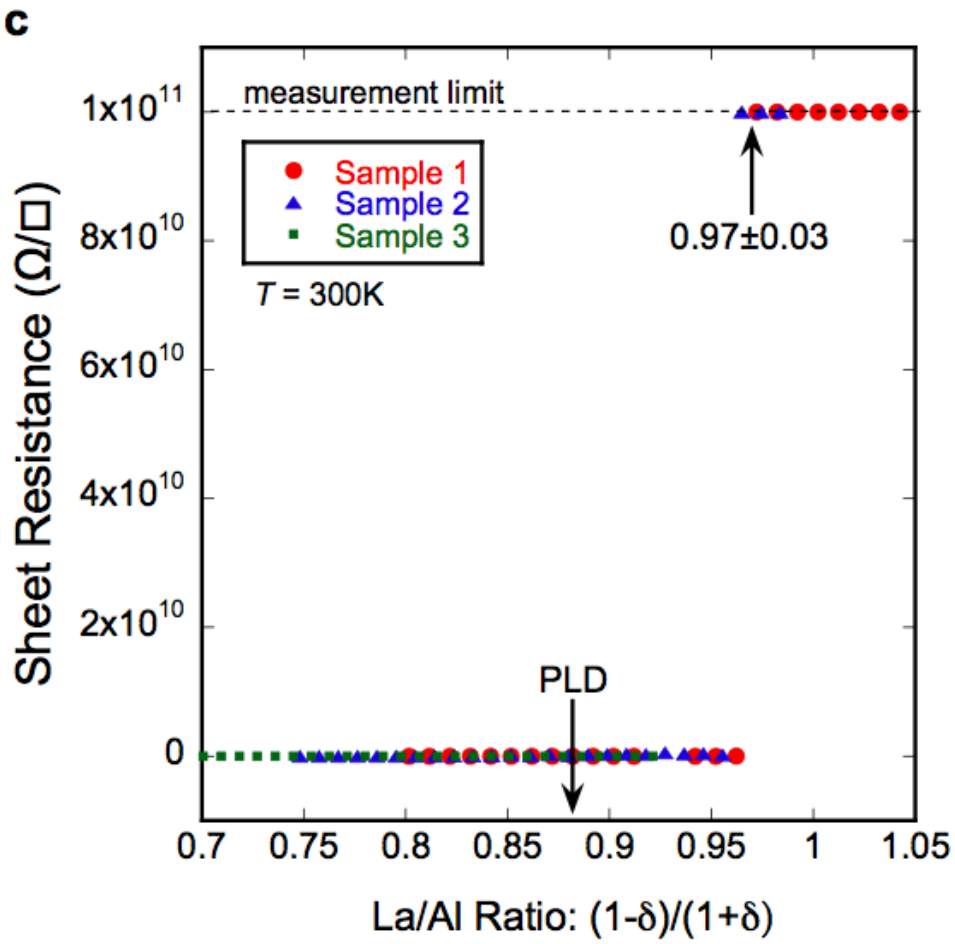

Figure 4.2: The dependence of the interface conductivity on the film stoichiometry. The *La*/*Al* ratio was determined by RBS measurements.

4.3.2 Conducting interfaces through valence changes?

We first probe the electronic reconstructions manifest as valence changes on the titanium sites. As originally proposed, the polar catastrophe at this interface could be alleviated by the addition of half an electron of charge to the titanium sites, an analog to the manganese valence changes quantified in Chapter 5. This would bring the formal valence to $Ti^{+3.5}$ and potentially provide conductivity

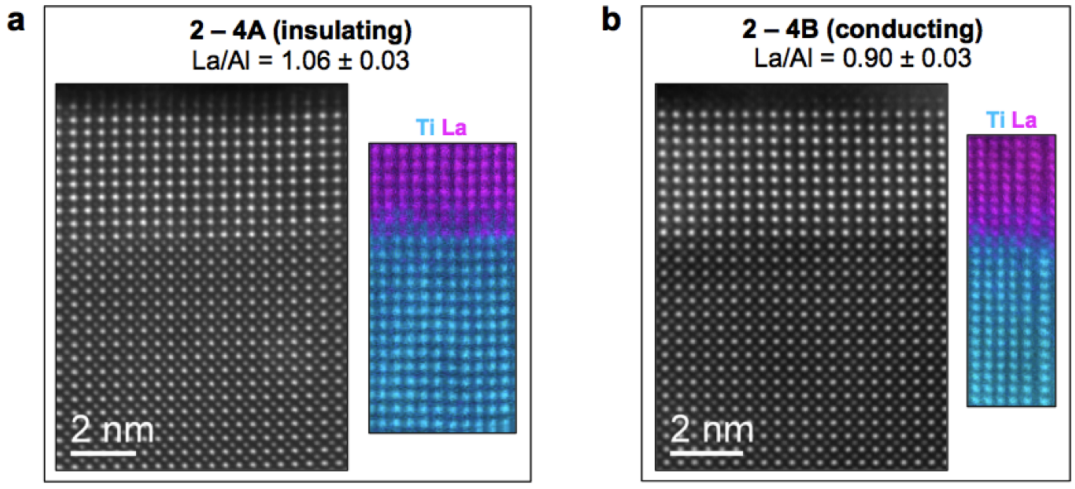

Figure 4.3: HAADF-STEM and EELS characterization of the conducting and insulating interfaces. (a) and (b) show HAADF-STEM images and corresponding titanium and lanthanum EELS maps for two representative conducting and insulating wafers near the end of the composition spread from **??**.

with the itinerant electron. Figure **??** shows the fine structure of the Ti-$L_{2,3}$ EELS edge across the interface for a representative conducting and insulating sample from Figure **??**. As shown in Figure **??**(a), a view of the edge binned parallel to the interface for the conducting sample, a strong change in valence is not apparent. The multivariate curve resolution (MCR) analysis of the edge did produce two distinct components as shown in Figure **??**(b). The interface component tracks a reduction in the crystal field splitting from the titanium edge, possibly caused by local lattice distortions near the interface to $SrTiO_3$. The Ti-$L_{2,3}$ edge concentration profile shown in Figure **??**(c) at the interface shows a significant component that is different from the bulk. A large portion is from crystal field distortions, but we cannot exclude the possibility of a small (< 0.1 eV) contribution from Ti^{+3}, similar to the results for the $La_{0.9}Sr_{0.1}MnO_3$ interface in Chapter 5. This being said, analysis of the fine structure of the titanium edge fails to identify a significant microscopic origin for the large change in interfa-

cial conductivity for the two samples probed. We note that a failure to identify a strong Ti^{+3} component at the interface of the conducting samples is consistent with recent work on samples grown in high oxygen partial pressures as was done here.

We can further confirm this analysis by analyzing the O-*K* edge at the interface. The pre-peak of the oxygen edge is coupled to the number of *d*-holes in the transition metal–titanium and aluminum for this system.[**?**] Thus analysis of the O-*K* edge provides an independent measurement of the interfacial chemistry, as discussed in Chapter 3. Figure **??**(a) shows a concentration profile of the various oxygen components shown in **??**(b). While both samples show the presence of the distinct interfacial component, it is present in the same quantity and concentration for both samples. Moreover, the residual shown in **??**(c) demonstrates that there is not a remaining signal from either sample. Thus it appears that both samples lack half an electron on the titanium sites and further that the fine structure of the oxygen and titanium edges is unable to provide a microscopic understanding of the differences between the samples.

4.3.3 Conducting interfaces through local deviations in cation stoichiometry

While we failed to observe changes in the titanium bonding at the interfaces, the EELS spectroscopic maps provide clues regarding the differing electronic properties by measuring how the samples accommodated the local deviations in stoichiometry at the atomistic scale. An EELS map was recorded collecting the titanium, aluminum and lanthanum edges simultaneously to compute the

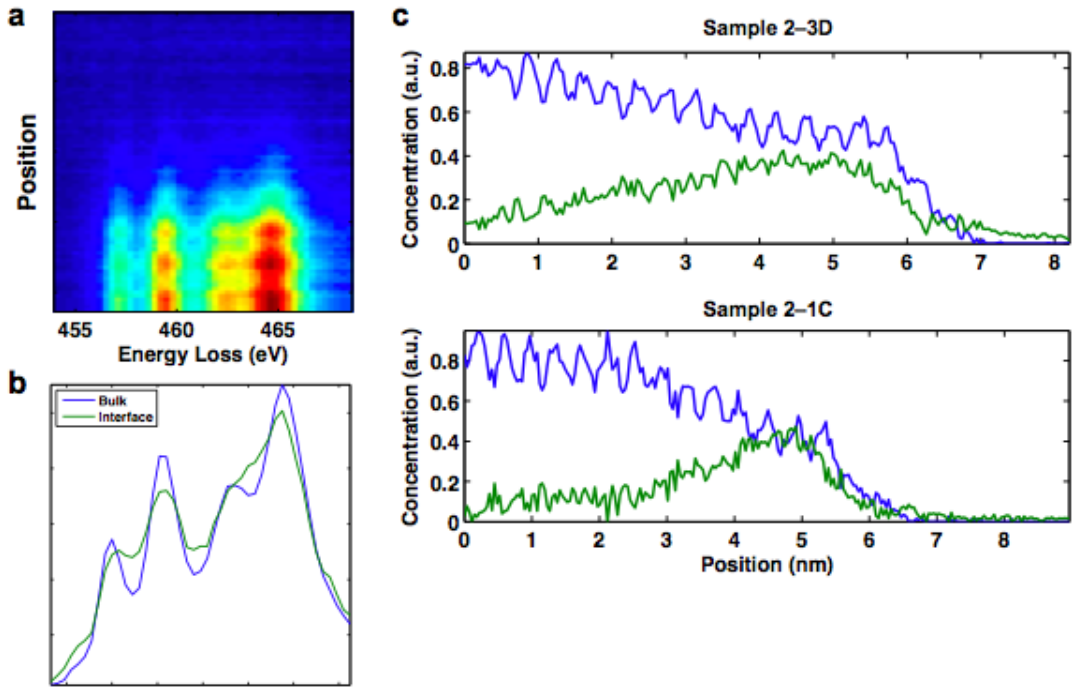

Figure 4.4: EELS fine structure of the Ti-$L_{2,3}$ edge of the $LaAlO_3/SrTiO_3$ interface for a conducting (2-3D) and an insulating (2-1C)sample. (a) A two-dimensional profile of the Ti-$L_{2,}3$ edge across the $LaAlO_3/SrTiO_3$ interface for the conducting interface 2-3D. The interface is interdiffused, although no shift to lower onset energy, indicative of a reduction in the titanium valence, is observed. (b) Spectra extracted from the multivariate curve resolution analysis of the Ti-$L_{2,3}$ edge. The interface component tracks a reduction in the crystal field splitting from the titanium edge, possibly caused by local lattice distortions near the interface to $SrTiO_3$. The Ti-$L_{2,3}$ edge spectrum at the interface shows a significant component that is different from the bulk. A large portion is from crystal field distortions, but we cannot exclude the possibility of a small ($\leq$0.1 eV) contribution from Ti^{+3}. The spectra and the lack of a dominant Ti^{+3} component look similar to those reported for other high oxygen pressure growths of $LaAlO_3/SrTiO_3$. (c) Result of the fit of the spectra in (b) to the full data sets for conducting sample (2-3D) and insulating sample (2-1C). Deviations in the quantity of the interface component observed could be due to slight differences in lanthanum interdiffusion for the two samples.

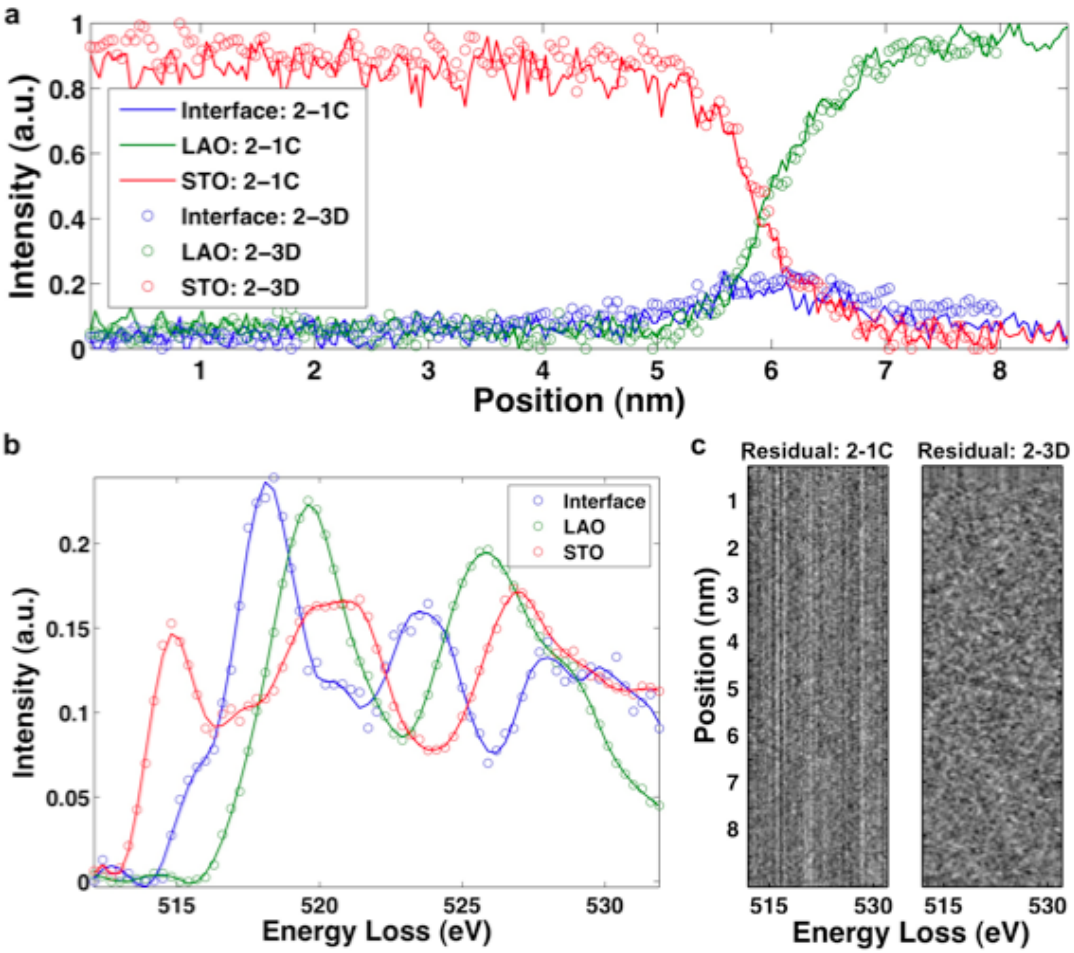

Figure 4.5: EELS fine structure of the O-*K* edge of the $LaAlO_3/SrTiO_3$ interface for a conducting (2-3D) and an insulating (2-1C) sample. (a) The concentration profile of the data fit to a $LaAlO_3$ and $SrTiO_3$ reference spectra as well as a distinct interface component extracted from the data by multivariate statistical analysis. (b) Spectra used in the fit. Both samples show the presence of an interfacial O-*K* edge component, distinct from $LaAlO_3$ and $SrTiO_3$. This component appears, however, for both samples with the same concentration and spatial extent. (c) The residual from the fit showing the absence of any remaining structure. The streaks for 2-1C result from a slightly different fixed pattern noise in the spectra due to a different acquisition time.

total concentration of atoms residing on the *B*-site sub-lattice. Likewise, a subsequent simultaneous acquisition the lanthanum, strontium and aluminum edges provides the total concentration of atoms on the *A*-site. In the conducting, Al-rich samples, aluminum and titanium were found to completely occupy the B-site sub-lattice, as shown in Fig. **??**(a). In contrast, the insulating, La-rich samples show a local accumulation of cation vacancies on the B-site sub-lattice at the interface (Fig. **??**(b)). Figure **??**(a,b) also shows that neither interface shows a corresponding local dip in the cation concentration on the A-site sub-lattice. The experimentally observed cation vacancies in the B-site sub-lattice at the interface of La-rich samples (Fig. **??**(b)) are significant for understanding the charge balance at the interface. From these can detect cation vacancies; as the cations are ionized–La^{+3}, Sr^{+2}, Al^{+3} and Ti^{+4}–cation vacancies would change the local electrostatic picture in the absence of valence changes as shown in Chapter 2.

The electrostatic picture resulting from these cation vacancies can be explicitly computed as shown in Fig. **??**. For the conducting, Al-rich samples, DFT calculations demonstrated that a stable defect configuration is for the excess aluminum to reside on the lanthanum side, below the detection limit of EELS, as shown in Fig. **??**(a). Given that both cations have the same nominal +3 oxidation state, this does not change the charge dynamics from a stoichiometric $LaAlO_3$ film. The diverging potential in **??**(b) could thus be alleviated by an electronic reconstruction, bringing charge to the interfacial titanium sites as shown in **??**(c). In contrast, DFT calculations predicted that vacancy Al_2O_3 planes are formed formed on the La-rich side of the composition spread as shown in **??**(d). These vacancy planes provide a conduit for cation vacancies to develop during growth as a response to the polar catastrophe. As shown in

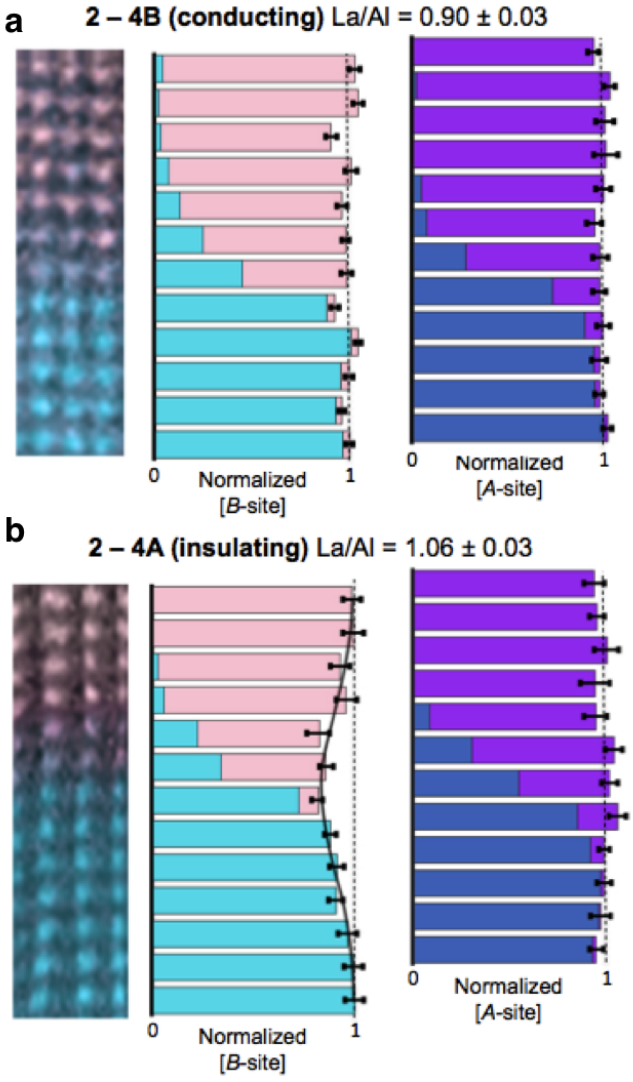

Figure 4.6: EELS concentration mapping of the interface. A representative STEM-EELS spectroscopic image of aluminum (pink) and titanium (turquoise) from the conducting wafer 24B shown in Fig. **??**(b). The normalized total concentration of titanium and aluminum occupying the B-site sublattice does not show any systematic variation from layer to layer along the [001] direction. Similarly, the total occupancy of lanthanum and strontium at the A-site shows no variation along the [001] direction. A representative STEM-EELS spectroscopic image of aluminum (pink) and titanium (turquoise) from the insulating wafer 24A shown in Fig. **??**(a). In contrast to the map shown in b, there is a dip in the normalized B-site occupancy at the interface, indicating a local accumulation of B-site vacancies, whereas the A-site occupancy shows no detectable variation along the [001] direction.

??(e), consistent with the EELS data, these charged aluminum vacancies screen the polarization catastrophe in the absence of other electronic changes.

It is important to note that this analysis required a normalization of the total EELS cross-section for each element. For the signals from Sr and Ti, the normalization could easily by achieved by assuming the $SrTiO_3$ is stoichiometric and normalizing the signals in the substrate away from the interface. In contrast, the $LaAlO_3$ film was only eight unit cells on average and it was not possible to normalize the signals sufficiently far from the interface. While the signals were normalized for the top few unit cells, we note that an error in the normalization could not create or remove a cation vacancy at the interface. Figure **??** shows simulations where the concentration of each constituent is modeled with an error function to approximate the diffusion profiles at the interface. Figure **??**(a) and Fig. **??**(b) show a vacancy free interface with and without a normalization error for one cation. Importantly, neither show a local dip in the total concentration below that experienced at either side. In contrast, Fig. **??**(c) and Fig. **??**(d) repeat the calculation, with vacancies added at the interface. Despite the normalization conditions, there is dip in the total concentration below that experienced at either side of the sample. Thus the calculations presented above are robust even to small errors in the EELS cross-section.

4.3.4 Conducting interfaces through interdiffusion

Interdiffusion has been proposed as the origin of the conductivity at the $LaAlO3_3/SrTiO_3$ interface as lanthanum doped $SrTiO_3$ is conducting (although it would be difficult to explain the novel magnetic phases which arise at this in-

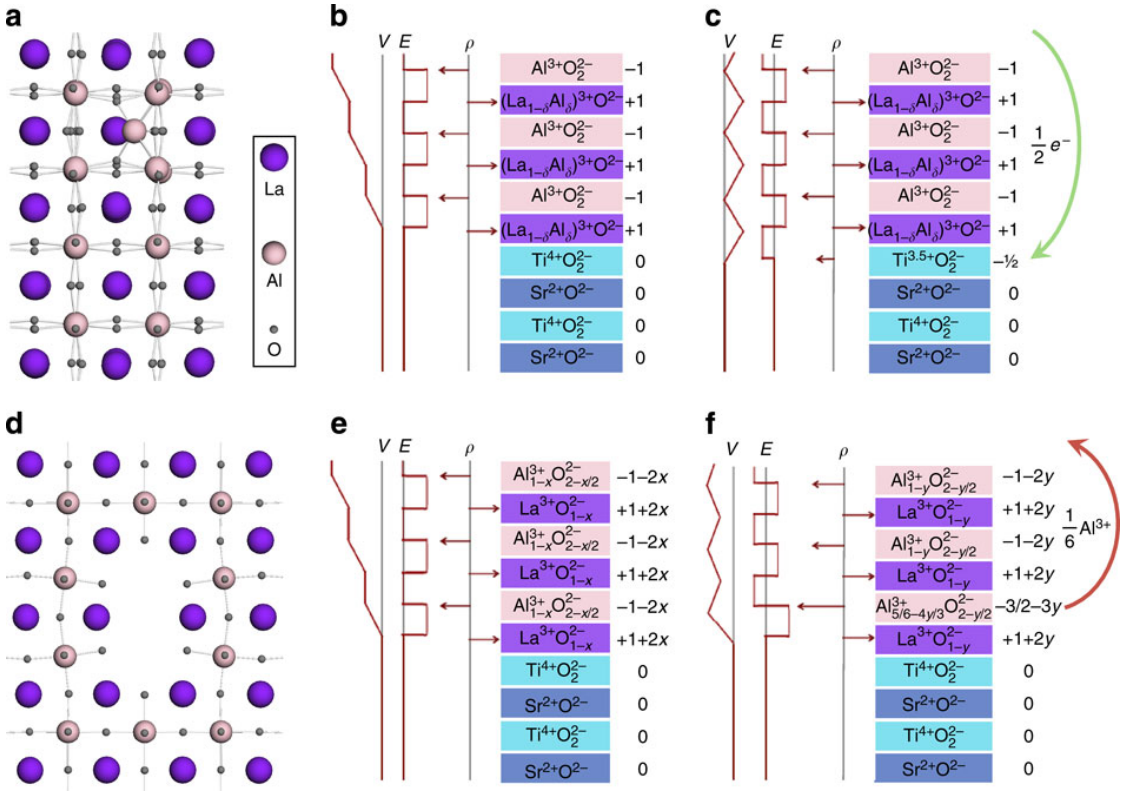

Figure 4.7: (a) In Al-rich films, aluminum substitutes for lanthanum and shifts off the cuboctahedron centre. The lowest-energy structure is shown as viewed along the [100] direction. (b) The alternating charges (ρ) of the (001) planes in Al-rich $La_{(1?\delta)}Al_{(1+\delta)}O_3$ and the charge neutral (001) planes in $SrTiO_3$ generates a positive average electric field (E) and a diverging potential (V). The substitution of Al^{+3} for La^{+3} does not modify the alternating polarity from that of a stoichiometric $LaAlO_3$ film. c. In thick Al-rich films, the system reconstructs electronically, transferring half an electron per unit cell from the surface to the interface. (d) In La-rich films, Al_2O_3-vacancy complexes form, which are periodic in the [001] direction. The smallest Al_2O_3-vacancy complex is shown as viewed along the [001] direction. (e) The extended Al_2O_3-vacancy complexes in the unreconstructed La-rich films also remove oxygen from the nominal $(LaO)^+$ layers. The aluminum deficiency is given by $x = 2\delta/(1\delta)$. A diverging potential results in the unreconstructed films from the alternately charged (001) planes of $La_{(1+\delta)}$ $Al_{(1-\delta)}O_3$. (f) In thick La-rich films, extra aluminum vacancies can move to the interface through the Al_2O_3-vacancy complexes to screen the diverging potential. The aluminum deficiency y now depends on the stoichiometry (δ) and the film thickness. Figure and caption from [**?**]

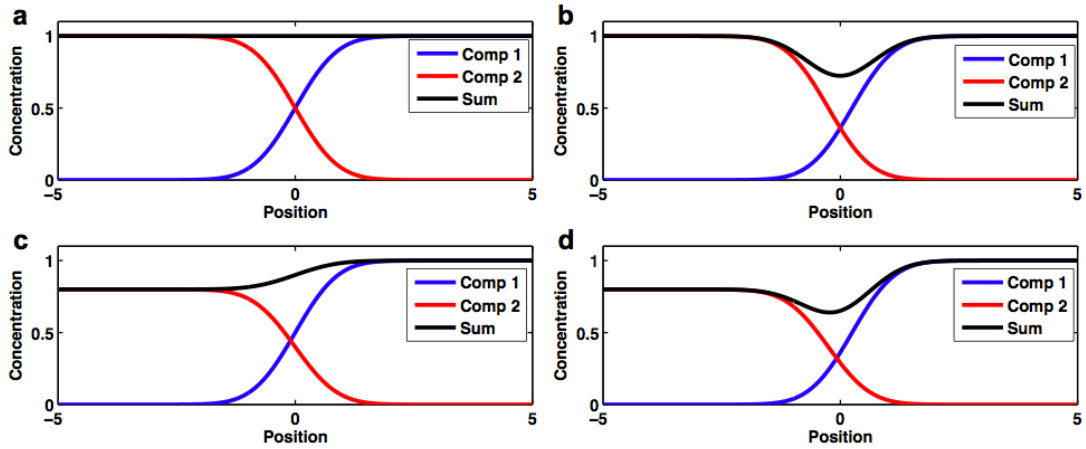

Figure 4.8: Simulation to confirm normalization of cation concentration. (a) A simulation of a vacancy free interface with interdiffusion (error function line shape). The total sum of the two components is unity throughout the interface. (b) Simulation of two normalized components, however with a 25% reduction in the total atomic concentration at the interface. A clear dip in the total concentration is observed, similar to Fig. **??**(b). (c) Simulation of two components, one of which has 80% occupancy but free of additional vacancies at the interface. There is no local dip in the total concentration at the interface below the mean values on either side. (d) Simulation of two components, one of which has 80% occupancy and additional vacancies added at the interface. Once again a local drop in the total atomic profile is seen at the interface.

terface with interdiffusion given that $LaTiO_3$ is non-magnetic). Although the dependence on the interface conductivity on the cation stoichiometry was demonstrated above, this series of samples provides a model system to investigate the proposed dependence of conductivity on the degree of lanthanum interdiffusion. Figures **??**(a) and (b) show representative HAADF-STEM images and titanium and lanthanum spectroscopic images from two films grown on the same original substrate near the ends of the composition spread. As shown, both films are coherent and epitaxial to the substrate. A small amount of lanthanum interdiffusion is observed, however, as shown in Fig. **??**(c), there is no correlation between the diffusion and conductivity. Namely, the samples are arranged

in Fig. **??**(c) roughly in order of increasing interdiffusion. Both conducting and insulating samples are observed at both ends of the spread, with no apparent correlation. Thus the charge carriers observed in Fig. **??** cannot be attributed to this extrinsic defect.

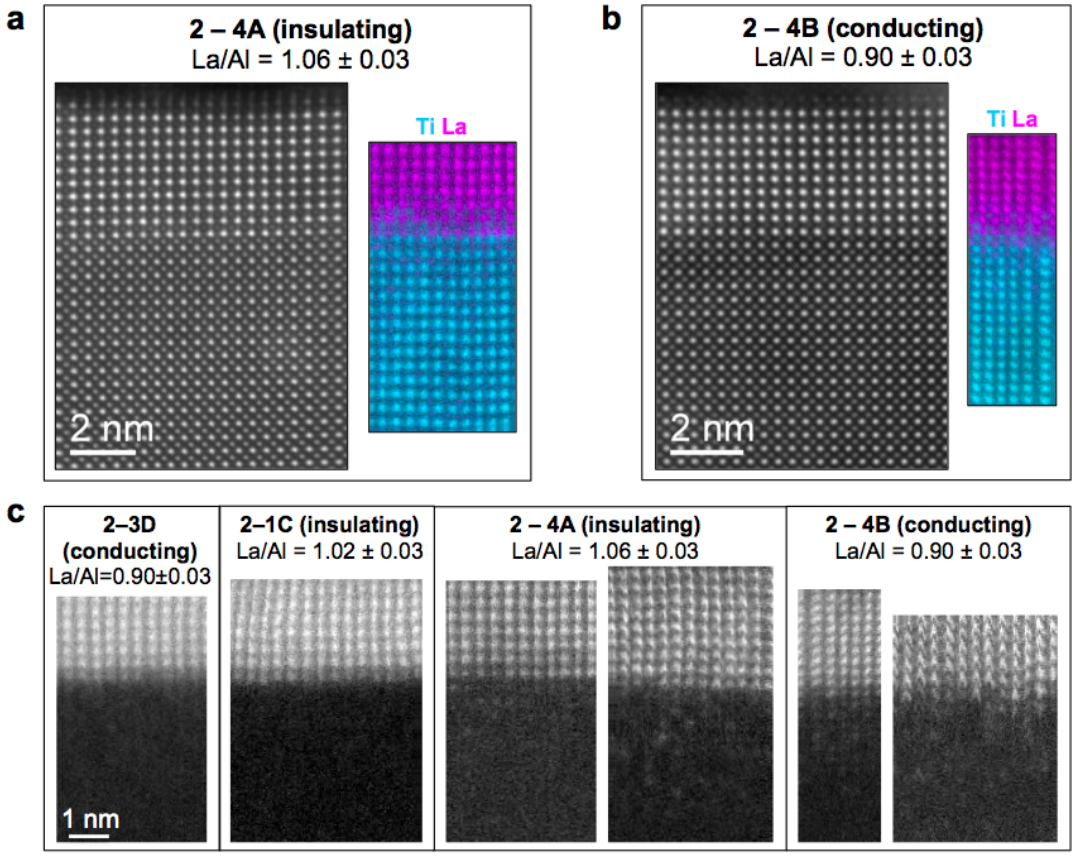

Figure 4.9: HAADF-STEM and EELS characterization of the conducting and insulating interfaces. (a) and (b) show HAADF-STEM images and corresponding titanium and lanthanum EELS maps for two representative conducting and insulating wafers near the end of the composition spread from **??**. A series of lanthanum EELS maps were collected in (c) through the composition spread, on multiple wafers. Two separate TEM samples were prepared from 2-4A and 2-4B to look for variations within a single wafer. While lanthanum interdiffusion is observed in each case, the conductivity does not track with the interdiffusion as both insulating and conducting samples show high and low amounts of interdiffusion

4.4 Conclusions

In this section, we investigated a series of $LaAlO_3/SrTiO_3$ interfaces with varying $LaAlO_3$ cation stoichiometry. This interface has been the subject of intense interest and debate of late due to the questions regarding the interplay of defects and intrinsic electronic reconstructions in understanding the interfacial conductivity. Here, we propose a new model for understanding these polar interfaces where the polar catastrophe was alleviated with a local dip in total cation concentration residing on the *B*-site sublattice. This total dip could be probed even the presence of cation interdiffusion using STEM-EELS to measure the concentration of each constituent cation simultaneously. This interplay between the intrinsic and extrinsic causes for interface chemistry will be investigated further through an exploration of the related $La_{1-x}Sr_xMnO_3/SrTiO_3$ interfaces.

4.5 Acknowledgements

Most of the figures and analysis for this chapter appears in "$LaAlO_3$ stoichiometry is key to electron liquid formation at $LaAlO_3/SrTiO_3$ interfaces" authored by M. P. Warusawithana, C. Richter, J. A. Mundy, P. Roy, J. Ludwig, S. Paetel, T. Heeg, A. A. Pawlicki, L. F. Kourkoutis, M. Zheng, M. Lee, B. Mulcahy, W. Zander, Y. Zhu, J. Schubert, J. N. Eckstein, D. A. Muller, C. Stephen Hellberg, J. Mannhart and D. G. Schlom. (Nature Communications 4, Article number: 2351, 2013). I performed the STEM and EELS analysis of these samples in consultation with Lena F. Kourkoutis and David Muller. The DFT calculations and preparation of the corresponding figures presented in this chapter were done by C. Stephen Hellberg. The samples were grown by Maitri Warusawithana

and Darrell Schlom. I would like to particularly acknowledge extensive conversations with Stephen Hellberg regarding the interpretation of the STEM-EELS data.

CHAPTER 5

VISUALIZING THE EVOLUTION FROM INTERFACIAL CHARGE COMPENSATION TO METALLIC SCREENING ACROSS THE MANGANITE METAL-TO-INSULATOR TRANSITION

5.1 Introduction

Manganites, such as $La_{1-x}Sr_xMnO_3$, exhibit many of the exotic bulk phases seen in the complex oxides, with paramagnetic insulating ($x \leq 0.2$) and ferromagnetic metallic ground states ($x > 0.2$) at room temperature and additional charge and orbital ordered phases accessible at low temperatures.[**?**, **?**] Next generation spin tunnel junctions could be formed by exploiting the room temperature ferromagnetism in ultrathin layers of $La_{0.67}Sr_{0.33}MnO_3$.[**?**] Observed interfacial dead layers have, however, limited the scaling of potential devices.[**?**] While explicit attempts[**?**, **?**] to offset the interface dipole[**?**, **?**] and to eliminate extrinsic defects[**?**] have reduced the observed dead layer thickness, direct mapping of these intrinsic electronic and magnetic reconstructions at the interface can be obscured by variations in growth techniques leading to competing defects.

Studying these electronic reconstructions at manganite interfaces provides an ideal platform to probe the interface across the metal-to-insulator transition. The large changes in electronic properties are induced by continuous hole-doping while maintaining the same crystal topology via the Mn-O backbone. In this chapter, we provide a systematic study of a series of $La_{1-x}Sr_xMnO_3$/Nb:$SrTiO_3$ (LSMO/STO) interfaces from $x = 0$ to $x = 0.5$, prepared under identical growth conditions, to disentangle the extrinsic and intrinsic effects at the interface through a range of states on the phase diagram.

By measuring the concentration and valence of all cations in the system using electron energy loss spectroscopy (EELS), we explicitly quantify the electronic charge transfer apparent as a cation valence change. We show a quantitative agreement between the polar catastrophe model and the total electron transfer to the manganese sites of the insulating LSMO films, yet a considerable drop in the total charge transfer and spatial extent with the onset of screening in the metallic $La_{0.7}Sr_{0.3}MnO_3$.

5.2 Experimental

We investigate thin films of $La_{1-x}Sr_xMnO_3$ with $x = 0, 0.1, 0.2, 0.3$ and 0.5 grown by pulsed laser deposition on TiO_2-terminated 0.01 w% Nb-doped $SrTiO_3$ [100] substrates. Cross-sectional TEM specimens were investigated on the 5^{th}-order aberration corrected 100 keV Nion UltraSTEM equipped with an Enfina spectrometer. The microscope conditions were optimized for EELS spectroscopic imaging with a probe size of 1 Å, EELS energy resolution of 0.6 eV and a dispersion of 0.3 eV/channel. Elemental concentrations and bonding information were extracted from the simultaneous acquisition of the Ti-$L_{2,3}$, Mn$L_{2,3}$, O-K and La-$M_{4,5}$ edges. To measure the concentration of all the cations in the system, the Nion UltraSTEM, now equipped with a Quefina Dual-EELS spectrometer, was used to measure the Sr-$L_{2,3}$ edge simultaneously with the Ti, Mn and La edges. For all samples, the Ti signal from the substrate and the La edges were used to accurately calibrate the energy shift and dispersion between the samples.

5.3 Results

5.3.1 Cation Interdiffusion

A high angle annular dark field (HAADF) STEM image of the $La_{0.9}Sr_{0.1}MnO_3/SrTiO_3$ interface is shown in Fig. 1a; the interface is coherent and free of dislocations. From the corresponding La, Mn, and Ti EELS elemental maps in Fig. **??**b-d respectively and the combined map in Fig. **??**e, we note an asymmetry as the *B*-site or Mn/Ti sub-lattice is nearly atomically abrupt with inter-diffusion observed only over a single monolayer near the interface. In contrast, the *A*-site La shows considerable inter-diffusion over approximately four monolayers near the interface. The polar discontinuity shown in **??**f and in Chapter 2 cannot be alleviated by *A*-site interdiffusion in and of itself, however, asymmetric diffusion between the *A*-site and *B*-site cations could reduce (or enhance) the potential offset at the interface as shown in Chapter 2. Ironically though, preferential diffusion between the *A*-site cations for the $La_{0.9}Sr_{0.1}O/TiO_2$ (the so-called *n*-type) interface without changes in the *B*-site cation valence serves to increase the potential build-up rather than decrease it.

Cation vacancies, on the other hand, could provide positively charged defects to reduce the potential build-up in the film. The total concentration of the cations across the interface, Fig. **??** and Fig. **??**, was calculated using the elemental profile maps acquired simultaneously for Ti, Mn, La and Sr. Following a background subtraction and integration over the near edge fine structure, each signal was normalized far away from the interface, e.g. Ti was assumed to fully occupy the B-site sublattice in $SrTiO_3$ 10 nm away from the film-substrate interface. The total *A*-site and *B*-site cation concentrations were then summed

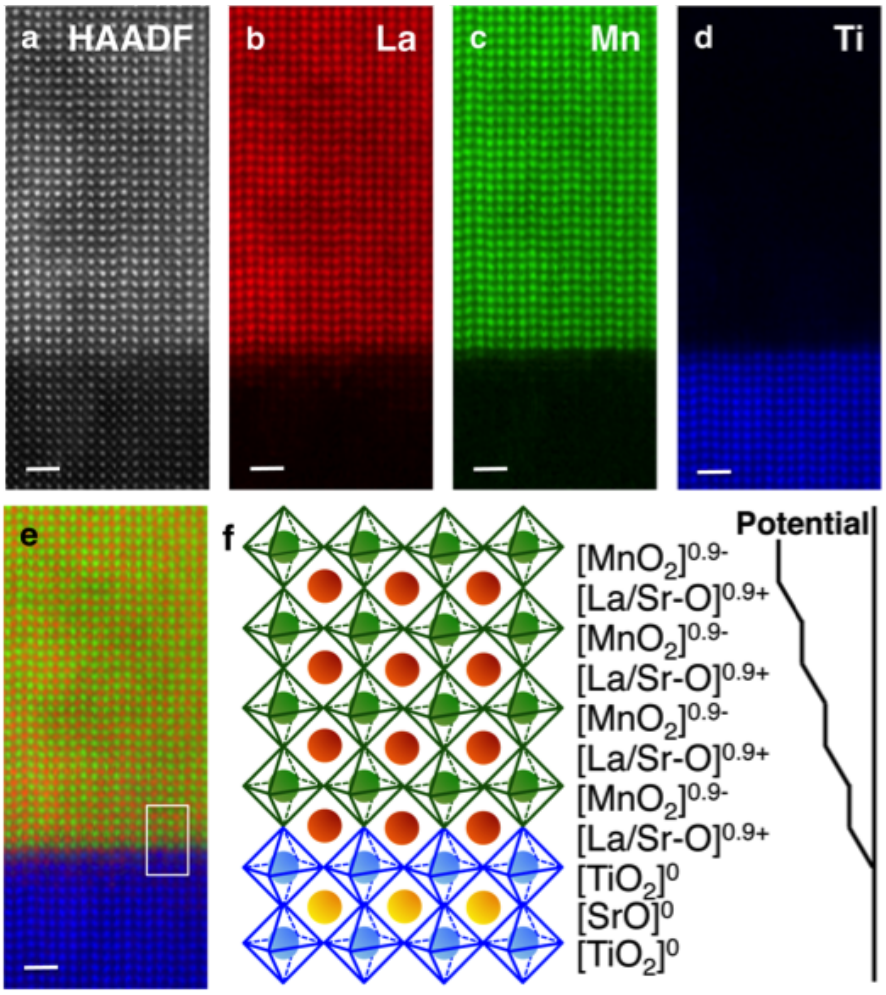

Figure 5.1: EELS Spectroscopic mapping of the $La_{0.9}Sr_{0.1}MnO_3/SrTiO_3$ interface. The HAADF-STEM image and the the elemental concentrations of La, Mn and Ti are shown in (a-d) respectively. A combined map with Ti in blue, Mn in green and La in red is shown in (e). A cartoon of an atomically abrupt $La_{0.9}Sr_{0.1}MnO_3/SrTiO_3$ interface with the diverging electric potential due to the polar film is shown in (f). Scale bars are 1 nm.

through the interface to look for local variations in the total cation concentration as were shown for some $LaAlO_3/SrTiO_3$ interfaces[**?**, **?**] in Chapter 4. Despite the observed asymmetric diffusion between the *A*- and *B*-site cations, the total cation concentration across the interface does not deviate by more than 3 ± 2 % from the expected occupancy of a cation vacancy-free interface, even for the most diffuse interface as shown in Fig. **??** and Fig. **??** . Extrinsic defect driven mechanisms, therefore, do not play a dominant role in our films.

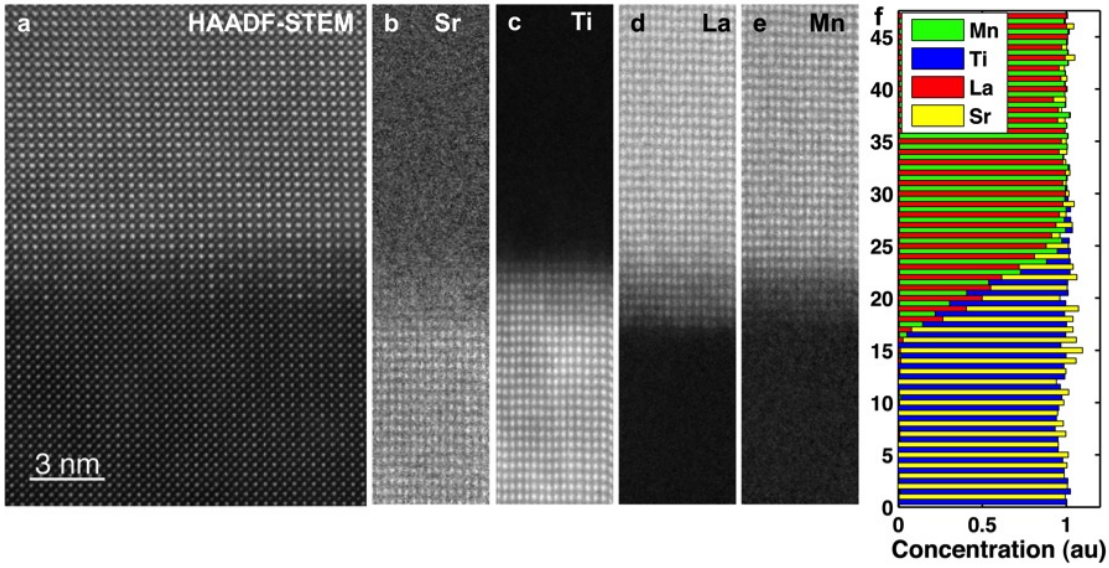

Figure 5.2: Spectroscopic imaging of all the cations at the $LaMnO_3/SrTiO_3$. The HAADF-STEM image in (a) shows that the interface is coherent and free of dislocations. The concentration maps for Sr, Ti, La and Mn are shown in b-e, respectively. The binned concentrations for all cations are shown in (f).

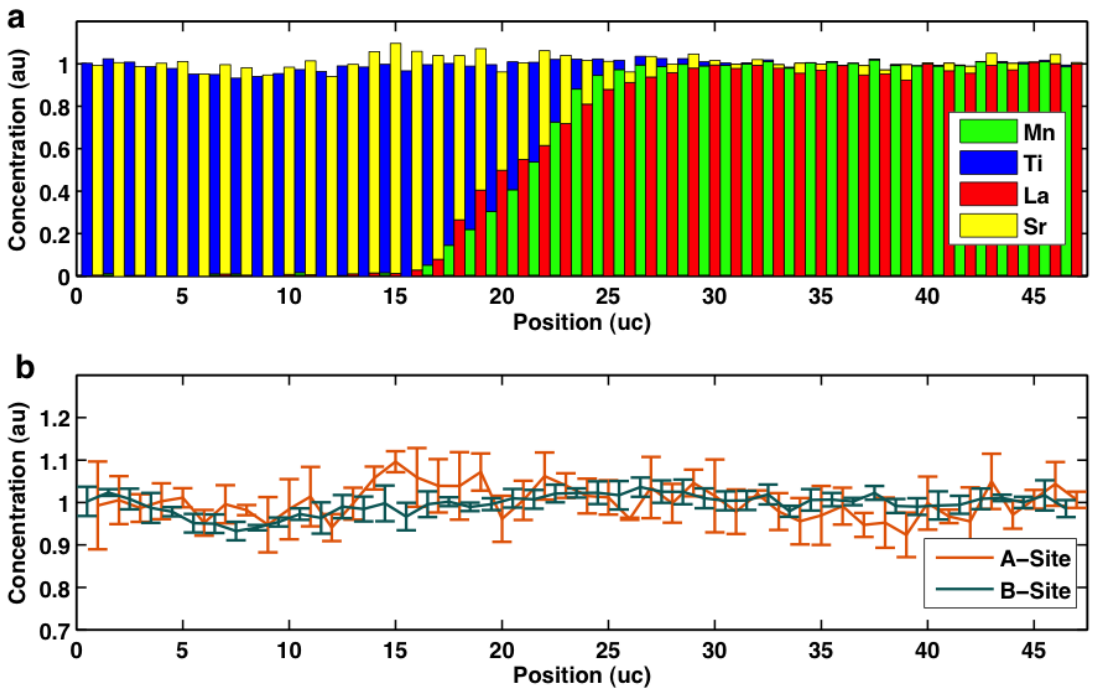

Figure 5.3: Determining the total cation concentration across the interface for $LaMnO_3/SrTiO_3$. (a) The profile of all the concentrations, reproduced from Fig. **??**. (b) The total concentration on the A-site (La + Sr) and the B-site (Mn + Ti). Error bars are the standard error of the mean. From these plots, the total variation in the interfacial composition was determined to be less than 3% from the expected stoichiometry.

5.3.2 Mapping the Valence Changes at the $La_{0.9}Sr_{0.1}MnO_3/SrTiO_3$ interface

As the polar discontinuity was not alleviated by cation vacancies, we now turn to charge modulation. The Mn $L_{2,3}$-edge binned parallel to the interface is shown in Fig. **??**a; near the interface the edge onset shifts to lower energy, indicative of a reduced manganese valence state. From this edge, two distinct components were extracted with multivariate curve resolutiona bulk $Mn^{+3.1}$ spectra and a lower valence stateas shown in Fig. **??**b. A non-negative

non-linear least squares fit to the full Mn $L_{2,3}$-edge reveals the presence of a significant fraction of a lower valence state at the interface as shown in the binned line profile in Fig. **??**c and full 2-D fit in Fig. **??**d. The residual from the fit is presented in Fig. **??** and Fig. **??**.

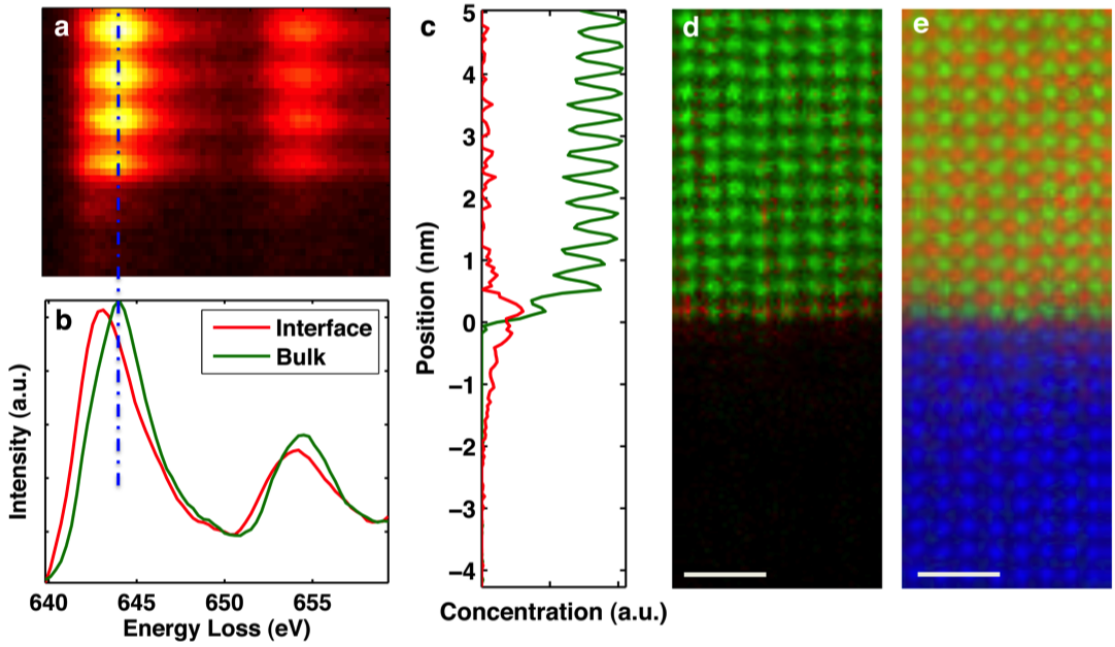

Figure 5.4: Mn valence changes at the $La_{0.9}Sr_{0.1}MnO_3/SrTiO_3$ interface. The Mn $L_{2,3}$-edge binned across the interface is shown in (a) from which two distinct components can be extracted as shown in (b). The two components are fit to the Mn spectra across the spectroscopic image as shown binned in (c) and in the full 2-D map in (d). The concentration map plotting Ti, Mn and La in blue, green and red, respectively, is shown in (e). Scale bars are 1 nm.

Titanium is a multivalent cation and charge could potentially reside on the titanium site as well. A similar analysis of titanium did not yield a change in the valence below the nominal Ti^{+4} of bulk $SrTiO_3$. Figure **??** shows the evolution of the Ti-$L_{2,3}$-edge across the $La_{0.9}Sr_{0.1}MnO_3/SrTiO_3$ interface as a complement to Fig. **??**. Two distinct components were extracted from the binned Ti-$L_{2,3}$ edge, (a), as shown in (b). While the interface component is spatially localized at

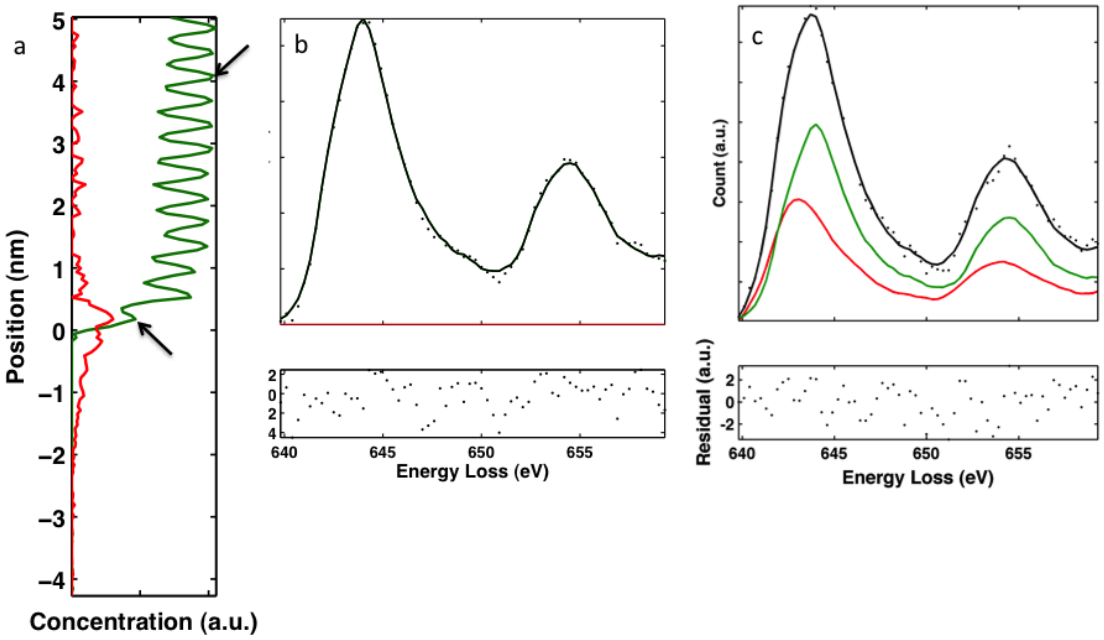

Figure 5.5: Fitting of the Mn-$L_{2,3}$ interface across the interface. (a) Mapping of the EELS fine structure of across the interface, reproduced from Fig. **??**(c). (b) For the location marked with an arrow in (a) in the bulk of the film, the EELS fine structure can be reproduced completely with the bulk component in Fig. **??**(b) and no contribution from the interface component. The raw data is plotted with black dots and the fit with a black line. The residual was computed the difference between the raw data and computed fit. As the residual plot below the spectra shows, there is no remaining fine structure that is not captured. (c) The same analysis is repeated for a lattice site near the interface marked with an arrow in (a). Here, there are significant contributions from both the interface and the bulk components from Fig. **??**(b). The addition of the two components to calculated spectra is shown with the black line. As indicated by the residual, the fine structure is captured by a linear combination of these two components.

the interface, it does not show the distinct reduction in onset energy indicative of a Ti^{+3} bonding state. Rather, we observe a reduction in the e_g-t_{2g} splitting which can be understood as a reduction in the coherent crystal field splitting at the interdiffuse interface.[**?**] This indicates that the majority of the electronic transfer to the interface resides on the manganese sites in our samples rather than on the titanium sites as was reported for thin films.[**?**, **?**]

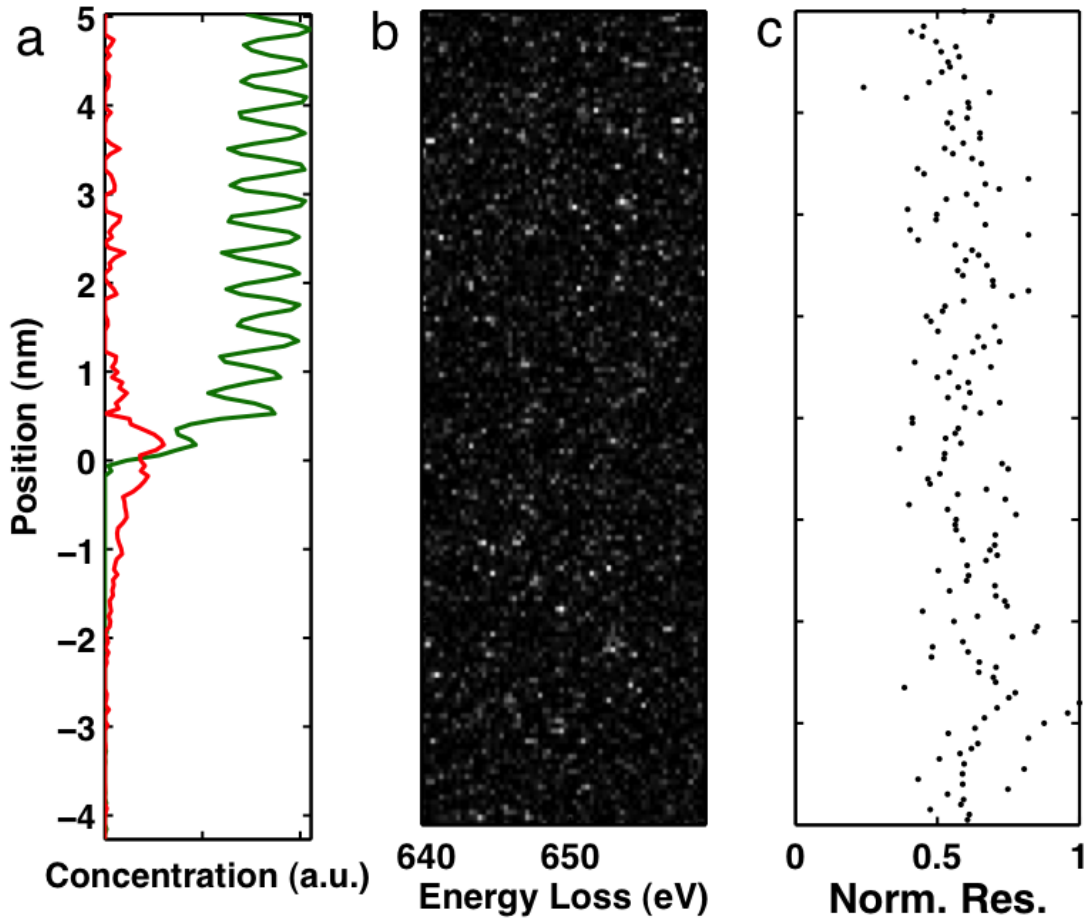

Figure 5.6: Goodness of the fits shown in Fig. 2. (a) The concentration map of the two EELS fine structure components reproduced from Fig. **??**(c). The squared residual is shown in (b). A sum of the residual across the energy range is shown in (c). As shown, the fit matches the experimental data to within the noise through the spatial and energy range probed.

Finally, we note that the interface manganese valence changes cannot be attributed to interdiffusion. Note that diffusion of a manganese atom onto a titanium site should drive the manganese valence up from the nominal bulk valence of +3.1 towards the titanium valence of +4. Moreover, we note that in Fig. **??**, intermixing on the *A*-site was observed which would place Sr atoms on the La sites in the LSMO films. This once again would serve to increase the inter-

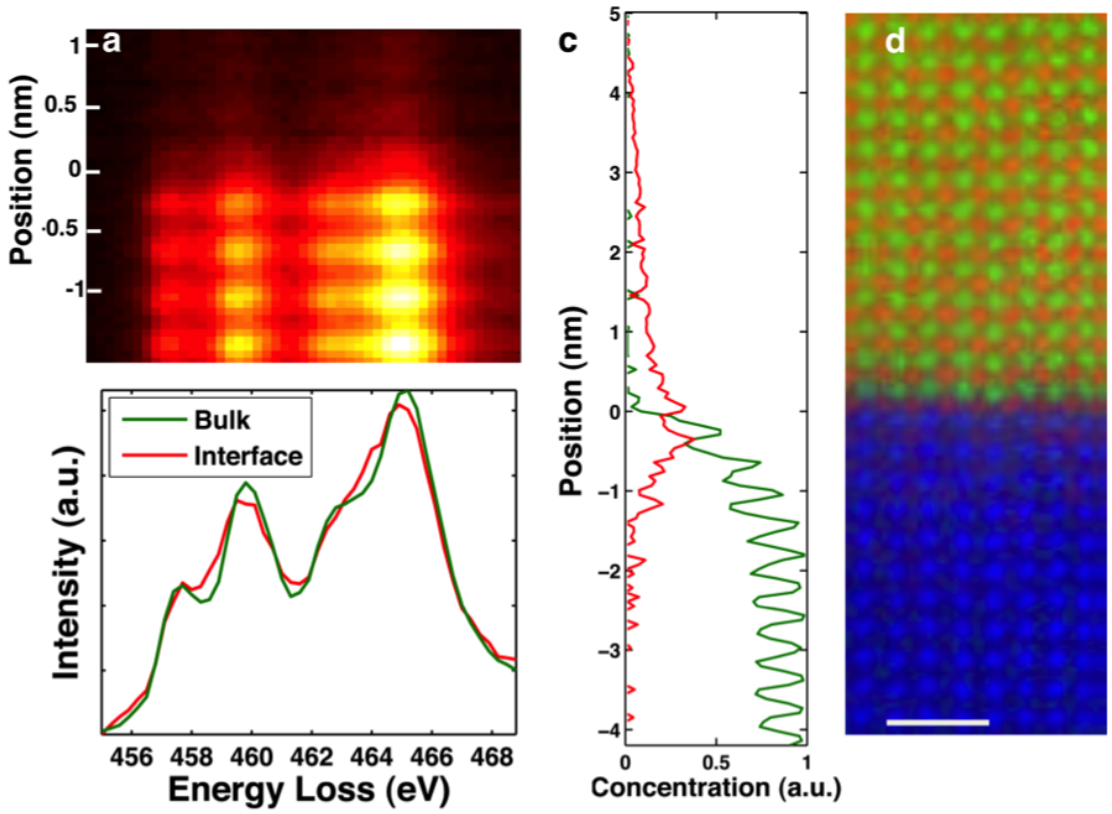

Figure 5.7: Ti fine structure changes at the $La_{0.9}Sr_{0.1}MnO_3/SrTiO_3$ interface. The Ti $L_{2,3}$-edge binned across the interface is shown in (a) from which two distinct components can be extracted as shown in (b). The two components are fit to the Ti spectra across the spectroscopic image as shown binned in (c). The concentration map plotting Ti, Mn and La in blue, green and red, respectively, is shown in (e). Scale bars are 1 nm.

facial manganese valence, in contrast to the experimentally observed decrease. Experimentally, however, we show that the interfacial manganese valence instead decreases. Thus, the changes in manganese valence observed cannot be interpreted by interdiffusion driven valence changes.

5.3.3 Mapping valence changes across the metal-insulator transition

To probe how the charge transfer varies across the metal-to-insulator transition, this analysis was extended to the full series of LSMO films from $x = 0$ to $x = 0.5$. The 2-D concentration maps shown in Fig. **??**a indicate that the considerable *A*-site intermixing at the $LaMnO_3/SrTiO_3$ interface did not persist for the strontium doped films. To characterize the manganese valence at the interface, we performed a non-negative non-linear least squares fit of the manganese signal across the interface to reference spectra for Mn^{+3}, $Mn^{+3.5}$ and Mn^{+2}, Fig. **??**b, obtained from the bulk $LaMnO_3$, $La_{0.5}Sr_{0.5}MnO_3$ films and the literature[**?**] respectively. We note that while the $Mn^{+3.5}$ spectra represents a superposition of Mn^{+3} and Mn^{+4} spectra, the mathematical decomposition of the full data into this spectral basis is equivalent to that which could be achieved using a basis including the Mn^{+4} spectra. The residuals from the fits are presented in Fig. **??**, demonstrating the reliability of the fits across the series of samples with the basis spectra chosen. A statistically significant concentration of Mn^{+2} is observed at the interface for $x < 0.3$. Furthermore, the line profiles, Fig. **??**c, show a significant change in manganese valence near the interface, even in the absence of the Mn^{+2} component for the $x = 0.3$ interface.

The total electronic charge transfer to the manganese ions near the interface can be calculated by subtracting the measured valence from the nominal bulk. Figure **??**a shows the computed charge transfer across the interface, which is integrated to find the total charge transfer in Fig. **??**b. We demonstrate a quantitative agreement between the polar catastrophe electronic reconstruction model[**?**] shown in Fig. **??** and the measured charge on the interfacial man-

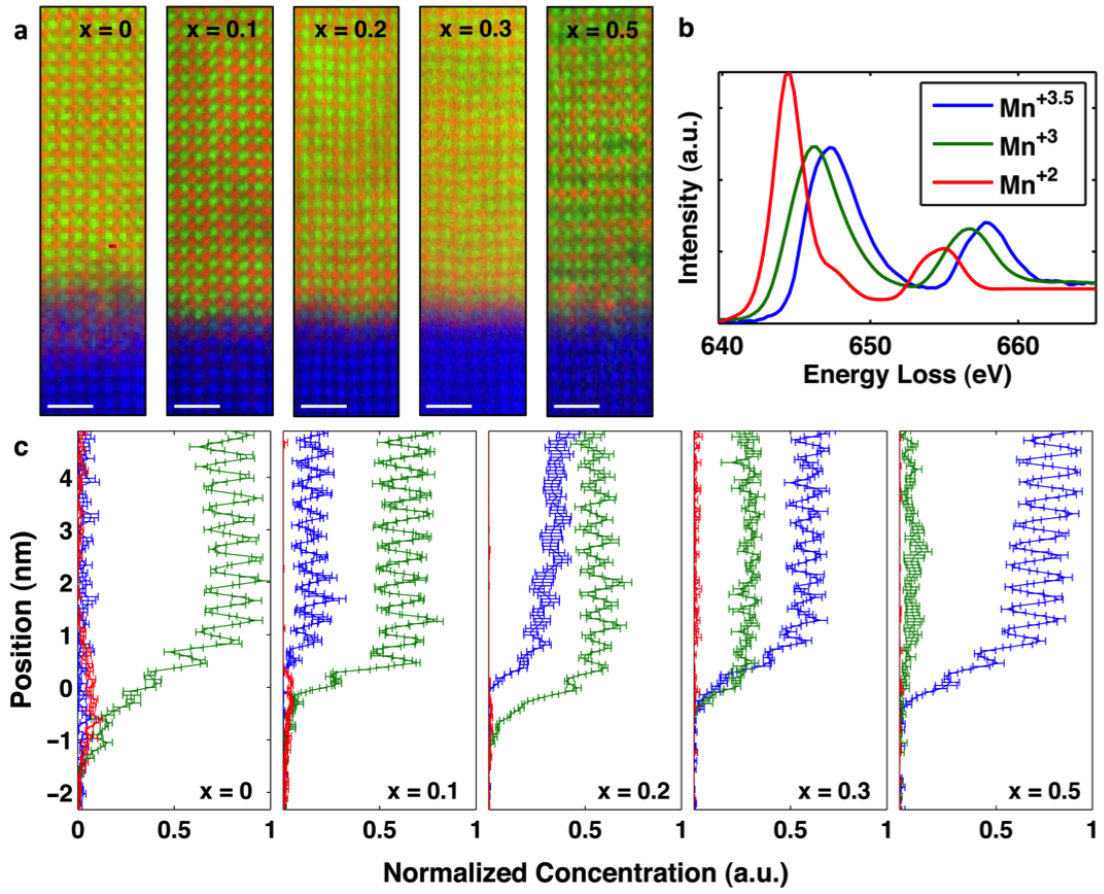

Figure 5.8: Mn valence changes at the series of $La_{1-x}Sr_xMnO_3/SrTiO_3$ interfaces. Spectroscopic images for $x = 0, 0.1, 0.2, 0.3$ and 0.5 films are shown left to right in (a). Ti is plotted in blue, Mn in green and La in red. The $x = 0.5$ image shows cation ordering not observed in the other films. Three Mn reference spectra shown in (b) for Mn^{+2}, Mn^{+3} and $Mn^{+3.5}$ were used to determine the Mn valence across the interface. The results of the non-negative non-linear least squares fit is shown in (c) for x = 0, 0.1, 0.2, 0.3 and 0.5 ordered left to right. Error bars plot the standard error of the mean generated from five binned regions from each spectroscopic image.

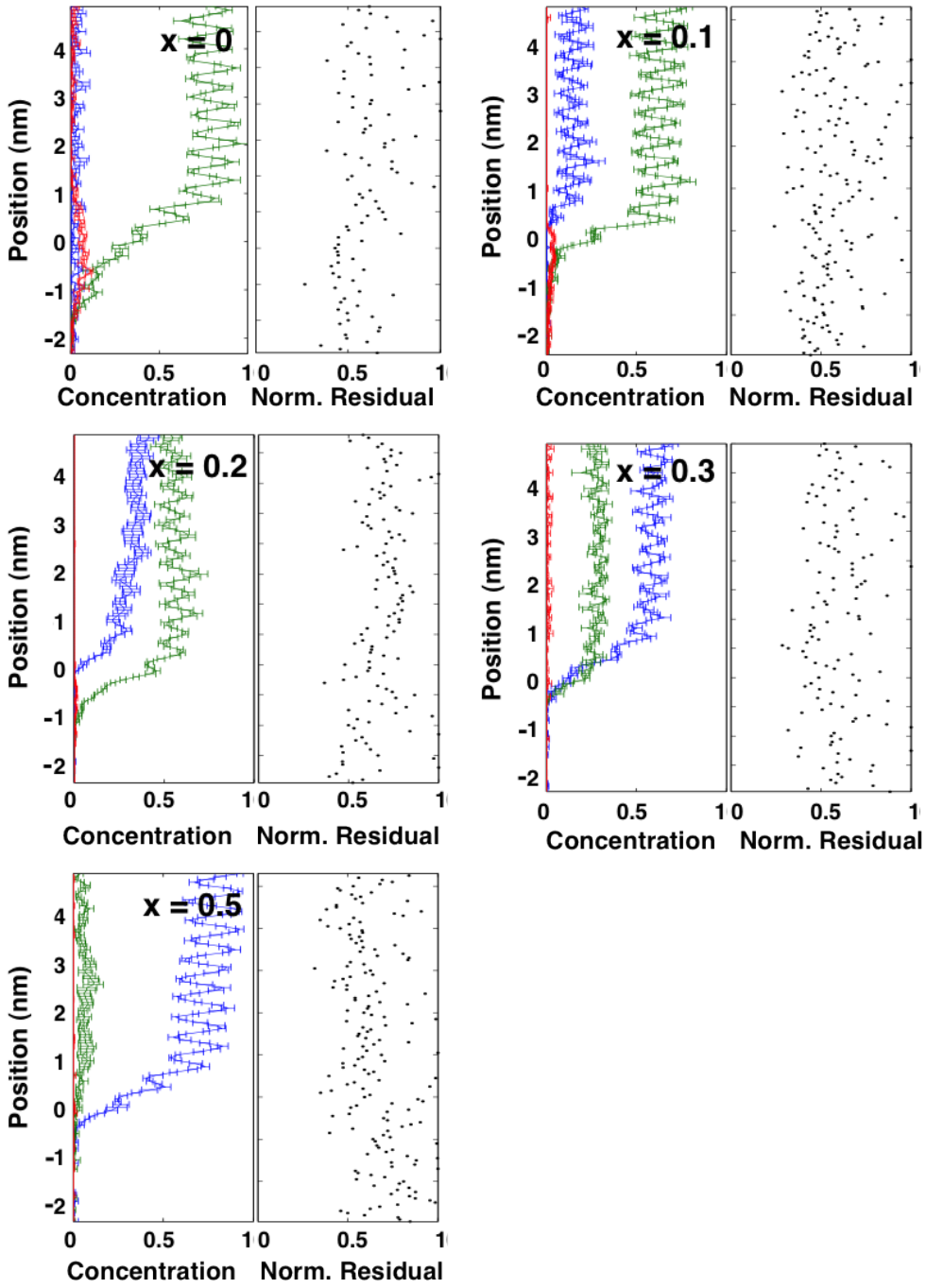

Figure 5.9: Normalized residuals for the samples measured in Fig. **??**. The concentration plots, reproduced from Fig. **??**(c) and the corresponding residual are plotted for $x = 0, 0.1, 0.2, 0.3$ and 0.5. In all cases there is no spatial variation in the residual indicating that the components shown in Fig. **??**(a) capture the fine structure of the Mn-$L_{2,3}$ edge through the interface for all samples.

ganese sites for $x \leq 0.2$. For $x \geq 0.3$, significantly less charge is measured with no statistically significant electronic transfer for x = 0.5 despite the prediction of 0.25 e^-. We note that this sharp discontinuity as a function of doping in the measured charge build-up at the interface coincides with at the room temperature metal-to-insulator transition at $x = 0.3$. In metallic films electronic charge transfer to the interface is expected to equilibrate the chemical potentials and to balance interface charges. The magnitude of the interface charge can be different from the polar catastrophe model because the simple ionic picture is no longer valid to describe the electrostatic potential. It is, therefore, not surprising that the magnitude of the compensating charge required for the metallic films deviates from that expected for insulating films.

Finally, we note that not only does the total electronic charge transfer to the interface change in the proximity of the metal to insulator transition, yet also the length over which this reconstruction occurs. As shown in Fig. **??**c, despite the decrease in charge transferred with increasing x, the width of the electronic reconstruction region remains roughly constant for $x \leq 0.2$ with the width of the charge profiles constant at 4.4 unit cells. Surprisingly, the significant intermixing observed for the $LaMnO_3/SrTiO_3$ interface in contrast to the other films did not impact the width of charge transfer. In contrast, the small amount of charge transferred to the $x = 0.3$ interface has a narrower width with modulations observed only over 2 unit cells. The length scale in the metallic state is consistent with previous theoretical[**?**] and experimental[**?**] measurements of screening lengths for $x = 0.33$ films of approximately 1-2 unit cells. Thus, both the magnitude and the spatial width of the excess electrons at the LSMO/STO interface are tuned across this phase transition.

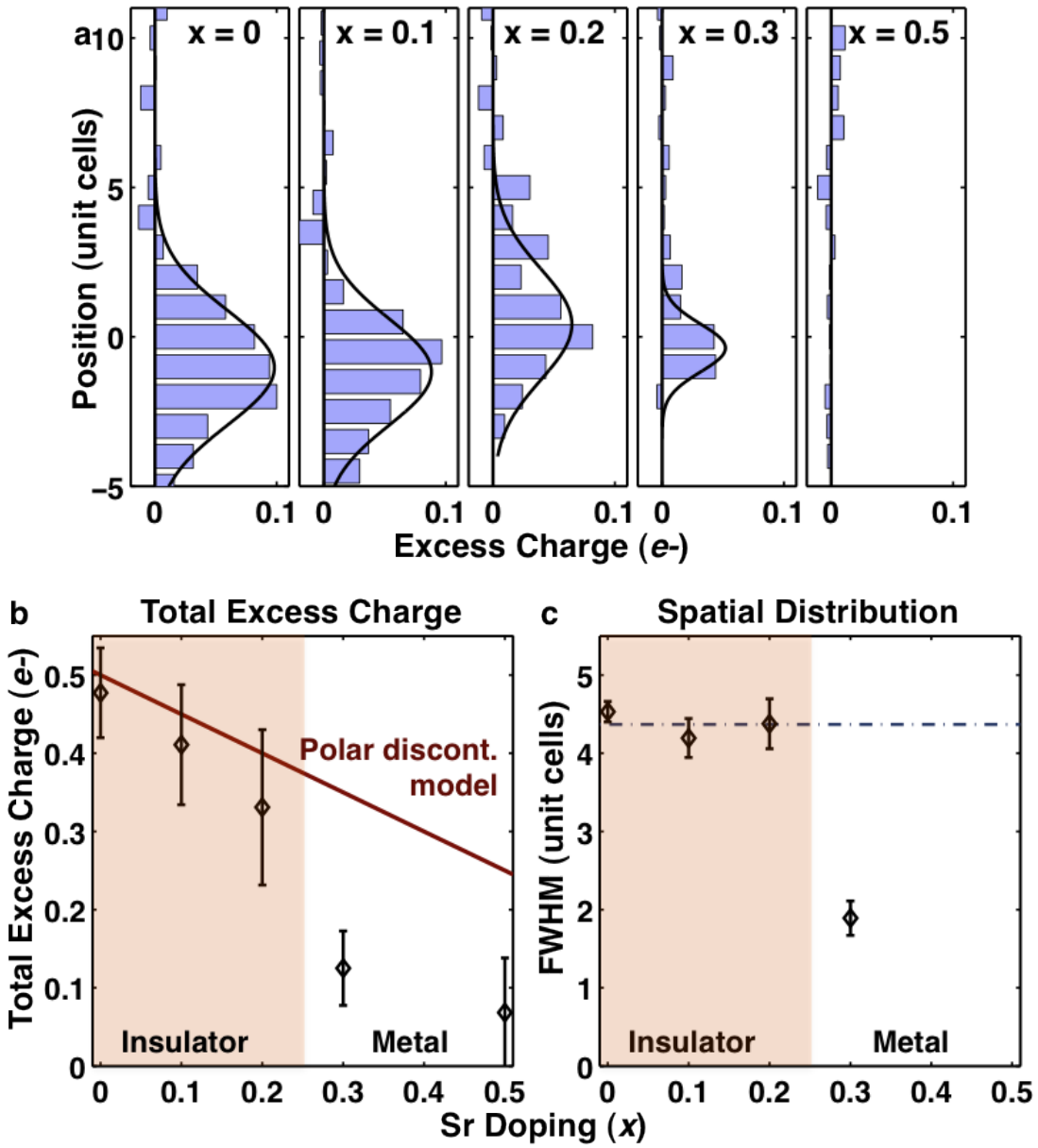

Figure 5.10: The excess charge accumulation at the interface computed from the deviation between the bulk and measured Mn valence across the interface. (a) The total excess charge per unit cell is plotted across the interface $x = 0, 0.1, 0.2, 0.3$ and 0.5 ordered left to right. The 0 of position denotes the interface, defined by the midpoint of the Mn concentration profile. A Gaussian fit was added as a guide to the eye. (b) The total excess charge integrated across the interface and compared to the polar discontinuity model. (c) The full width at half maximum of the Gaussian charge profiles shown in (a). A dashed line is added through the mean of the width for the insulating samples at 4.4 unit cells. Error bars are the standard error of the mean.

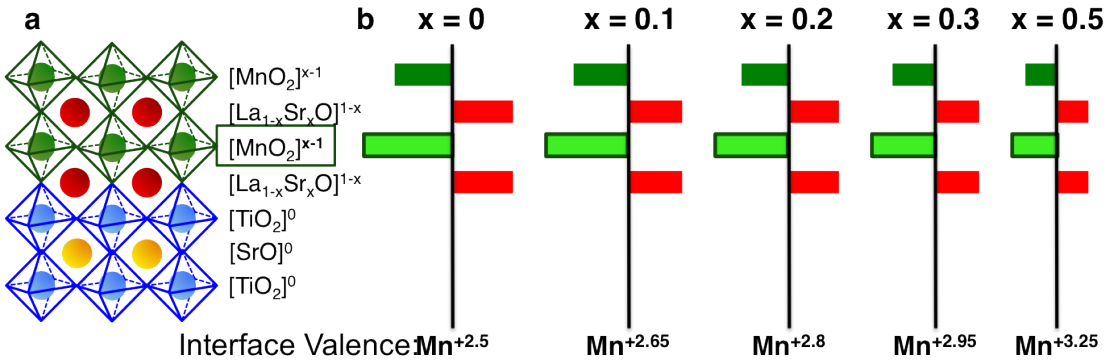

Figure 5.11: The total charge needed on the Mn sites to alleviate the polar catastrophe. (a) shows a cartoon of the polar discontinuity at an atomically abrupt LSMO/STO interface. To alleviate the polar catastrophe charge is transferred to the interfacial Mn sites resulting in a reduction of the Mn valence. The charge on the Mn sites and the Mn valence at the interface for $x = 0$ to $x = 0.5$ are shown in (b).

5.4 Conclusions

In summary, we probed a series of $La_{1-x}Sr_xMnO_3$ thin films on $SrTiO_3$ ranging from the paramagnetic insulating to ferromagnetic metallic regions of the phase diagram. By mapping the valence changes of the manganese sites across the interface, we show a quantitative agreement between the total electron transfer to the interface for the insulating region of the phase diagram and a significantly reduced charge transfer for the metallic films. Moreover, we measured the spatial extent of the resultant excess electrons residing at the interface. Despite differences in chemical intermixing, the electronic reconstruction width remains constant at about four unit cells for the insulating films yet narrows to two unit cells as LSMO becomes metallic. The engineering of the spatial extent of the interface charge should be useful in the construction of novel electronic phases at oxide interfaces.

CHAPTER 6

SPATIAL DELOCALIZATION OF EXCESS CHARGE IN MANGANITE SUPERLATTICES

6.1 Introduction

As shown in Chapter 2, interfaces can strongly modify the properties of complex oxide systems, both through the stabilization of phases not present in the bulk compounds as well as through electronic reconstructions in response to interfacial layering. Chapter 2 described the $LaTiO_3/SrTiO_3$ system where metallic conductivity was observed in superlattices of two insulators. $LaMnO_3$ and $SrMnO_3$ are both non-magnetic insulators yet appropriately selected superlattices demonstrate a metallic ferromagnetic state.[**?**, **?**] For the $(LaMnO_3)_n/(SrMnO_3)_n$ system, superlattices with $n \leq 4$ were found to behave like the bulk solid-solution $La_{1/2}Sr_{1/2}MnO_3$ yet superlattices with $n > 4$ exhibited properties more similar to the bulk constituents.

Further work was done on the $(LaMnO_3)_{2n}/(SrMnO_3)$ system; the bulk solid solution, $La_{2/3}Sr_{1/3}MnO_3$ is a ferromagnetic metal at room-temperature and of interest for spin-polarized tunnel junction memories. There was a sharp change in the electric properties as a function of n: notably, for $n \leq 2$, the samples exhibit metallic behavior at low temperatures, similar to the bulk conditions. For $n \geq 3$, the resistivity increases as a function of temperature.[**?**, **?**, **?**]. The magnetic properties were also found to depend strongly on the layering. A uniform ferromagnetic state was observed for $n \leq 2$ with a strongly modulated ferromagnetic state for $n > 3$ [**?**, **?**]

$LaMnO_3$ is composed of Mn^{+3} where the manganese d electrons occupy a $t_{2g}^3 e_g^1$ state. A Mott-Hubbard gap breaks the degeneracy of the e_g orbitals through a Jahn-Teller distortion.[**?**] $LaMnO_3$ is an A-type antiferromagnet. In contrast, $SrMnO_3$ has a Mn^{+4} oxidation state and a d orbital configuration of t_{2g}^3. $SrMnO_3$ is thus a band insulator (and a G-type antiferromagnet) in the bulk form. Thus, superlattices of $LaMnO_3$ and $SrMnO_3$ include a variation of Mn^{+3} and Mn^{+4}. Theoretical work suggested that the conductivity observed in the $n = 1$ and $n = 2$ layers could be attributed to a double-exchange mechanism with the remaining layers.[**?**]

In this chapter, we will experimentally probe the spatial variation of the manganese e_g electron through variable n $LaMnO_3)_{2n}(SrMnO_3)_n$ superlattices. We will show a delocalization of the charge for $n = 1$ and a spatially varying charge density for $n \geq 2$. The fundamental delocalization of this charge is crucial for correlating the electronic properties to the theoretical models. As shown in Chapter 3, EELS can in principle map local bonding changes with atomic-resolution in two-dimensions, laying the foundation for the mapping of the charge delocalization here.

6.2 Experimental

Superlattices of $LaMnO_3$ and $SrMnO_3$ were grown by reactive molecular-beam epitaxy. Details of the growth conditions can be found elsewhere [**?**]. Samples were prepared for imaging through tripod polishing followed by a low angle ion milling. Energy energy loss spectroscopy was employed to measure the composition and valence of the elements on the Nion UltraSTEM.

6.3 Results and Discussion

6.3.1 Constant n $(LaMnO_3)_{2n}(SrMnO_3)_n$ superlattices

To investigate the spatial delocalization of the e_g electron in the $(LaMnO_3)_{2n}(SrMnO_3)_n$, we first investigate superlattices grown with a constant value of n. This allows the explicit measure of conductivity to compare to previous studies. A representative HAADF-STEM image of a $n = 1$, $n = 2$ and $n = 3$ superlattice is shown in Figs. **??** (a - c) respectively. An EELS image mapping the concentration of the manganese and lanthanum atoms is shown as an insert. Each of the superlattices shows atomically abrupt interfaces without chemical interdiffusion indicating the atomic layer precision achievable by MBE. As was previously reported, resistivity measurements shown that the $n = 1$ and $n = 2$ superlattices are conducting at low temperatures with an uptick in the resistivity observed for the $n = 3$ superlattice. Larger EELS spectroscopic images for the $n = 2$ and $n = 3$ superlattices are shown in Fig. **??** and Fig. **??** respectively. Figure **??** shows a full 1024 x 1024 pixel EELS spectroscopic image, the largest recorded at the time of publication, allowing the mapping of elemental concentrations at scales associated with that of a typical HAADF-STEM image.

6.3.2 Spectroscopic imaging of the $(LaMnO_3)_2(SrMnO_3)_1$ superlattice

We can also probe the manganese valence present in the EELS images shown in Fig. **??**. Figure **??** explores the manganese valence through the $n = 1$ su-

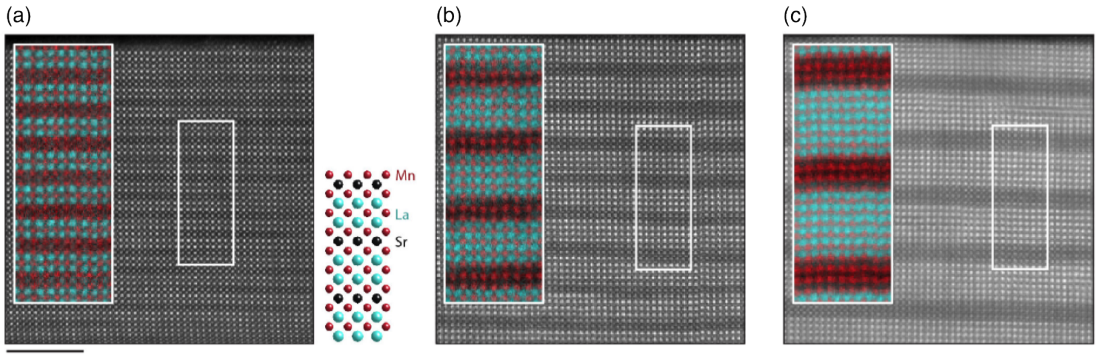

Figure 6.1: HAADF-STEM images of an $n = 1$, $n = 2$ and $n = 3$ $(LaMnO_3)_{2n}(SrMnO_3)_n$ superlattices are shown in a - c respectively. An inset of each image displays an EELS spectroscopic image with lanthanum in red and manganese in turquoise. Each of the samples shows atomically abrupt interfaces with little intermixing.

perlattice. Here a single Mn-$L_{2,3}$ line shape shown in Fig. **??**(a) is sufficient to capture the EELS fine structure through the superlattice shown in Fig. **??**(b). The fine structure of the Mn-$L_{2,3}$ edge binned parallel to the interface direction is shown in Fig. **??**(c). We note that there is contrast coming from the spatial distribution of manganese in the superlattice, yet not a shift in the onset energy of the edge that would be indicative of this. When the single line shape shown in Fig. **??**(a) is fit to the data shown in Fig. **??**(c), there is no structure remaining in the residual of the fit as shown in Fig. **??**(a). This analysis indicates that there is a constant $Mn^{+3.33}$ valence state observed throughout the structure and the e_g electron is delocalized.

This analysis can be independently confirmed through the analysis of the oxygen fine structure. As shown in Chapter 3, the fine structure of the oxygen fine structure can track the number of d holes on the transition metal coordinated to the oxygen atom in addition to the bonding to the neighboring cations. Figure **??**(a) displays the same spectroscopic image pictured in Figure Fig. **??**(a)

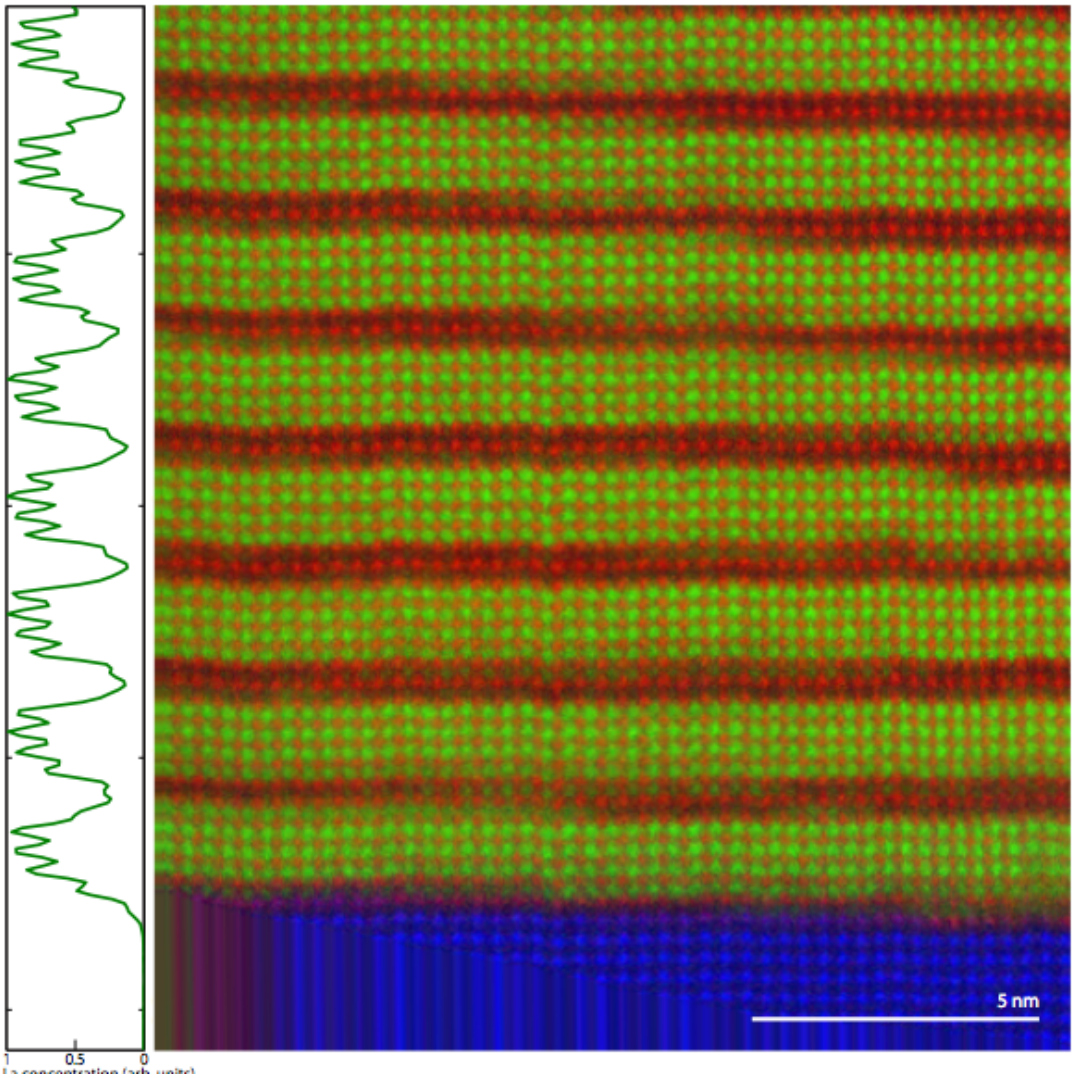

Figure 6.2: EELS spectroscopic image of the $n = 2$ $(LaMnO_3)_{2n}(SrMnO_3)_n$ superlattice. Lanthanum, manganese and titanium are shown in green, red and blue respectively. The streaks at the bottom of the image are a result of the post-acquisition drift-correction algorithm.

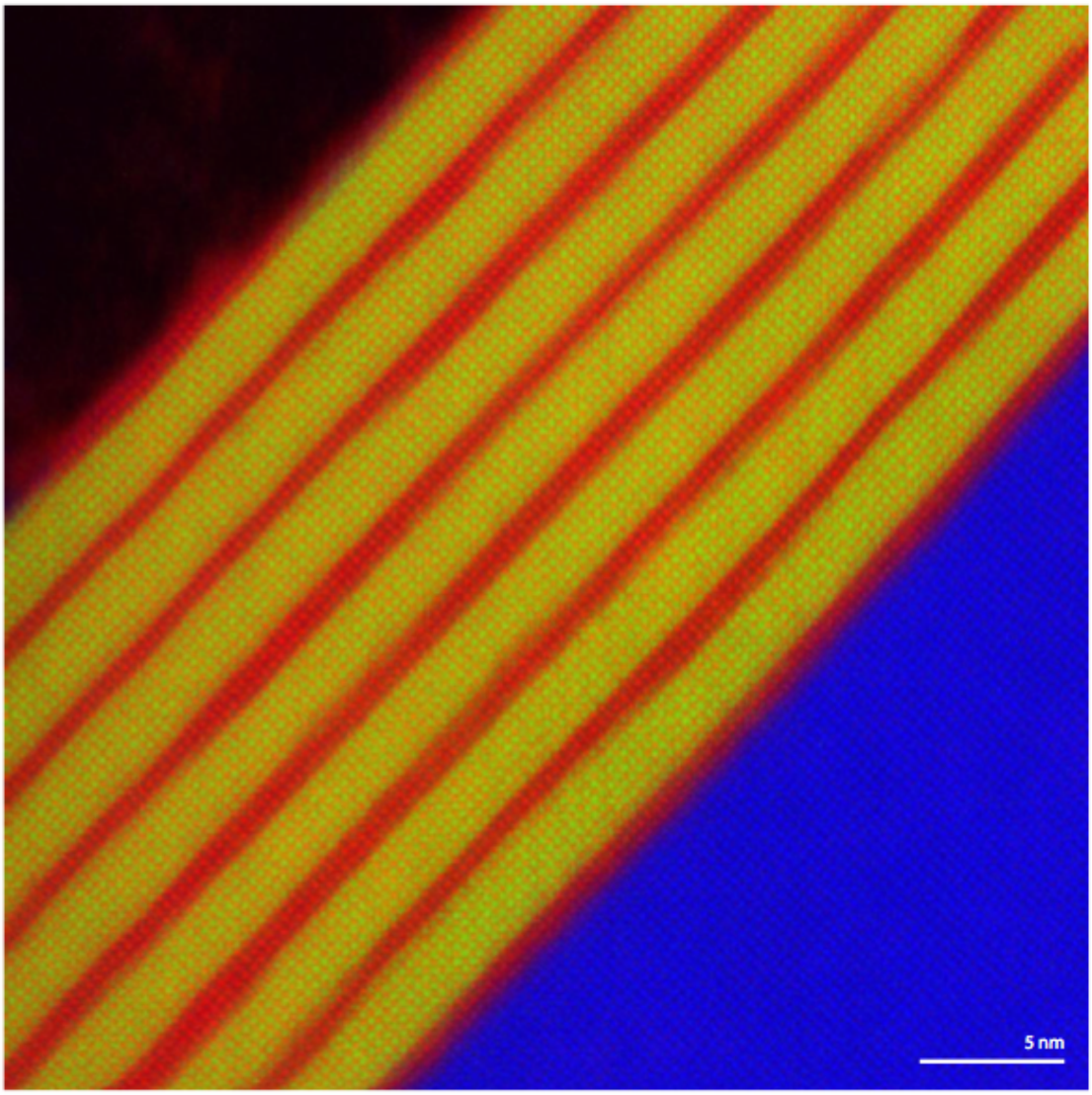

Figure 6.3: EELS spectroscopic image of the $n = 3$ $(LaMnO_3)_{2n}(SrMnO_3)_n$ superlattice. Lanthanum, manganese and titanium are shown in green, red and blue respectively. No post-acquisition drift correction was necessary however the noise was reduced with the use of a weighted-PCA algorithm

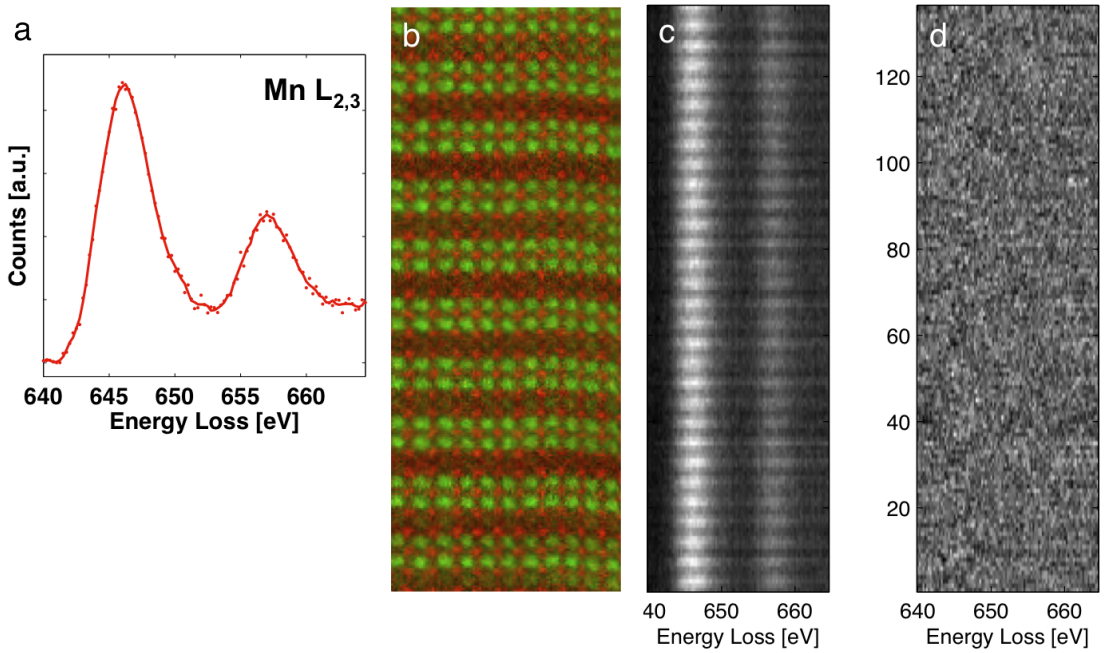

Figure 6.4: Atomic-resolution valence mapping of the $(LaMnO_3)_2(SrMnO_3)_1$. The mean Mn-$L_{2,3}$ edge observed is shown in a, corresponding to the EELS spectroscopic image shown in b. A 2-D plot of the Mn-$L_{2,3}$ edge is shown in (c), binned parallel to the interface. Fitting the single component to the full spectra shown in (c) produces no remaining residual as shown in (d), indicating that the valence does not vary spatially.

with the fine structure of the O-*K* edge, binned parallel to the interface, pictured in Fig. **??**(b). Here, we note a clear shift in the energy of the second peak as the signal is collected from the $SrMnO_3$ and $LaMnO_3$ planes. Indeed, a MCR analysis of the edge can extract two distinct components as shown in Fig. **??**(c). These components are fit to the oxygen signal as shown in Fig. **??**(c). A clear oscillation is seen with a "$LaMnO_3$" signal observed for two monolayers followed by "$SrMnO_3$" for one. It is important to note that only second peak of the O-*K* edge is distinct between the two EELS line shapes. The second peak tracks the empty *d* states on the neighboring lanthanum and strontium and thus oscillates with the composition.[**?**] In contrast, the pre-peak tracks the hybridization between

the oxygen atom and the *d* electrons on the manganese site; notably there is thus no spatial variation in the *d* electron density of states despite the clear ability of the O-*K* edge to track bonding changes at the atomic scale.[**?**]

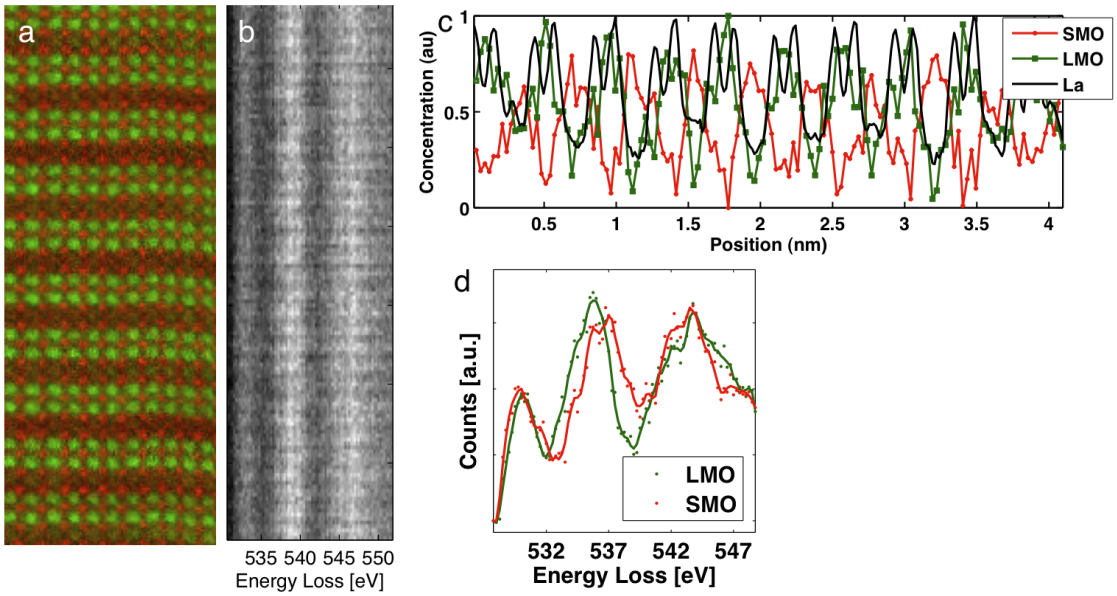

Figure 6.5: Atomic-resolution mapping of the O-*K* edge fine structure of the $(LaMnO_3)_2(SrMnO_3)_1$. a. A spectroscopic image of the superlattices with Mn in red and La in green. b. The fine structure of the O-*K* edge from (a) binned parallel to the interfaces. From this fine structure two distinct components, (d), can be extracted and fit to the data as shown in (c). The La signal is overlaid on the two components in (c) to demonstrate that the "$LaMnO_3$" O–*K* edge fine structure does follow the spatial location of the La.

A similar analysis was attempted on the remaining $n = 2$ and $n = 3$ superlattices. Similar to previous studies,[**?**] a spatial variation in the manganese edge was detected–however, the manganese valence was found to *decrease* when entering the $SrMnO_3$ layers rather than increase! This is in contrast to the expected valence for $SrMn^{+4}O_3$ and $LaMn^{+3}O_3$. Angle-resolved photoemission (ARPES) studies of the superlattices, performed directly after growth without exposing the sample to air, found the expected $SrMn^{+4}O_3$ valence state.[**?**] Thus efforts

were made to avoid exposure to air when attempting to image a variable n superlattice below. The samples was capped with a thick aluminum capping layer prior to removing the sample from the vacuum of the MBE chamber. The sample was then immediately prepared using the focused ion beam where exposure to air and aqueous solvents could be avoided; the sample was imaged in the microscope immediately following its removal from the FIB. It is important that x-ray studies of the bulk wafers–uncapped yet stored in the N_2 environment of a desiccator for approximately one month (relative humidity below 5%)–also showed the low valence state of manganese. Thus, we do not believe that this is a simple artifact of the TEM preparation or imaging technique.

6.3.3 Variable n $(LaMnO_3)_{2n}(SrMnO_3)_n$ superlattices: HAADF-STEM imaging

While the variable n superlattices allow the explicit measurement of the transport properties, a single superlattice with varying n allows a simultaneous measurement of the manganese valence across a single sample. Figure **??** shows a HAADF-STEM of such a superlattice containing six repeats of $(LaMnO_3)_2(SrMnO_3)_1$ followed by three repeats of the $n = 2$, $n = 3$ and $n = 4$ repeats. The HAADF-STEM image indicates that the film is coherent and epitaxial to the substrate with the intended composition.

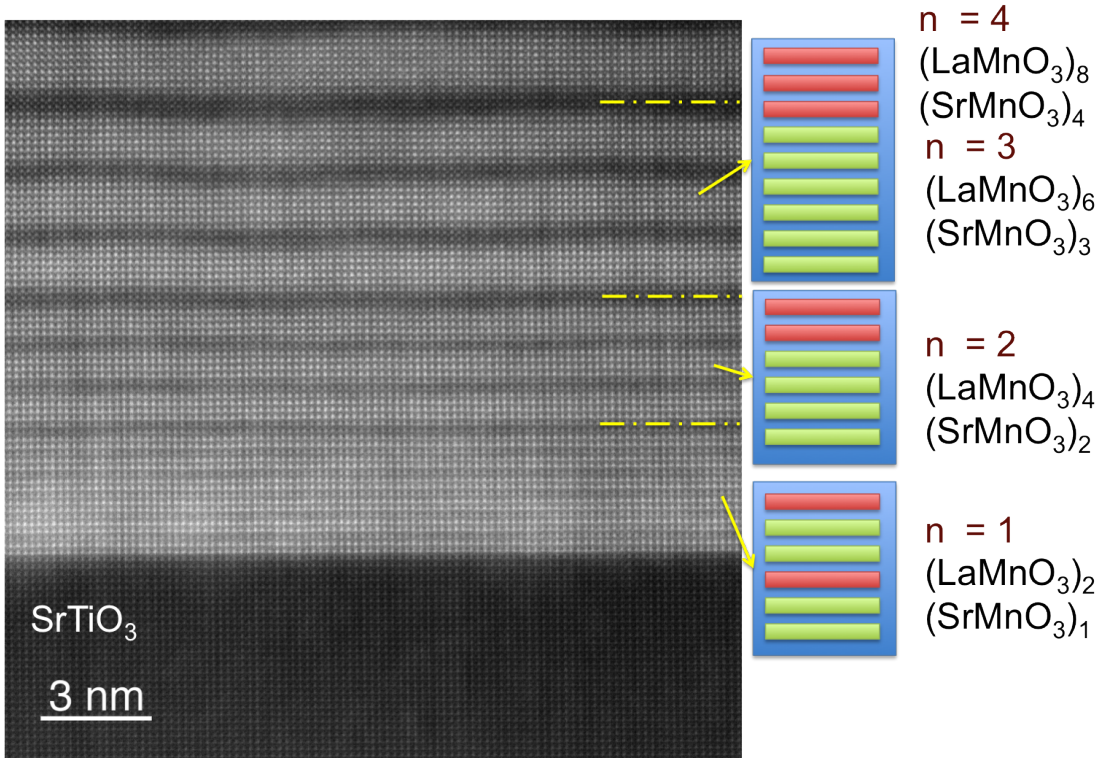

Figure 6.6: HAADF-STEM image of a variable n $(LaMnO_3)_{2n}(SrMnO_3)_n$ superlattice on a $SrTiO_3$ substrate. There are six repeats of $(LaMnO_3)_2(SrMnO_3)_1$ followed by three repeats of the $n = 2$, $n = 3$ and $n = 4$ repeats. A cartoon of the layering pattern is shown on the side.

6.3.4 Spectroscopic imaging of the electronic charge delocalization in $(LaMnO_3)_{2n}(SrMnO_3)_n$ superlattices

Figure **??** evaluates the manganese valence across $n = 1$, $n = 2$ and $n = 3$ layers of the $(LaMnO_3)_{2n}(SrMnO_3)_n$ superlattice. The concentration map shown in **??**(a) indicates the clear patterning of three repeats of the $n = 1$ structure, $(LaMnO_3)_2$, followed by three of the $n = 2$ structure, $(LaMnO_3)_4$ and finally two of the $n = 3$ structure, $(LaMnO_3)_6$. The Mn-$L_{2,3}$ edge was binned parallel to the interfaces and is shown in Fig. **??**(b). Unlike the spectra shown in Fig. **??**(c), there is a

change in the line shape which emerges following the $n = 1$ layering. This was explored further by using MCR to pull out two distinct components, $Mn^{+3.5}$ and Mn^{+3} as shown in Fig. **??**(d). These were fit to the data to provide the spatially varying concentration in **??**(c).

We note that there is a modulation in the manganese valence with the position for the $n = 2$ layers. The La concentration is overlaid on the Mn^{+3} signal in Fig. **??**(c) indicating a lower electronic charge density there. These changes become more pronounced for the $n = 3$ layers with a large change in the concentration across the interfaces. We note, however, despite the correct pinning of the excess charge density to the $SrMnO_3$ layers, in contrast to previous studies,[**?**] the absolute charge remains below that expected for a fully oxidized $LaMnO_3)_{2n}(SrMnO_3)_n$ superlattice. Using the fit of the two components to the $n = 1$ layers, and the assumption that we should observe a constant $Mn^{+3.33}$ valence there from the previous work, we can label the "$SrMnO_3$" valence as $Mn^{+3.5}$. While above the Mn^{+3} observed in $LaMnO_3$, it remains below the nominal Mn^{+4} predicted. Analysis of the EELS line shape in Fig. **??**d further corroborates the assignment of this valence below Mn^{+4} given the expected energy difference in the peak onset.

Once again, we can partner the evaluation of the Mn-$L_{2,3}$ edge with that of the O-K edge as shown in Fig. **??**. Here the EELS spectroscopic image is shown again for reference in Fig. **??**(a). The evaluation of the O-K edge produced three distinct components as shown in Fig. **??**c and as fit to the signal in Fig. **??**(b). We note that for both the $n = 1$ and the higher n layers, there is a clear oscillation of the signal which tracks the cation bonding of the oxygen atom. The fine structure of the "$LaMnO_3$" component has a lower pre-peak signal than that of

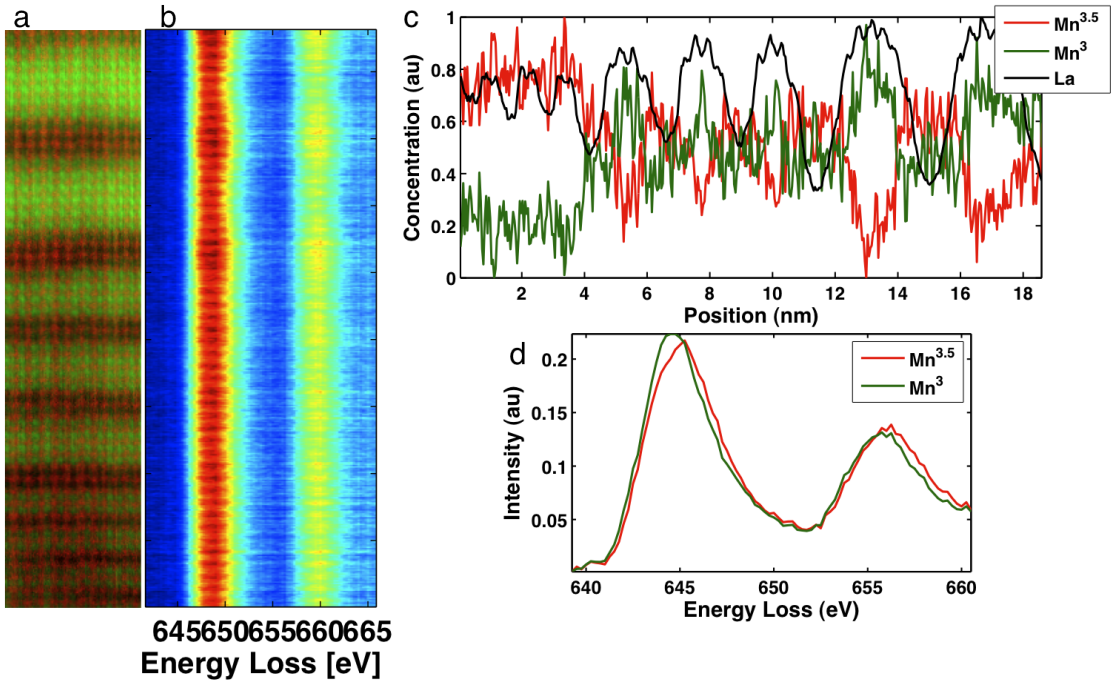

Figure 6.7: Mapping the Mn valence in the $n = 1$, $n = 2$ and $n = 3$ $(LaMnO_3)_{2n}(SrMnO_3)_n$ superlattice. A spectroscopic image is pictured in (a) with La in green and Mn in red. There are three repeats of the $n = 1$ and $n = 2$ layers and two of the $n = 3$ layers. The Mn-$L_{2,3}$ edge binned parallel to the interface is shown in (b). The change in structure through the superlattice was fit with two Mn components as shown in (d) and fit to the data in (c). The La signal is overlaid in (c) to show that there is a constant valence observed in the $n = 1$ layers yet a oscillating charge for the higher n values.

the "$SrMnO_3$" consistent with the expected bulk signals where there is a full e_g electron on the "$SrMnO_3$" sites and the absence of e_g electronic charge on the "$LaMnO_3$" sites. The intensity of these pre-peak for the "$SrMnO_3$" signal however is still shy of that for the bulk component[**?**] consistent with the manganese valence assignment to $Mn^{+3.5}$ in these layers. Finally, we note that three components are needed to fully match the O-K edge through the compound. This third "LSMO" component captures that the cation stoichiometry varies through the $n = 1$ layers–and thus the second peak of the O-K edge moves–however the Mn

electronic density–manifest as the intensity of the pre-peak–does not change.

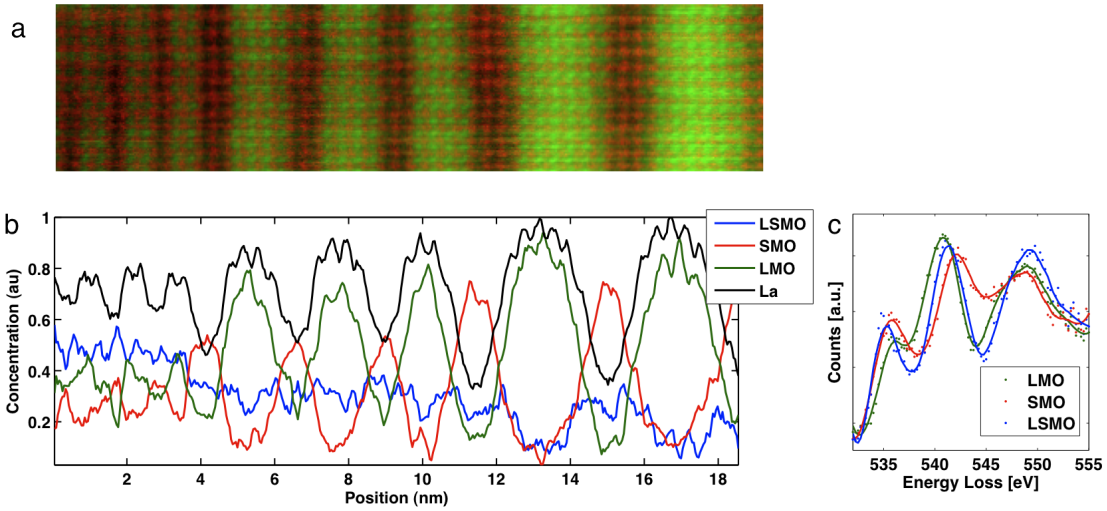

Figure 6.8: Mapping the O-K edge fine structure in the $n = 1$, $n = 2$ and $n = 3$ $(LaMnO_3)_{2n}(SrMnO_3)_n$ superlattice. A spectroscopic image is pictured in (a) with La in green and Mn in red. Three distinct components were extracted in (c) and fit to the data in (b).

We can also map the manganese valence in 2-D through the $n = 4$ layers. Figure **??**(a) shows an EELS spectroscopic image of the $n = 2$, $n = 3$ and $n = 4$ layers. The simultaneous ADF signal is shown in Fig. **??**(b). There a signal mean Mn-$L_{2,3}$ spectra was extracted from each of the manganese lattice sites in the crystal, similar to the analysis for the iron valence in Chapter 3. The color overlay shows the measured valence of that location using the EELS spectra from **??**(d). A full 2-D map of the fit of the two components to the Mn signal is shown in **??**(c). In the lower layers, we can see a clear variation with the reduced valence manganese clustering to the $LaMnO_3$ layers and the increased charge sitting on the $SrMnO_3$ layers. This persists to the $n = 4$ layers, however some spatial variation in the measured valence starts to emerge.

From these spectroscopic images, we can compute the mean manganese va-

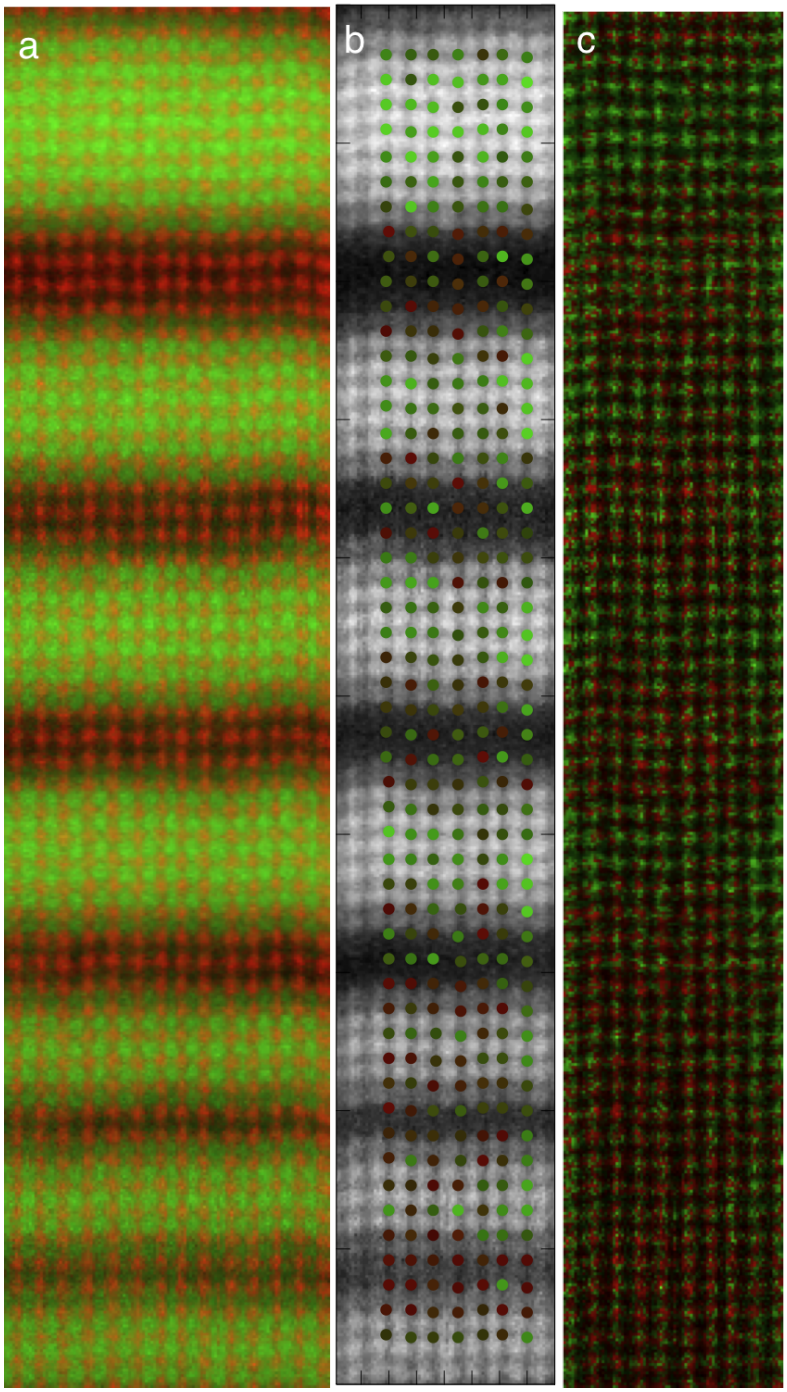

Figure 6.9: Mapping the Mn valence in the $n = 2$, $n = 3$ and $n = 4$ $(LaMnO_3)_{2n}(SrMnO_3)_n$ superlattice. A spectroscopic image is pictured in (a) with La in green and Mn in red. The simulatenously recorded ADF image is shown in (b). A signal Mn spectra was extracted from each lattice site–the valence is overlaid on the site using the components given in Fig. **??**c. A full fit of the components in Fig. **??**(c) is shown in (c).

lence observed through the superlattice. Multiple spectroscopic images were cross-correlated and the signals averaged. Figure **??** shows the measured valence, unit cell by unit cell, through the structure with the La concentration overlaid. It is important to note that hints of a spatially varying valence are observed in the $n = 1$ layers however the valence is near uniform in this location. As the $n = 2$ layers begin, a strong oscillation in the valence is observed showing the localization of the electronic charge in these layers.

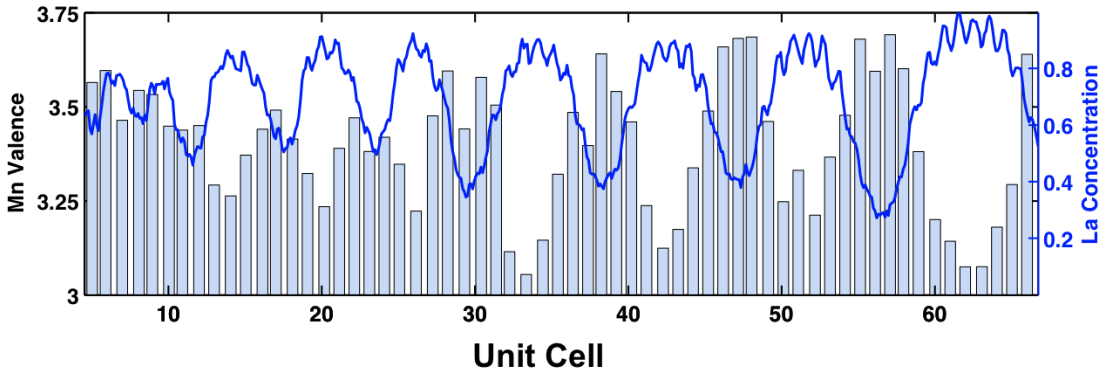

Figure 6.10: Mean Mn valence through the $LaMnO_3)_{2n}(SrMnO_3)_n$ superlattice. The layered valence was computed by cross-correlating multiple spectroscopic images and fitting the two Mn-$L_{2,3}$ reference spectra to the data. The La signal is overlaid for reference in blue; the quantification of the La concentration is shown on the right axis.

Finally, we note that $SrMnO_3$ remain unstable and the bulk valence is not achieved. From Fig. **??**, the mean valence of both the $SrMnO_3$ and the $LaMnO_3$ layers were computed and are plotted in **??**. We note that the there is a steady decrease in the total electronic charge from the $n = 1$ layers to the higher n layers. This tracks the instability of the $SrMnO_3$ layers and partial conversion of these layers to a lower valence manganese states.

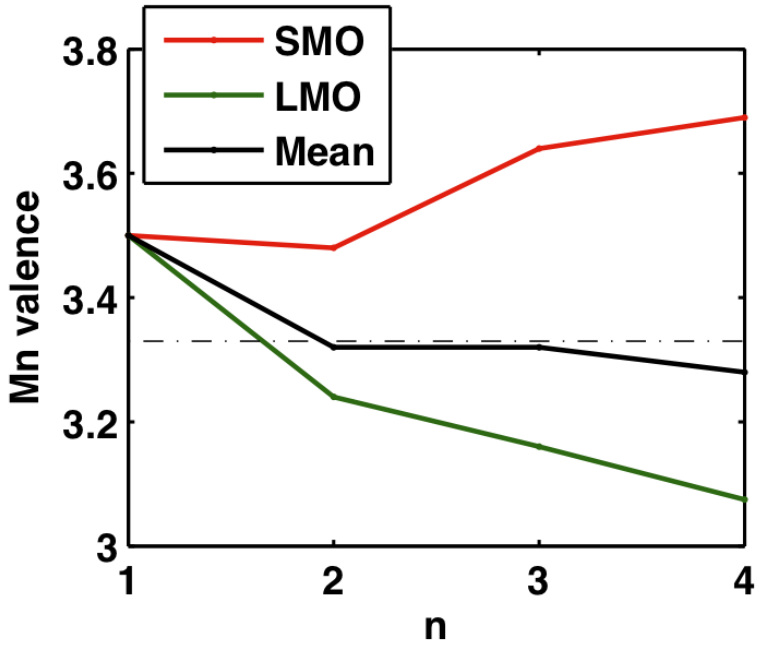

Figure 6.11: The total mean valence in the $LaMnO_3$ and $SrMnO_3$ layers from Fig. **??**. A mean valence through the structure is also plotted, showing the lower valence in the higher n layers.

6.4 Conclusions and speculation

Here we investigated a series of $(LaMnO_3)_{2n}(SrMnO_3)_n$ superlattices with n varying from $n = 1$ to $n = 4$. We showed that for the $n = 1$ superlattice the charge is delocalized through the superstructure with a mean $Mn^{+3.33}$ state observed throughout. The mapping of the cation stoichiometry through the hybridization of the A-site cation/oxygen atom demonstrated the atomic level sensitivity despite the fundamentally delocalized charge. For the $n = 2$ superlattices, we observed the charge start to localize on the layers with a build-up of charge on the $SrMnO_3$ layers.

Despite the correct trends observed, the total charge observed does not

match the Mn^{+4} state expected for $SrMnO_3$. It is possible that strain played a role in driving the state towards this valence. $SrMnO_3$ is metastable in the perovskite cubic form and has a bulk lattice constant of 3.81 Å; reducing the sample to form $SrMnO_{3-\delta}$ increases the lattice constant.[**?**] Given that the bulk lattice constants of $LaMnO_3$ and $SrTiO_3$ are 3.94 Å and 3.91 Å respectively, $SrMnO_3$ experiences a considerable tensile strain. This strain can partially relieved by relaxing the structure to the $SrMnO_{2.5}$ form with a lattice constant of 3.84 Å. Future work could explore this by growing $SrMnO_3$ on a series of samples with both compressive and tensile strain and comparing the resulting manganese valence. This is important to understand as theoretical work has suggested that strained $SrMnO_3$ could be multiferroic[**?**]; if the system shows a higher propensity to form oxygen vacancies as it strained, it could make effective application of strain to $SrMnO_3$, rather than $SrMnO_{2.5}$, challenging.

CHAPTER 7

CONCLUSIONS

The interface between transition metal oxides is a playground for stabilizing phases not present in the bulk constituent compounds. Here, we used scanning transmission electron microscopy (STEM) in conjunction with electron energy loss spectroscopy (EELS) to investigate a series of oxide interfaces. By measuring the concentration and valence of the cations across an interface, we have a unique atomic-resolution probe of the local electronic properties. The focus of this thesis was complementing a study of these electronic charges at oxide interfaces with a simultaneous measurement of interdiffusion, vacancies and other defects. This permitted us to determine circumstances in which defects dominated the observed electronic properties in contrast to intrinsic changes.

Chapter 2 presented the polar catastrophe model for understanding the interface between an insulating polar film and non-polar substrate. The presence of alternating positively and negatively charged layers on a non-polar surface causes the build-up of a non-zero electric field and an electric potential which diverges with sample thickness. The polar catastrophe can be alleviated by transferring charge to the interface, manifest as either the presence of an extra half of an electron or hole. In addition, we show that cation off-stoichiometry can also provide charged defects which screen the polarization catastrophe in the absence of valence changes. We also explicitly consider the case of asymmetric interdiffusion and show that while this can add (or subtract) an additional electronic dipole to the interface, it cannot relieve the polarization catastrophe in the absence of valence changes.

Atomic-resolution mapping of bonding changes in the O-*K* edge in hexagonal $LuFe_2O_4$ was presented in Chapter 3. There are two inequivalent oxygen lattice position in $LuFe_2O_4$ with differing bonding to the surrounding iron and lutecium atoms. Due to the resultant different hybridization between the oxygen *p* oribtals to the cation *d* orbitals, the O-*K* edge tracks the local chemical environment with atomic-resolution. Using this atomic-resolution probe we also investigated the iron valence. $LuFe_2O_4$ is purported to be the highest-temperature known ferroelectric ferrimagnet with a charge-ordering on the iron sites giving rise to the improper ferroelectricity. We failed to identify a clear charge-ordering pattern, with only a mean iron valence of $Fe^{+2.5}$ observed, consistent with other recent studies which have questioned the ferroelectricity.

Using this atomic-resolution EELS probe, two polar interfaces were studied in detail. We first examined the $LaAlO_3/SrTiO_3$ interface in Chapter 4. The $LaAlO_3$ film stoichiometry was shown to greatly impact the interface conductivity, with only *Al*-rich samples resulting in conducting interfaces. Using EELS, we demonstrated that the *La*-rich insulating samples accumulated a vacancies on the *B*-site Al/Ti sublattice near the interface. The conducting *Al*-rich samples did not have a local variation in the cation stoichiometry. This provides the first direct evidence of the screening of the polarization catastrophe with cation vacancies.

We then investigated the polar $La_{1-x}Sr_xMnO_3/SrTiO_3$ interfaces in Chapter 5. As a function of *x*, the films range from paramagnetic insulators to ferromagnetic metals. By mapping the valence changes of the manganese sites across the interface, we show a quantitative agreement between the total electron transfer to the interface for the insulating region of the phase diagram and a signifi-

cantly reduced charge transfer for the metallic films. Moreover, we measured the spatial extent of the resultant excess electrons residing at the interface. Despite differences in chemical intermixing, the electronic reconstruction width remains constant at about four unit cells for the insulating films yet narrows to two unit cells as LSMO becomes metallic. This provides a contrast to the system studied in Chapter 4 where extrinsic defects dominated the properties of some of the samples.

Finally, we investigated digital superlattices of $LaMnO_3$ and $SrMnO_3$ in Chapter 6. $LaMnO_3$ has a single electron in the outer $e_g - d$ orbital while $SrMnO_3$ has a e_g^0 state. For $(LaMnO_3)_2(SrMnO_3)_1$, this e_g electron is delocalized throughout the superlattice. In contrast, for $n \geq 2$ $(LaMnO_3)_{2n}(SrMnO_3)_n$ superlattices, the electron mostly resides on the $LaMnO_3$ sites. We observe that the $SrMnO_3$ samples appear to be oxygen-deficient, possibly to relieve the strain imposed by $LaMnO_3$ and the $SrTiO_3$ substrates.

These four systems demonstrated the ability of EELS to probe bonding changes at complex oxide interfaces with atomic-resolution. For the $La_{1-x}Sr_xMnO_3/SrTiO_3$ interfaces, charge-transfer to the interface to the interface to alleviate the polar catastrophe was observed. In contrast, the $LaAlO_3/SrTiO_3$ interfaces demonstrated that defects such as cation vacancies can sometimes dominate the interfacial properties. STEM and EELS should prove powerful tools to the continued investigation of both the intrinsic electronic reconstructions at oxide interfaces as well extrinsic defects which can co-exist.